

AD_____

Award Number: W81XWH-09-1-0280

TITLE: Ovarian tumor-stroma interactions in an in vivo orthotopic model

PRINCIPAL INVESTIGATOR: Per Borgstrom

CONTRACTING ORGANIZATION: Vaccine Research Institute of San Diego
San Diego CA 92109

REPORT DATE: August 2012

TYPE OF REPORT: Annual Report

PREPARED FOR: U.S. Army Medical Research and Materiel Command
Fort Detrick, Maryland 21702-5012

DISTRIBUTION STATEMENT: Approved for Public Release;
Distribution Unlimited

The views, opinions and/or findings contained in this report are those of the author(s) and should not be construed as an official Department of the Army position, policy or decision unless so designated by other documentation.

REPORT DOCUMENTATION PAGE				Form Approved OMB No. 0704-0188	
Public reporting burden for this collection of information is estimated to average 1 hour per response, including the time for reviewing instructions, searching existing data sources, gathering and maintaining the data needed, and completing and reviewing this collection of information. Send comments regarding this burden estimate or any other aspect of this collection of information, including suggestions for reducing this burden to Department of Defense, Washington Headquarters Services, Directorate for Information Operations and Reports (0704-0188), 1215 Jefferson Davis Highway, Suite 1204, Arlington, VA 22202-4302. Respondents should be aware that notwithstanding any other provision of law, no person shall be subject to any penalty for failing to comply with a collection of information if it does not display a currently valid OMB control number. PLEASE DO NOT RETURN YOUR FORM TO THE ABOVE ADDRESS.					
1. REPORT DATE Oct 2012		2. REPORT TYPE Annual Progress Report		3. DATES COVERED Oct 2011 - Jan 2012	
4. TITLE AND SUBTITLE Ovarian tumor-stroma interactions in an in vivo orthotopic model				5a. CONTRACT NUMBER	
				5b. GRANT NUMBER W81XWH-09-1-0280	
				5c. PROGRAM ELEMENT NUMBER	
6. AUTHOR(S) Per Borgstrom, John Welsh E-Mail: rdqti@utqo Biochem				5d. PROJECT NUMBER	
				5e. TASK NUMBER	
				5f. WORK UNIT NUMBER	
7. PERFORMING ORGANIZATION NAME(S) AND ADDRESS(ES) Vaccine Research Institute of San Diego San Diego CA 92109				8. PERFORMING ORGANIZATION REPORT NUMBER	
9. SPONSORING / MONITORING AGENCY NAME(S) AND ADDRESS(ES) U.S. Army Medical Research and Materiel Command Fort Detrick, Maryland 21702-5012				10. SPONSOR/MONITOR'S ACRONYM(S)	
				11. SPONSOR/MONITOR'S REPORT NUMBER(S)	
12. DISTRIBUTION / AVAILABILITY STATEMENT Approved for Public Release; Distribution Unlimited					
13. SUPPLEMENTARY NOTES					
14. ABSTRACT The objective of this project is to develop a syngeneic orthotopic intravital video microscopy method to study ovarian cancer. In this model, MOVCAR cells are implanted on minced, revascularized ovary tissue in a dorsal skinfold chamber and allowed to grow. The most informative strategy has been to serially implant such tumors from mouse to mouse, and follow gene expression. In other experiments, this strategy yields a time course of adaptive responses to the novel environment. With the MOVCAR-pseudo-ovary model, we encountered problems of chamber clouding due to bleeding due to ovulation, which we overcame by titrating progesterin in the host's diet, and toxicity of mCherry, which we overcame by switching to GFP. We are now wrestling with the problem that the MOVCAR cells lose their ability to grow in vitro, for which there are two possible solutions, one relying on the stochasticity of loss of growth in vitro, and the other involving co-evolution of growth in vivo and growth in vitro. We have made substantial progress in developing an algorithmic approach to these adaptive data.					
15. SUBJECT TERMS ovarian cancer, intravital microscopy, orthotopic model					
16. SECURITY CLASSIFICATION OF:			17. LIMITATION OF ABSTRACT	18. NUMBER OF PAGES	19a. NAME OF RESPONSIBLE PERSON
a. REPORT	b. ABSTRACT	c. THIS PAGE			USAMRMC
U	U	U	UU	75	19b. TELEPHONE NUMBER (include area code)

Table of contents

Introduction	2
Body	2
Key research accomplishments	6
Reportable Outcomes	7
Conclusions	7
References	7
Appendices	8

INTRODUCTION

As we stated in our previous progress report, the over-arching goal of this project was to gain a better understanding of gene expression in ovarian cancer, in both the tumor and the stromal part of a tumor. During this process, it is generally understood that both genetics and epigenetics are involved, and that developing tumors also influence the behavior, vis-à-vis gene expression, in the surrounding stroma. To achieve this, we set out to develop a pseudo-orthotopic syngeneic intravital microscopy model for ovarian cancer, and, not surprisingly, encountered difficulties. During the first two years of funding, we solved problems created by the estrous cycle, namely, clouding of the IVM chambers due to bleeding, and toxicity when MOVCAR cells were transformed to express H2b-Cherry. These obstacle delayed the time course of our experiments, but we felt that we were still well-positioned to achieve most of the original approved goals of the project, because we introduced an efficient approach to study gene expression. We have largely succeeded in developing the IVM-ovarian cancer model, although we have not collected as much data on gene expression during adaptation as we had intended. One serious problem over the last period was that cells adapted to grow on ovary tissue in dorsal skinfold chamber for one cycle would not grow in vitro, such that the cells could not be passaged in the manner we proposed. Consequently, the savings we achieved in other experiments could not be applied to the MOVCAR adaptation case. Fortunately, within the past two months, we have succeeded in explanting MOVCAR tumors from the chambers and growing them in vitro. This will allow us to continue along the lines originally proposed.

An implicit goal in these experiments was to develop an effective means of analyzing gene expression data as MOVCAR cells adapted to grow more aggressively on ovary tissue. Due to the obstacles mentioned above regarding estrous, H2b-Cherry toxicity, and the loss of an in vitro growth phenotype in the adaptation experiments that we began early this year, we have only very limited gene expression, and this presented a problem relative to development of the informatics aspects of the proposal. Therefore, we used data we gathered from a similar set of experiments using N202 cells to develop an informatics approach, which we believe sheds quite a bit of light on cancer, particularly metastasis to the brain, which is common in ovarian cancer.

BODY This is our third progress report, and we shall first reiterate some of the text in abbreviated form from our previous reports. In our first report, we changed the SOW to accommodate the fact that H2b-Cherry is toxic to MOVCAR cells. We devised an alternative strategy in which we successfully transformed MOVCAR cells with H2b-GFP, and were able to grow these H2b-GFP cells on pseudo-organ tissues from (B6.129(Cg)-Gt(ROSA)26Sortm4(ACTB-tdTomato,-EGFP)Luo/J)^{nude} mice, which fluoresce in the TRITC part of the spectrum (i.e. red). So, by adapting our cell line and mouse model, we were able to grow the necessary tumors, as of the last progress report. The modified SOW is on record.

Figure 1 is an image of H2b-GFP MOVCAR tumors one week old. Shortly after these pictures were taken, the ovarian tissue in the chamber began to hemorrhage as it continued to ovulate. When this happens, the tissue becomes obscured by blood in the chamber. On a sporadic basis, chambers would last for more than two weeks after implantation of the tumor spheroids, only to succumb to hemorrhaging. After some time, we observed pre-ovulation phenomena, i.e. changes in morphology, that pointed ovulation; fortunately, because we were hitherto mystified by the phenomenon. The solution was to suppress ovulation using progestin. Initially, progestin prevented ovulation, but also suppressed tumor growth, and it took us time to learn that tumor growth is dependent on the dose of progestin, and that a lower dose does not prevent tumor growth. In **Figure 2**, we show a growth curve, which shows the usual drop off due to cell death, and then a post-adaptation increase in tumor mass.

We developed a promising, inexpensive, and robust method to explore differential gene expression in experiments of this sort. The adaptation of cultured tumor cells to grow on pseudo-organ tissue requires a period

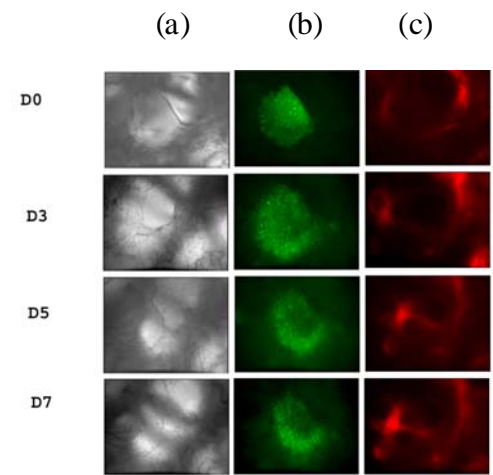


Figure 1. (a) Bright field, vasculature, (b) GFP-Movcar, (c) Tomato pseudo-ovary. Day 0-7 are indicated.

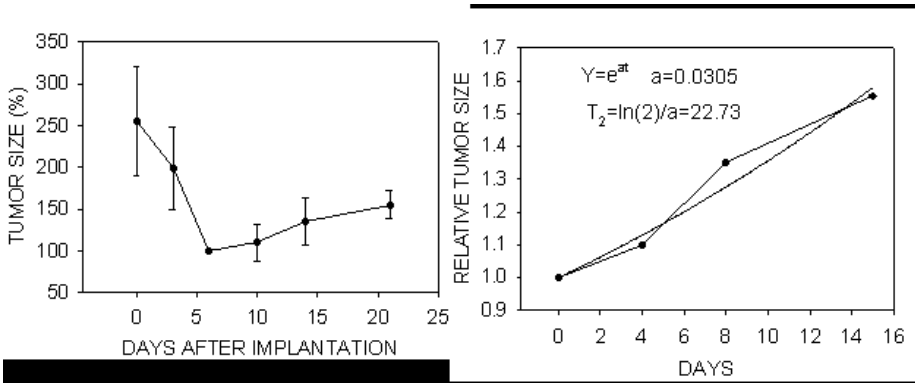


Figure 2. (a) Growth curve for MOVCAR tumor, normalized to Day 6. The initial decline, followed by recovery can be seen. (b) Calculation of growth rate from day 6 and beyond for first training cycle.

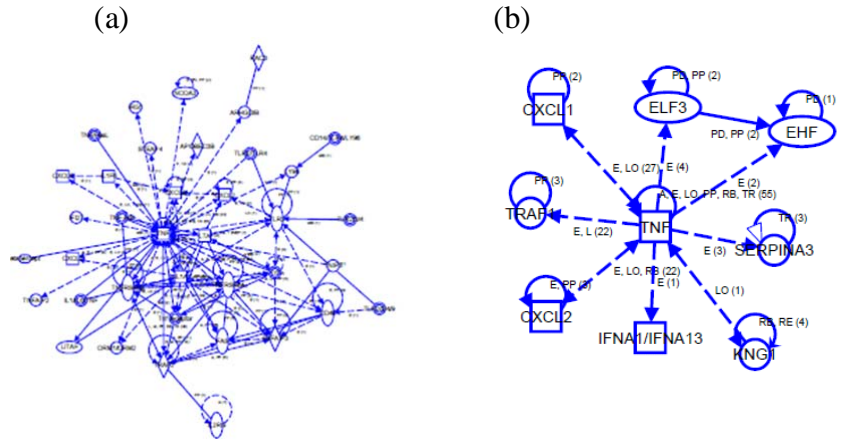
entails intervening in vitro culturing of the cells to make transplantable spheroids. Invariably, each subsequent passage grows faster on the pseudo-organ, with much less initial cell death. This means that the cells growing in culture retain genetic and epigenetic features that allow them to grow on the pseudo-organ with shorter lag times, and this meant to us that gene expression analysis on the cultured cells might be worth doing. The benefits of working with cultured cells include that a single cell population can be used without significant contamination from other cell lines, which is a condition that is extremely hard to avoid when using microdissected tissue, and significant mass, which avoids needing amplification steps that can, in fact, always do, introduce error. The disadvantage is, of course, that the “snap shot” of gene expression is less relevant to the in vivo environment. Note, however, that candidates from the cell culture experiment can be tested very reliably by going back to the tissue, and that a work plan going in this direction is far simpler and more robust than direct analysis of tumor tissue.

We expanded cells from the first passage (Chamber model 1 or CM1) of an H2b-GFP Movcar tumor, and did gene expression analysis using Affymetrix microarrays comparing unadapted (CM) to the CM1 adapted cells. The strength of this analysis derives from comparison with gene expression analysis in a parallel experiment involving the breast cancer cell line N202. That experiment is farther along than the ovarian project because we did not have the hemorrhaging problem. In **Figure 3**, we show, in the N202 experiment in which N202 cells are growing on pseudo-lung, *Tnf*, which is the mouse homolog of human TNF-alpha, is highly implicated in tumor cell adaptation. Not shown are similar results implicating *Tnf* when N202 cells grow on bone marrow. In **Fig. 3b**, however, MOVCAR cells growing on ovary do not adapt by a mechanism that involves overexpression of *Tnf*. Kim et al. [1] showed that Lewis lung carcinoma cells activate macrophage by secreting the proteoglycan versican, and the macrophage, in turn, secrete TNF-alpha and IL6. The mortality of *Tnf*^{-/-} mice upon tail vein injection of LLC cells was markedly reduced, implying that *Tnf* is required for metastasis, and biological arguments suggest that *Tnf* exerts its role by conditioning the metastatic microenvironment. Here, we apparently have a cell line that has learned to secrete *Tnf* without the macrophage intermediate. MOVCAR cells *do not* use this mechanism, and we hypothesize that this is because, in this experiment, the MOVCAR cells are growing on their native tissue of origin (i.e. ovary), whereas the N202 cells have been forced to adapt to what is essentially a metastatic environment. In other words, the N202 cells recognize the metastatic environment as “foreign” and have adapted via enhancement of factors normally associated with innate immunity. The suggestion, then, is that if we force MOVCAR cells to adapt to a tissue other than ovary, that we may also see adaptation involving *Tnf*. It is also possible, however, that MOVCAR cells adapted to tissue of a metastatic site do so indirectly, in which case, we can use the conditioned medium strategy of Kim et al. [1] to track this down.

of adaptation. This adaptation is important because it involves the genetic and epigenetic alterations that must take place for a cancer cell to be able to grow in the foreign environment of the metastatic site: by identifying the changes in gene expression, the essential adaptations are revealed. In turn, the genes behind these essential adaptations become potential targets for therapeutics to block metastasis. Adaptation in our system requires several passages of the tumor cells from animal to animal, and this

Here, we briefly summarize a few of the more obviously interesting genes in our first run of this experiment on the adapted MOVCAR tumors. In this discussion, CM0, 1, 2, 3, etc. refer to passages 0, 1, 2, and 3, etc. in the animal, and in the manuscript presented below, we use P0, 1, 2, 3, etc. using “P” interchangeably with “CM”. Genes were sorted according to the most extremely upregulated upon adaptation. The most extremely differentially expressed gene after adaptation was **Slfn3** (26-fold over-expressed), and very little is known about it. Second on the list, however, is **Il2rg** (interleukin 2 receptor gamma), which is 19-fold overexpressed in CM1 relative to CM0. Il2rb is 4-fold higher, whereas Il2ra is not altered (0.9 fold). Il2rg is the common gamma chain important in signalling from a number of interleukins, including 2, 4, 7 and 21, and activates JAK3, and therefore the JAK-STAT pathway. Constitutive activation of JAK3 is observed in colorectal cancer, and repression of JAK3 leads to apoptosis [2]. JAK3 is constitutively active in acute lymphoblastic B-cell leukemia [3], and is considered a potentially viable target for drug development for leukemia. It is also upregulated, along with Il2ra and Il2rb in infiltrative human breast cancer[4]. *Our result is consistent with the possibility that gene amplification of Il2rg may constitutively activate JAK3, and if it generalizes to human ovarian cancer, suggests that such kinase inhibitor development may also apply to ovarian cancer.* IL2RG has been shown to be highly expressed in 3 out of 12 ovarian adenocarcinomas; therefore, we may have devised a model for this type of ovarian cancer. The next logical step will be to determine whether this gene is amplified at the DNA level. However, before we embark on gene-by-gene analyses, we will want to extend these experiments to later steps in adaptation.

These CM1 cells have gone quite far in avoiding apoptosis. **Nlrp1b** is a pro-apoptotic gene that forms part of the caspase-1-activating complex known as the inflammasome. In MOVCAR cells that have adapted for growth on pseudo-ovary tissue, Nlrp1b is over-expressed relative to the unadapted cell line by a factor of ~8. NLR proteins are thought to be “pattern matching” proteins that detect infectious agents as part of the innate immune system, and may also respond to stress; Nlrp1b is known to mediate cell death in response to anthrax toxin. The pro-apoptotic activity of Nlrp1b is opposed by Bcl-2 and Bcl-XL (Bcl2l1), which bind to Nlrp1b, and prevent its recruitment of caspase-1. In MOVCAR, 11 out of 19 NLR family members are over-expressed by at least a factor of 2, the highest being Nlrp1b at 8-fold, and the second being Nlrp3 at 4.5-fold. Interestingly, many Bcl-2 family members (8/14) are also over-expressed by at least a factor of 2, suggesting that an aspect of the growth of these ovarian cancer cells in pseudo-ovary tissue may be that the Bcl-2 family is opposing natural tumor suppressor activities of Nlrp1b. Importantly, we think, Il2rg + Il2rb, both of which are overexpressed, induce Bcl-2 and Bcl2l1 expression, and, indeed, these are over-expressed 2.6-fold and 2-fold, respectively. It is as if there is a battle raging with Nlrp1b trying to induce apoptosis while Il2rg is opposing apoptosis and winning. Interestingly, in comparison with GEO, human NLRP1 is highly expressed in ovarian cancer and in ovarian endometriosis.



Other genes are intriguing. **Cxcl1**, otherwise known in humans as GRO α , is >11-fold over-expressed in ovary-adapted MOVCAR cells. This is interesting because Cxcl1 has been shown to induce proliferation in epithelial ovarian cancer cells by transactivation of the EGFR [5]; it is overexpressed in gastric cancer[6]; it promotes angiogenesis and invasion in gastric cancer [7]; and may mediate tumor invasion in bladder cancer[8]. CA125 is only mildly up-regulated (1.4-fold), but other mucins are highly upregulated (Muc19, 5-fold). March8 is 3-fold up-regulated, Hnrnpa0 is 1.7-fold up-regulated, and others identified in microarray analysis of human tumors. Myc is 2-fold up.

As we mentioned above, we have had significant unanticipated obstacles to overcome in the form of ovulation and mCherry toxicity, and at times we despaired that there may be no way around these problems. However, both problems yielded to relatively simple solutions, but these have slowed down our progress. Note that each of these cycles requires one week of organ tissue revascularization, three weeks of tumor growth, and two consecutive weeks of in vitro cell growth separated by cell sorting. In the present cycle, we encountered yet another unanticipated obstacle. After MOVCAR cells adapted for one round, yielding the gene expression data discussed above, we placed the tumors back into culture in order to expand them and carry them on to the next stage.

The cells survived in culture, but would not sit down on the plastic and grow, although they continued to live for more than three months. We tried mincing, trypsinization, growth on collagen, growth in soft agar, and growth on a “feeder” layer of fibroblasts, and all of our attempts failed. We placed them back into the mouse with minced ovarian tissue, and learned that they were still able to grow. In parallel, however, we learned that each adaptive series can be unique; that sometimes growth in culture is initially very slow and sometimes fast, and that some adaptive series resemble others at different time points.

Therefore, we have begun this adaptive series again, hoping that the original experiment resulted in the chance selection of a clone that will not grow in vitro and that we will achieve growth with other adaptive series. If this does not work, we will shorten the adaptation time so that the cells spend a greater amount of time, relatively, growing in vitro. In other words, we will force the cells to co-adapt to growth in vivo and in vitro. Thus, with this new series, we will recover tumors after 7 and 14 days rather than after 21 days and place them back in vitro.

An implicit part of these experiments is data interpretation, and it occurred to us that analysis of time course data on tumor development is unprecedented, which compelled us to begin to work on the problem in anticipation of time course data from the MOVCAR experiment. We already had in hand a set of data from N202 cells growing on brain tissue. These efforts are relevant to the ovarian cancer case in two senses: first, we needed to work out a bioinformatics strategy, and second, because metastasis of ovarian cancer to the brain is a particularly undesirable outcome. We have gained a novel finding, that metastasis to brain tissue of a cancer cell line is accompanied initially by expression of genes of an ostensibly neurological gene expression phenotype; and to the extent that our findings are general, we would suggest the use of c-kit inhibitors to prevent brain metastasis in patients with metastatic disease. Below, we present a manuscript with the tentative title, “*Cancer adaptoemes: gene expression requirements for cancer cell growth in foreign tissue microenvironments*”, that is very near completion. We feel that the results of this informatics effort funded by the current grant is of immense medical importance: it is the first study that shows that metastatic cancer cells adopt gene expression patterns characteristic of the host tissue in which it finds itself, and it shows clearly that prevention of metastasis in at-risk cases might be achieved by interfering with this initial adaptive phase. It further shows that, while placing different tumors on a time line based on hierarchical clustering does not work, there is a fascinating potential option that real tumors could be placed on a time line established by experimental tumors. In short, the different “subtypes” of tumors so often recognized in gene expression data may actually be tumors developing along the same time line but stochastically stalled at different points. The easiest indicator of this can be seen in Figure 3, frame 6, where considerable differential gene expression is observed, followed by return to baseline, in which case, hierarchical clustering would place points P3 and P4 close to P1 (which is wrong).

We have one more month of funding on this proposal, and we hope to be able to obtain sufficient funding to continue with this model for ovarian cancer. We think we will have sufficient resources from other sources to complete two adaptive series, and, once completed, will serve as the basis of an analysis such as that presented for N202 cells.

TASK 1

1. Development of H2b-GFP-MOVCAR cells
2. Development of a H2b-GFP-MOVCAR/Tomato pseudo-organ model for ovarian cancer

Completed by the end of the first year.

TASK 2

1. Solving the ovulation/hemoraging problem with progesterin. **Completed in the second year.**
2. Intravital microscopy studies implanting different stroma, i.e., ovary, skin, lung and liver with and without H2b-GFP-MOVCAR cells using the Tomato pseudo-organ model. **The first and second training cycles on ovary are now complete for one series. We now expect that co-adaptation to in vivo and in vitro growth may be necessary to carry cells through a series of training cycles. This will be achieved by shortening the in vivo adaptation period. We are proceeding with available resources. We plan to perform gene expression analysis on at least two adaptive series using the resources still available from this grant and private resources.**
3. Microdissection to isolate tumor and stroma. **We now use growth in cultured cells.**
4. Gene expression on sorted, cultured CM1. **We now have two series through CM1, one of which was carried through CM2 but would not grow in vitro. We will test this with the second series. If this, too, does not grow in vitro, we will begin again, but shorten the in vitro adaptation period to obtain cells that have not lost their ability to grow in vitro. We plan to repeat this and carry these experiments through to CM4 for at least two series, with the caveat that shorter adaptive periods may lead to series being carried out until CM12.**

TASK 3

1. **We propose** to continue with the gene expression in sorted, cultured adapted cells as this appears to be revealing some genes that are already known to be differentially regulated in ovarian cancer.
2. Microarrays and data analysis on stroma and tumor. **We are still trying to overcome the problem of loss of an in vitro growth phenotype, as outlined above.**
3. Our original plan was to breed (B6.129(Cg)-Gt(ROSA)26Sortm4(ACTB-tdTomato,-EGFP)Luo/J)^{nude} mice for Aim 2, in which we isolate cells of the immune system to subject to microarray analysis. This breeding is not necessary, because we have learned to use T-cell filtration during bone marrow transplantation. **We will not make progress on this aim.**
4. In situ hybridization and immunohistochemistry in human tissues. **We will not make progress on this aim.**

In the Appendix, we present a manuscript that is near completion “Cancer adaptomes: gene expression requirements for cancer cell growth in foreign tissue microenvironments”, and we have attached two additional publications that were partially or indirectly supported by the present grant.

Realistically, with the resources remaining in this grant and a few extra resources from other sources, we expect to be able to solve the growth in vitro problem using shorter in vivo training periods and perform gene expression analysis on at least two MOVCAR adaptive series. This will be sufficient to publish the results, and notify the ovarian cancer community of the properties of the animal model. This project did not work out the way we expected, but we have made significant progress in a very difficult area, and we believe the model is a short step away from viability for MOVCAR. It should be noted that this property of MOVCAR cells refusing to attach to plastic is unprecedented relative to dozens of different cell lines we have tried, and therefore this outcome was wholly unexpected. Nevertheless, as CM1 sits down on plastic, we think the shorter training period strategy is bound to succeed.

KEY RESEARCH ACCOMPLISHMENTS

- Development of a H2b-GFP-MOVCAR cell line
- Development of a H2b-GFP-MOVCAR/Tomato pseudo-organ model for ovarian cancer: specifically, we have overcome the mCherry problem and we have overcome the ovulation-dependent hemorrhaging problem.

- Gene expression analysis after the first training cycle.
- Developed a web-based informatics framework that uses gene ontology to identify major adaptive features.

REPORTABLE OUTCOMES

- The H2b-GFP-MOVCAR cell line deserves to be made publically available, as it is likely to be useful in ovarian cancer research using diverse strategies.
- The H2b-GFP-MOVCAR/Tomato pseudo-organ ovarian cancer model is reportable without much additional refinement, and we are preparing a manuscript. We need a few high-quality FFPE images.
- Our gene expression analysis shows that cells retain a pattern of differential gene expression from training even after they have been expanded briefly in culture. We will report this in a publication, but we first want gene expression analysis in other pseudo-organs to test the hypothesis that the cancer cells autonomously activate components of the innate immune system when they find themselves in the wrong tissue environment.
- A web-accessible tool for reporting outcomes of adaptation experiments, currently applied to our larger parallel dataset for N202 adaptation: see www.voxvill.org/100.IVM/100.IVM.index.php.

CONCLUSIONS Prior to this project, we had devised pseudo-organ models for lung, liver, brain, bone marrow, breast, and prostate and anticipated that we would encounter no significant problems with essentially any other tissue. The toxicity of mCherry to MOVCAR cells aside, this assumption was incorrect; it simply had not occurred to us that ovary would present its own set of unique problems. Not only did ovulation-dependent hemorrhaging present a problem, but control of that through hormone therapy presented its own set of problems vis-à-vis the effect of progestin on ovarian tumor growth. It was fortunate that a dose of progestin could be found that both suppressed ovulation and permitted tumor growth, for without this result, IVM would not be possible on pseudo-ovaries. These are relatively long-term experiments, such that when problems occur, the time frame can be seriously upset. We have been unable to coax CM2 cells to grow in vitro, but our experiments indicate that clonal selection can result in significantly different outcomes in a stochastic manner. We have also had the interesting idea that shorter adaptive times in vivo may allow us to preserve in vitro growth.

REFERENCES All of the appropriate references are contained in the first manuscript in the Appendix.

APPENDIX

Cancer adaptomes: gene expression requirements for cancer cell growth in foreign tissue microenvironments

Gaelle Rondeau¹

Parisa Abedinpour¹

Prerak Desai¹

Veronique Baron^{1,2}

Per Borgstrom^{1,2,4}

John Welsh^{1,3,4}

¹Vaccine Research Institute of San Diego

²Pelficure, Inc.

³San Diego Institute of Biological Research

Summary

The migration of cells into novel microenvironments occurs frequently during normal development and during the progression of cancer. In these processes, signals from the host tissue alter gene expression in the migrated cells, and vice versa. Normal cells adapt by adjusting gene expression and altering their epigenetic state, as do cancer cells, which have additional adaptive plasticity due to genomic instability. We studied changes in gene expression when cancer cells adapt to grow on brain, bone marrow, and lung tissue implanted and maintained in an *in vivo* culture system. We observed the temporary induction of genes characteristic of the host tissue and slow growth, followed by evolution away from this phenotype and rapid growth.

Cell-autonomous factors and external factors supplied by the local microenvironment control gene expression during development [9, 10] and when cells are placed in novel tissue microenvironments for investigative purposes [11-15]. Cancer cells respond to signals present in their local microenvironment [16], and reciprocally alter gene expression in the local stroma [17]. We asked whether cancer cells express genes characteristic of the surrounding tissue when embedded in a foreign tissue microenvironment.

Minced tissues implanted in dorsal skinfold chambers survive and revascularize, yielding substrates upon which tumor cells can be grown [18]. We prepared brain, bone marrow, and lung tissues in this manner and implanted the murine breast cancer cell line N202. Three weeks after *in vivo* seeding, cells from the resulting N202 tumors were grown briefly *in vitro*, sorted, grown again, and reintroduced into the *in vivo* culture system for up to four cycles.

Cells grown in this manner on brain tissue for four cycles initially grew more slowly *in vitro* than the parental cell line, but eventually surpassed the initial growth rate, and growth *in vitro* and *in vivo* correlated well (**Figure 1a-c**). In bone marrow, a steady increase in growth rate was observed both *in vitro* and *in vivo* (**Figure 1d-f**), also with strong correlation, whereas in lung correlation was poor.

Gene expression profiles for parental cells (P0) and passages 1-4 (P1-P4) were generated from the *in vitro* cell cultures. **Figure 2** shows kmeans groups for cells grown on brain tissue at times P0-4 assuming 25 kmeans groups. Kmeans groups for brain, bone marrow and lung are designated “BN_N X”, “BM_N X”, and “LN_N X”, respectively, where N refers to the number of kmeans groups and X refers to the specific group. Statistically significant GO Biological Process Terms (www.geneontology.org) associated with each kmeans group were determined and are italicized in the text. Corresponding GO IDs are listed in **Table 1**, with p-values from Fisher’s exact test [19] corrected to indicate false discovery rates (q-values) [20]. These analyses can be explored in further detail at www.voxvill.org/100.IVM/100.IVM.index.php.

Homeostasis **Figure 2** shows kmeans groups of genes that are differentially expressed at sequential times during N202 cell adaptation to brain tissue. The most significant GO terms in **BN₂₅ 6**, which contains genes that are sharply up-regulated in P1 and P2, are *sodium ion transport*, *L-amino acid transport*, and *ion transport* (**Table 1**). *Ion transport*, *anion transport*, and *ATP hydrolysis coupled proton transport* are significant in **BN₂₅ 15**, *iron ion homeostasis* and *arginine transport* are significant in **BN₂₅ 18**, and *amine transport* is significant in **BN₂₅ 19**, all of which contain genes that are sharply up-regulated in P1 and P2. The genes associated with these GO annotations can be found in **Table S1**. These results indicate that the cells must first solve problems related to material homeostasis when placed in this novel tissue microenvironment. Similar responses occur in lung, e.g. genes for *ion transport* are initially up-regulated in **LN₂₅ 23**.

Using a higher number of kmeans groups allows one to focus on a more detailed behavior, in this case up-regulation specifically in P1. In **LN₄₉ 28**, *transmembrane transport* is the most significant GO term. The importance of ion homeostasis in adaptation to bone marrow can be seen most easily in **BM₄₉ 12** and **BM₄₉ 41**, where ion transport is significant due to initial up-regulation of *Slc38a1*, *Slc31a2*, *Cachd1*, and *Steap4* in the former and *Slc1a5* in the latter. All of these are initially up-regulated in bone marrow and lung but not in brain.

Cell Cycle and cell morphology Gene expression in **BN₂₅ 2, 4, 5, 16, 20, and 25** is repressed during P1 and P2, during which time cell growth is slow and cell morphology is relatively simple, whereas expression in **BN₂₅ 6, 13, 15, 18, 19, and 24** is elevated during this initial phase and anti-correlated with growth rate and morphological complexity (**Figs. 1 and 2**). **BN₂₅ 4**, which reaches its lowest point at P2 when cell cycle is at its slowest, contains significant GO terms most directly related to cell cycle (**Table 1**). During adaptation, cell shapes became less complex in P1 and P2, and then became more complex in P3 and P4 (**Figure 3**), reflecting cytoskeletal processes regulated by Rho GTPases [21, 22]. These are enriched in **BN₂₅ 2** and **BN₂₅ 4**, consistent with the timing of changes in proliferation and morphological complexity (see **Table 1**). >32-fold up-regulation places the *Kit* oncogene from **BN₂₅ 19** among the most highly up-regulated genes observed in these experiments, although here, *Kit* oncogene does not drive rapid growth.

Brain specific induction N202 cells transplanted on brain tissue initially express genes characteristic of the brain tissue microenvironment. **Table 2** lists significant (qval ≤ 0.05) GO Biological Process Terms from the kmeans groups in which genes were initially up-regulated or down-regulated in P1 by at least a factor of 1.5, using N=25. Thirty-nine (39) genes associated with significant neurobiology-related GO Biological Process Terms were up-regulated in P1, whereas 23 were down-regulated. With N=36, 49 up-regulated and 23 down regulated genes associated with significant neurobiology-related GO Biological Process Terms were detected, as shown in **Table 3**. Induction or repression of neurobiological processes is more pronounced in the first passage in brain tissue than in bone marrow or lung. Induction of genes involved in neurobiological processes

exceeds repression by a substantial margin in adaptation to brain tissue, unlike the case for bone marrow or lung.

Activation of *Epha4*, associated with *negative regulation of axon regeneration*, and *Lrrk2*, associated with *negative regulation of neuron maturation* and *negative regulation of branching morphogenesis of a nerve* repress neuron-like differentiation. Most repressed genes associated with neurobiological functions represent functions that, if activated, would suppress a neurobiological phenotype. However, among these are several for which repression promotes neuron survival, including *Map3k11*, *Bcl2l11*, *Casp9*, *Ptprf*, and *Cdc42*, associated with *positive regulation of neuron apoptotic process*. In balance, N202 cells respond to the brain tissue microenvironment by expressing a variety of genes that perform neurobiological functions. Typically, this behavior persists through P1 and P2, and desists in P3 and P4, whereupon the cells begin a more rapid growth phase.

Some of the genes in **BN₂₅ 6, 8, 18, and 19** are induced in P1 by ≥ 4 -fold and perform neurobiological functions, but are not associated with enriched GO annotations, which we list here together with functional pointers: *Atp1b1*, electrical excitability [23]; *Chi311*, neuroectoderm differentiation [24] and self-transcendence in schizophrenia [25]; *Chrm3*, acetylcholine effects [26]; *Cldn1*, fibroblastic meningioma [27]; *Prss12*, synaptic function [28]; *Slc38a1*, glutamate transport [29]; *Syne1*, cerebellar ataxia [30]; *Tmem47*, occurs at high levels in dog brain [31]; *Ugt8a*, transfers galactose to ceramide [32]; *Zc4h2*, mental retardation [33]; *Kctd12b*, GABA(B) receptor subunit [34]; *Lrrk2*, Parkinson's disease [35]; *Maoa* [36] and *Moxd1* [37] modify dopamine levels; *Neto2*, glutamate signaling [38, 39]; *Nr4a2*, Parkinson's disease [38], schizophrenia, and manic depression [40, 41]; *Pcdh7*, cell-cell interactions in the developing brain [42]; *Pgap1*, otocephaly [43]; *Slc1a1*, post-synaptic glutamate neurotransmitter activity and schizophrenia [44] and obsessive compulsive disorder [45, 46]; and *Slit2*, brain vessel density and permeability [47].

This suggests that the N202 cells initially detect signals characteristic of the brain microenvironment. The cells eventually evolve away from this phenotype and toward a more rapid growth phenotype. In a biological replicate experiment, genes associated with neurobiological functions and induced in P1 and P2 in the first experiment (**Table 1**) were similarly induced in the replicate experiment by a $\sim 2:1$ margin (27:13 and 25:15, induced vs. repressed, respectively). Among genes that were repressed in the first experiment, most were repressed in P1 in the replicate experiment (5:19, induced vs. repressed), but many of these returned to baseline or above by P2 (15:9, induced vs. repressed), similar to the latter stage, P3 in the first experiment. Genes from **BN₂₅ 5** in the replicate experiment were induced immediately, rather than exhibiting the two-cycle delay of the previous experiment. Modeling indicated that replicate P1 and P2 corresponded most closely with times P2.6 and P3.8 in the original time series (**fig. S6**). Such variation in timing would be expected of adaptation driven by stochastic processes.

Functions associated with bone marrow are characteristic of inflammation and cannot be used as evidence of orthotopic gene expression. Nevertheless, their absence would comprise a conspicuous failure of the hypothesis. Indeed, genes associated with bone marrow and with inflammation are expressed when N202 cells are placed in contact with bone marrow. In **BM₂₅1**, *Tlr2*, *Ripk2*, *Myd88* are initially up-regulated, and regulate inflammatory responses [48], such as *positive regulation of interleukin-6 production*, *MyD88-dependent toll-like receptor signaling pathway*, and *positive regulation of tumor necrosis factor production* (see www.voxvill.org/100.IVM/100.IVM.index.php). *Immune response* due to *Csf3*, *Cxcl5*, and *Cxcl1*, and *inflammatory response* due to *Itgb6*, *Cxcl5*, and *Cxcl1*, are up-regulated in P1 of **BM₃₆25**. Several genes that change in P1 have functions in bone unrelated to inflammation, per se. In **BM₂₅1**, *Adams1* is important in inflammation, but also in normal bone physiology [49] and metastasis to bone [50]. *Alp1* is a tissue-specific alkaline phosphatase expressed in bone, liver, and kidney [51]. *Nr4a2* can be induced in bone-marrow-derived mesenchymal stem cells [52]. *Bcl9* is up-regulated in osteoarthritis [53]. *Sfrp1*, and *Tob1* and *Sfrp1* are associated with significant GO terms *bone trabecula formation* and *negative regulation of osteoblast differentiation*, respectively. *Stc2* controls bone growth [54]. *Loxl4* is up-regulated in bone marrow but not brain and lung, and is involved in crosslinking collagen. In **BM₃₆22**, in which genes are up-regulated only in P1, *hemopoietic progenitor cell differentiation* is significant due to *Fst* and *Sfrp1*, as are *negative regulation of bone remodeling*, *negative regulation of osteoclast differentiation*, *convergent extension involved in somitogenesis* and *bone trabecula formation*.

Inflammation and Innate immunity

Characteristics of P1 and P2 include innate immune system functions, such as *opsonization*, *chemotaxis*, *positive regulation of macrophage activation*, *positive regulation of phagocytosis* and others from genes initially up-regulated in **BN₂₅ 19**. In **BN₂₅ 15**, genes are induced in P1 and P2 and return to control levels by P3, and concern *response to endoplasmic reticulum stress* and *endoplasmic reticulum unfolded protein*

response. Concordantly, anti-apoptotic Bcl2, which is found in **BN₂₅ 6** and protects against endoplasmic reticulum stress[55], is at its highest level in P2, and has been associated with B-cell lymphomas[56] and other cancers [57]. Endoplasmic reticulum-related stress signifies that normal protein trafficking is disrupted during the first two passages and then resolves coincidentally with an increase in growth rate. **BN₂₅ 25**, contains genes that are responsible for *peptide transport* and *proteolysis*, and *innate immune response*.

Angiogenesis Angiogenesis promotes tumor survival and growth, and in this pseudo-orthotopic model, neovasculature arises from pre-existing vasculature in the local stromal tissue[18]. In **BN₂₅ 20**, in which genes are sharply *down-regulated* during P1 and P2, and then rebound in P3 and P4, Plau, Col8a1, and Nrp1 are associated with *angiogenesis* and Ddah1, promotes endothelial cell proliferation [58]. In **BN₂₅ 25**, Adamts1 and Sema4a, associated with *negative regulation of angiogenesis*, are sharply down-regulated. None of these genes is similarly regulated in the bone marrow or lung tissue microenvironments. In **BN₂₅ 17**, Eya1 and Hey1, regulate sprouting angiogenesis[59], are associated with *positive regulation of Notch signaling pathway*, and are strongly down-regulated in all three tissues. Nevertheless, revascularization in all three tissues is robust (**fig. S5A, and S5B**), indicating that these functions derive from the three tissue microenvironments, and not from the tumor cells. The tumor cells adapting to brain tissue do provide several pro-angiogenic functions temporarily, e.g. in **BN₂₅ 15**, Plxnd1, Vangl2, Fzd2, Fzd5 and Vegfa promote *patterning of blood vessels* and *vascular development*.

Closing comments

These data show that cancer cells implanted in foreign tissue microenvironments can initially respond by expressing genes typical of the cells that comprise the microenvironment. Genes in this early response class represent potential therapeutic targets to delay or prevent brain metastasis using drugs already in use for other purposes, including Alpl, Arg2, Bcl2, C3, Chrm3, Kit, Maoa, and Odc1. Treatment with these agents may interfere with early adaptation to the extent that over-expression of any of these genes is important to cell survival or progression. A few genes that can be inhibited by known drugs or chemicals are up-regulated at early times and persist or are up-regulated at later times, including Alpl, Plat, and Pnp. At least three drugable genes are initially down-regulated by the brain tissue microenvironment and then return to control levels, and if this return to control levels is required for more aggressive growth these genes might be of therapeutic interest: Hdac1, Jun, and Vdr. Drugs that inhibit these genes can be seen in www.voxvill.org/100.IVM/100.IVM.index.php and in **Table S3**.

The use of in vitro cultivation of FAC-sorted tumor cells relieves concerns that orthotopic gene expression measurements may be compromised by host tissue contamination, which is difficult to rule out in gene expression analysis of resected natural tumors. Also, while the experimental tumors, themselves, are serially transplanted, the organ tissue is not, thereby precluding any long-term adaptive response on the part of the microenvironment. Many other adaptive responses that occur in the serially transplanted tumor cells, including associations with stress and wound healing, innate immune responses, changes in metabolism and others, can be explored further at www.voxvill.org/100.IVM/100.IVM.index.php.

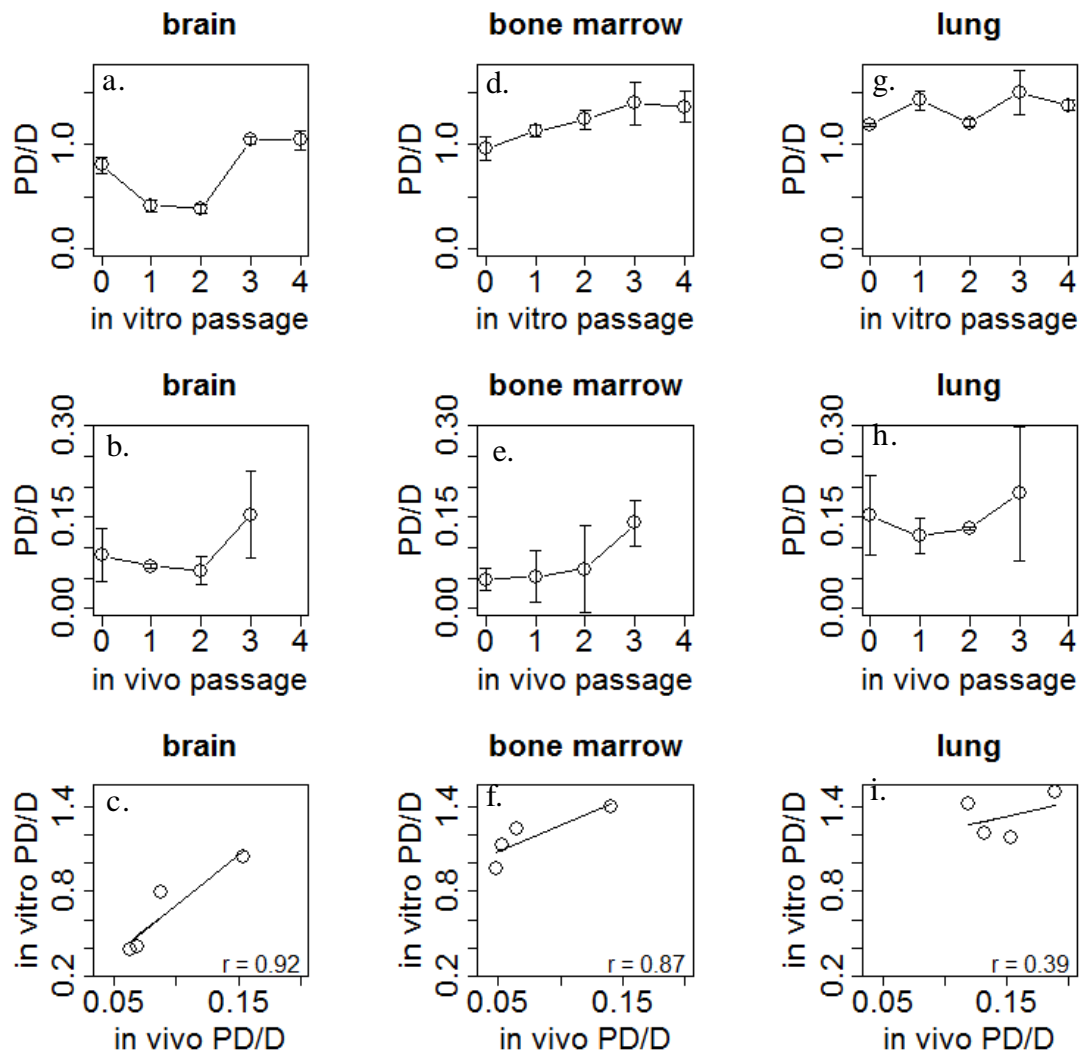


Figure 1. (a, d, g) In vitro rates population doubling per day (PD/D) for cells grown from in vivo passages 0-4 for brain, bone marrow, and lung tissue, respectively, and 3 independent measurements per time point. Error bars represent one standard deviation. (b, e, h) In vivo growth rates, 2 animals per measurement. Error bars represent one standard deviation. (c, f, i) Correlation between in vitro and in vitro growth rates; r is Pearson's correlation. (Note that the cells of the final time point were not transferred into the chamber, and therefore the second row has one fewer time point than the first).

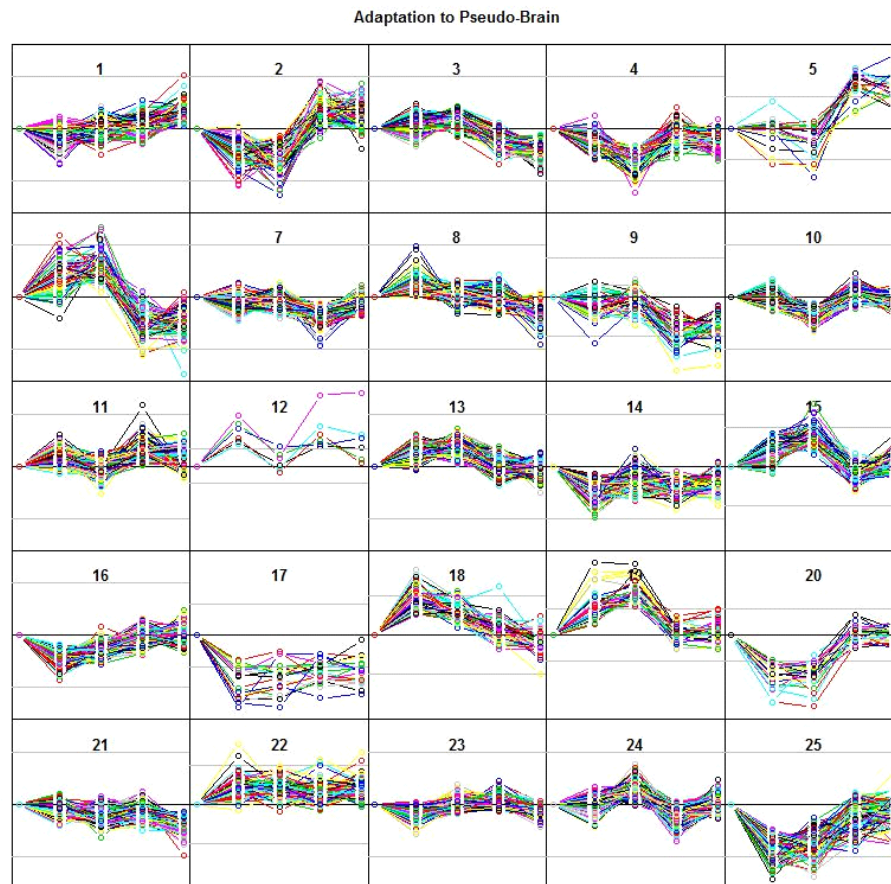


Figure 2. Adaptation of N202 cells to brain tissue. N=25. Gray lines represent 4-fold changes. Horizontally, positions represent sequential in vivo passages, and gene expression analysis was performed on cells from each of these passages expanded in vitro.

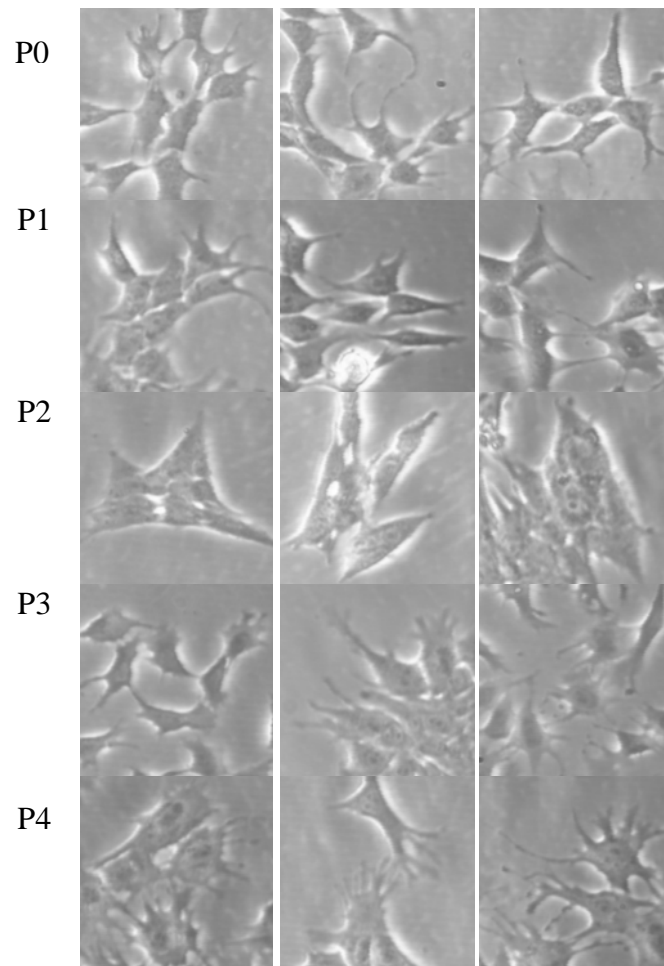


Figure 3. Cell morphology during adaptation to brain tissue. **(P0)** The parental cell line has short dendritic projections. **(P1)** Cells after the first passage become slightly less dendritic. **(P2)** After the second passage, cells have very few dendritic projections. **(P3)** Cells of P3 have numerous, stumpy dendritic extensions, and this phenotype is somewhat more pronounced in **(P4)**.

Table 1. Significant GO Biological Process Terms in Adaptation of N202 Cells to Brain Tissue				
Function	KMG	GO ID	GO Biological Process Term	qval*
Homeostasis	BN ₂₅ 6	GO:0006814	sodium ion transport	0.0006
		GO:0015807	L-amino acid transport	0.0008
		GO:0006811	ion transport	0.0009
		GO:0003333	amino acid transmembrane transport	0.006
	BN ₂₅ 15	GO:0006811	ion transport	0.008
		GO:0006820	anion transport	0.03
		GO:0015991	ATP hydrolysis coupled proton transport	0.004
	BN ₂₅ 18	GO:0055072	iron ion homeostasis	0.0009
		GO:0015809	arginine transport	0.042
	BN ₂₅ 19	GO:0015837	amine transport	0.018
Cell cycle, motility, and morphology	BN ₂₅ 2	GO:0032321	positive regulation of Rho GTPase activity	0.001
		GO:0030036	actin cytoskeletal organization	0.003
		GO:0032956	regulation of actin cytoskeleton organization	0.016
		GO:0051017	actin filament bundle assembly	0.019
	BN ₂₅ 4	GO:0007049	cell cycle	7x10 ⁻¹¹
		GO:0051301	cell division	4x10 ⁻⁷
		GO:0007067	mitosis	2x10 ⁻⁶
		GO:0006260	DNA replication	8x10 ⁻⁶
		GO:0007076	mitotic chromosome condensation	4x10 ⁻⁷
		GO:0006281	DNA repair	0.0002
		GO:0030261	chromosome condensation	0.0004
		GO:0007059	chromosome segregation	9.66x10 ⁻⁴
		GO:0006334	nucleosome assembly	0.001
		GO:0006487	protein N-linked glycosylation	0.002
		GO:0006284	base-excision repair	0.006
		GO:0007099	centriole replication	0.009
Angiogenesis	BN ₂₅ 15	GO:0001569	patterning of blood vessels	0.004
		GO:0001944	vascular development	0.004
	BN ₂₅ 17	GO:0045747	positive regulation of Notch signaling pathway	0.0005
	BN ₂₅ 20	GO:0001525	angiogenesis	0.003
	BN ₂₅ 25	GO:0016525	negative regulation of angiogenesis	0.03
Protein dynamics and Innate immunity	BN ₂₅ 15	GO:0034976	response to endoplasmic reticulum stress	0.001
		GO:0030968	endoplasmic reticulum unfolded protein response	0.006
	BN ₂₅ 19	GO:0008228	opsonization	0.0003
		GO:0006935	chemotaxis	0.0004
		GO:0043032	positive regulation of macrophage activation	0.0007
		GO:00507866	positive regulation of phagocytosis	0.002
	BN ₂₅ 25	GO:0015833	peptide transport	0.008
		GO:0006508	proteolysis	0.01
		GO:0045087	innate immune response	0.02

Table 2. Induction of neurobiological functions in N202 cells implanted with brain tissue.
qval ≤ 0.05, N = 25, P1 Ratio ≥ 1.5-fold

GO ID	GO Biological Process Term	KMG	+/-	Gene
GO:0048846 GO:0021972 GO:0033563 GO:0090260 GO:0021836	axon extension involved in axon guidance, corticospinal neuron axon guidance through spinal cord, dorsal/ventral axon guidance, negative regulation of retinal ganglion cell axon guidance, chemorepulsion involved in postnatal olfactory bulb interneuron migration	6	+	Slit2
GO:0046928	regulation of neurotransmitter secretion	6	+	Celsr1
GO:0001941	postsynaptic membrane organization	6	+	Chrnbl
GO:0007411	axon guidance	9	+	Epha4 Etv1 Gli3 Sem5a
GO:0097156 GO:0097155 GO:0048681 GO:0008347 GO:0048710	fasciculation of motor neuron axon, fasciculation of sensory neuron axon, negative regulation of axon regeneration, glial cell migration, regulation of astrocyte differentiation	9	+	Epha4
GO:0007399	nervous system development	9	+	Epha4 Sem5a Sem7a
GO:0035633 GO:0032227 GO:0031915 GO:0051968 GO:0019233 GO:0007613	maintenance of blood-brain barrier, negative regulation of synaptic transmission, dopaminergic, positive regulation of synaptic plasticity, positive regulation of synaptic transmission, glutamatergic, sensory perception of pain, memory	12	+	Ptgs2
GO:0008090	retrograde axon cargo transport	13	+	Dst Ndel1
GO:0050905	neuromuscular process	13	+	Agtppb1 Atxn2 Hoxa1
GO:0090177	establishment of planar polarity involved in neural tube closure	15	+	Vangl2
GO:0090179	planar cell polarity pathway involved in neural tube closure	15	+	Vangl2 Fzd2
GO:0032902	nerve growth factor production	15	+	Pcsk6
GO:0033603	positive regulation of dopamine secretion	15	+	Slc18a1
GO:0050953	sensory perception of light stimulus	15	+	Myo7a
GO:0043382	positive regulation of memory T cell differentiation	15	+	Il23a
GO:0021952 GO:0001764	central nervous system projection neuron axonogenesis, neuron migration	18	+	Nr4a2 Dclk1
GO:0021953 GO:0042416 GO:0042053	central nervous system neuron differentiation, dopamine biosynthetic process, regulation of dopamine metabolic process	18	+	Nr4a2
GO:0014043 GO:2000173 GO:0060161 GO:0022028	negative regulation of neuron maturation, negative regulation of branching morphogenesis of a nerve, positive regulation of dopamine receptor signaling pathway, tangential migration from the subventricular zone to the olfactory bulb	18	+	Lrrk2
GO:0042135 GO:0042420	neurotransmitter catabolic process, dopamine catabolic process	18	+	Maoa
GO:0010975	regulation of neuron projection development	18	+	Klk6
GO:0051971 GO:0050966	positive regulation of transmission of nerve impulse, detection of mechanical stimulus involved in sensory perception of pain	18	+	Itga2
GO:0007271	synaptic transmission, cholinergic	18	+	Chrm3
GO:0008088 GO:0002175	axon cargo transport, protein localization to paranode region of axon	19	+	Ugt8a
GO:0006836	neurotransmitter transport	19	+	Slc6a14
GO:0048170	positive regulation of long-term neuronal synaptic plasticity	19	+	Kit
GO:0048676	axon extension involved in development	22	+	Mtap1b
GO:2000734	negative regulation of glial cell-derived neurotrophic factor receptor signaling pathway involved in ureteric bud formation	22	+	Gata3
GO:0031175	neuron projection development	22	+	Btg2 Cd24a Ptk2b
GO:0010976	positive regulation of neuron projection development	22	+	Cd24a Lif Ptk2b
GO:0051930	regulation of sensory perception of pain	22	+	Edn1 F2r
GO:0048711	positive regulation of astrocyte differentiation	22	+	Lif Clcf1
GO:0048484	enteric nervous system development	2	-	Phactr4
GO:0001774	microglial cell activation	2	-	Jun
GO:0002282	microglial cell activation involved in immune response	2	-	Tlr2
GO:0021766	hippocampus development	2	-	Hdac1 Lrp8
GO:0050772	positive regulation of axonogenesis	4	-	Sema4d Shox2
GO:0048011	nerve growth factor receptor signaling pathway	9	-	Sort1
GO:0007638	mechanosensory behavior	9	-	Etv1
GO:0048678	response to axon injury	14	-	Erb2 Sod1
GO:0043525	positive regulation of neuron apoptotic process	16	-	Map3k11 Bcl2l11 Casp9 Ptpfr Cdc42
GO:0043526	neuroprotection	17	-	Ccl5
GO:0045664	regulation of neuron differentiation	17	-	Eya1

GO:0001580	detection of chemical stimulus involved in sensory perception of bitter taste	17	-	Rtp4
GO:0007413 GO:0030517	axonal fasciculation, negative regulation of axon extension, negative regulation	20	-	Nrp1
GO:0048843 GO:0048841	of axon extension involved in axon guidance, regulation of axon extension			
GO:0048485 GO:0021636	involved in axon guidance, sympathetic nervous system development, trigeminal nerve morphogenesis			
GO:0010977	negative regulation of neuron projection development	20	-	Lgals1
GO:0070997	neuron death	20	-	Plau
GO:0001956	positive regulation of neurotransmitter secretion	25	-	Sphk1

Table 3. Induction or repression of genes associated with neurobiological GO processes in the first passage (P1). qval \leq 0.05, N = 9, 16, 25, 36. P1 Ratio \geq 1.5-fold

Expt	UP	DN	UP.cnt	DN.cnt
BM9		Sema7a Eya1 Erbb2 Sod1 Hes1 Dll1 Slc5a3 Etv5 Vim	0	9
BM16	Ptgs2 Ptgs1 Fam134b Nr4a2 Hoxa1	Sema7a Eya1 Slit2	5	3
BM25	Nr4a2 Tubb2b Sfrp1 Tlr2 Ptgs2 Ptgs1 Klk8	Sema7a Slit2 Etv1 Sema5a Erbb2 Dll1 Bcl2 Egr1 Casp3 Itga2 Eya1	7	11
BM36	Nr4a2 Hoxa1 Pdzn3 Tlr2 Sfrp1 Ptgs1 Ndr1 Rac3 Palld Edn1 Ptgs2	Eya1 Hes1 Sema7a Bcl2 Slit2 Sema5a Itga2	11	7
BN9	Nr4a2 Dcl1 Tgfb2 Lif Itga1 Ugt8a Slit2 Clcf1 Lrrk2 Ptgs2	Sema7a Lgals1 Rtp4 Jak2 Jun Ntn1 Nrp1 Six1 Lgm1 Hdac1 Hipk2 Adam8	10	12
BN16	Ptgs2 Nr4a2 Dcl1 Tgfb2 Lif Vangl2 Cbl Celsr1 Fzd2 Dbn1 Vegfa Slc1a2 Chac1 Slit2 Sema3b Ugt8a Lrrk2 Kit Klk6 Agtbp1 Atxn2 Hoxa1 Aars Cln3 Rora Cd24a Scrib Cdk5 Eph4 Gli3 Etv1 Sema5a Flot1 Btg2 Mapk8 Ptk2b Wnt7b Areg Prmt1 L1cam Hmga2	Phactr4 Tlr2 Sema7a Ccl5 Eya1 Rtp4 Erbb2 Sod1 Sort1 Utp111 Ntn1 Nrp1 Sphk1	41	13
BN25	Slit2 Celsr1 Chrn1 Eph4 Etv1 Gli3 Sema5a Sema7a Ptgs2 Dst Ndel1 Agtbp1 Atxn2 Hoxa1 Vangl2 Fzd2 Pcsk6 Slc18a1 Myo7a Il23a Nr4a2 Dcl1 Lrrk2 Maoa Klk6 Itga2 Chrn3 Ugt8a Slc6a14 Kit Mtap1b Gata3 Btg2 Cd24a Ptk2b Lif Edn1 F2r Clcf1	Phactr4 Jun Tlr2 Hdac1 Lrp8 Sema4d Shox2 Sort1 Etv1 Erbb2 Sod1 Map3k11 Bcl2l1 Casp9 Ptpfr Cdc42 Ccl5 Eya1 Rtp4 Nrp1 Lgals1 Plau Sphk1	39	23
BN36	Dst Ndel1 Ccl2 Arhgef7 Hif1a Sema3c Vangl2 Chrn3 Celsr1 Syng1 Lmo4 Serpine2 Pcsk6 Slc18a1 Tcfap2a Cln3 Dbn1 Vegfa Slc1a2 Chac1 Jhdm1d Itga2 Myo7a Lif Eph4 Etv1 Sema5a Ugt8a Slc6a14 Kit Mtap1b Gata3 Cd24a Gdf11 Btg2 Ptk2b Tbc1d24 Chrn1 Il23a Clcf1 Rnd1 Klk6 Edn1 Ptgs2 Slit2 Dcl1 Nr4a2 Lrrk2 Maoa	Ccl5 Eya1 Rtp4 Ntn1 Sema7a Rb1 Shc1 Melk Shox2 Ndr1 Tlr2 Map3k11 Bcl2l1 Casp6 Casp9 Etv1 Jak2 Jun Nrp1 Lgals1 Plau Sphk1 Arrb1	49	23
LN9	Eya1 Nf1 Efna3 Cdon	Clcf1 Crf1 Slit2 Adm Sema5a Sema7a Hes1 Dll1 Notch1	4	9
LN16	Eya1 Efna3 Nr4a2 Ptgs2	Sema7a Clcf1 Crf1 Slit2 Etv1 Ablm1 Adm Itga2 Gnas Rtp4	4	10
LN25	Nr4a2 Hoxa1 Agrn Pdzn3 Gpr115 Lphn2 Gpr56 Trp53bp2 Arsb Arsa Chd7 Grhl3 Maoa Eya1 Efna3 Tlr2	Id4 Hes1 Gnas Egr1 Casp3 Plau Itga2 Slit2 Adm Etv1 Shox2 Palm Rtp4 Sema7a Cav2 Lynx1	16	16
LN36	Nr4a2 Tcfap2a Agrn Pdzn3 Tlr2 Ptgs2 Maoa Eya1 Efna3	Nrtn Efnb1 Hes1 Rarb Egl3 Etv1 Atp6v1b1 Casp3 Itga2 Cav2 Sema7a Shox2 Slit2 Adm Sema5a Sema3e Id4 Klk6 Gnas Rtp4	9	20

REFERENCES

1. Kim, S., Takahashi, H., Lin, W.W., Descargues, P., Grivennikov, S., Kim, Y., Luo, J.L., and Karin, M. 2009. Carcinoma-produced factors activate myeloid cells through TLR2 to stimulate metastasis. *Nature* 457:102-106.(PMID: 19122641)
2. Lin, Q., Lai, R., Chirieac, L.R., Li, C., Thomazy, V.A., Grammatikakis, I., Rassidakis, G.Z., Zhang, W., Fujio, Y., Kunisada, K., et al. 2005. Constitutive activation of JAK3/STAT3 in colon carcinoma tumors and cell lines: inhibition of JAK3/STAT3 signaling induces apoptosis and cell cycle arrest of colon carcinoma cells. *Am J Pathol* 167:969-980.(PMID: 16192633)
3. Uckun, F.M., Pitt, J., and Qazi, S. 2011. JAK3 pathway is constitutively active in B-lineage acute lymphoblastic leukemia. *Expert Rev Anticancer Ther* 11:37-48.(PMID: 21070101)
4. Garcia-Tunon, I., Ricote, M., Ruiz, A., Fraile, B., Paniagua, R., and Royuela, M. 2004. Interleukin-2 and its receptor complex (alpha, beta and gamma chains) in in situ and infiltrative human breast cancer: an immunohistochemical comparative study. *Breast Cancer Res* 6:R1-7.(PMID: 14680494)
5. Bolitho, C., Hahn, M.A., Baxter, R.C., and Marsh, D.J. 2010. The chemokine CXCL1 induces proliferation in epithelial ovarian cancer cells by transactivation of the epidermal growth factor receptor. *Endocr Relat Cancer* 17:929-940.(PMID: 20702723)
6. Junnila, S., Kokkola, A., Mizuguchi, T., Hirata, K., Karjalainen-Lindsberg, M.L., Puolakkainen, P., and Monni, O. 2011. Gene expression analysis identifies over-expression of CXCL1, SPARC, SPP1, and SULF1 in gastric cancer. *Genes Chromosomes Cancer* 49:28-39.(PMID: 19780053)
7. Cheng, W.L., Wang, C.S., Huang, Y.H., Tsai, M.M., Liang, Y., and Lin, K.H. 2011. Overexpression of CXCL1 and its receptor CXCR2 promote tumor invasion in gastric cancer. *Ann Oncol*.(PMID: 21343381)
8. Kawanishi, H., Matsui, Y., Ito, M., Watanabe, J., Takahashi, T., Nishizawa, K., Nishiyama, H., Kamoto, T., Mikami, Y., Tanaka, Y., et al. 2008. Secreted CXCL1 is a potential mediator and marker of the tumor invasion of bladder cancer. *Clin Cancer Res* 14:2579-2587.(PMID: 18451219)
9. Kobayashi, K., Sawada, K., Yamamoto, H., Wada, S., Saiga, H., and Nishida, H. 2003. Maternal macho-1 is an intrinsic factor that makes cell response to the same FGF signal differ between mesenchyme and notochord induction in ascidian embryos. *Development* 130:5179-5190.(PMID: 12954719)
10. Gualandris, A., Noghero, A., Geuna, M., Arese, M., Valdembrì, D., Serini, G., and Bussolino, F. 2009. Microenvironment drives the endothelial or neural fate of differentiating embryonic stem cells coexpressing neuropilin-1 and Flk-1. *Faseb J* 23:68-78.(PMID: 18757501)
11. Mintz, B., and Illmensee, K. 1975. Normal genetically mosaic mice produced from malignant teratocarcinoma cells. *Proc Natl Acad Sci U S A* 72:3585-3589.(PMID: 1059147)
12. Takahashi, M., Palmer, T.D., Takahashi, J., and Gage, F.H. 1998. Widespread integration and survival of adult-derived neural progenitor cells in the developing optic retina. *Mol Cell Neurosci* 12:340-348.(PMID: 9888988)
13. Bonfanti, P., Claudinot, S., Amici, A.W., Farley, A., Blackburn, C.C., and Barrandon, Y. 2010. Microenvironmental reprogramming of thymic epithelial cells to skin multipotent stem cells. *Nature* 466:978-982.(PMID: 20725041)
14. Gomi, M., Takagi, Y., Morizane, A., Doi, D., Nishimura, M., Miyamoto, S., and Takahashi, J. 2012. Functional recovery of the murine brain ischemia model using human induced pluripotent stem cell-derived telencephalic progenitors. *Brain Res* 1459:52-60.(PMID: 22572083)
15. Kogler, G., Sensken, S., Airey, J.A., Trapp, T., Muschen, M., Feldhahn, N., Liedtke, S., Sorg, R.V., Fischer, J., Rosenbaum, C., et al. 2004. A new human somatic stem cell from placental cord blood with intrinsic pluripotent differentiation potential. *J Exp Med* 200:123-135.(PMID: 15263023)
16. Tlsty, T.D., and Coussens, L.M. 2006. Tumor stroma and regulation of cancer development. *Annu Rev Pathol* 1:119-150.(PMID: 18039110)
17. Joyce, J.A., and Pollard, J.W. 2009. Microenvironmental regulation of metastasis. *Nat Rev Cancer* 9:239-252.(PMID: 19279573)

18. Frost, G.I., Lustgarten, J., Dudouet, B., Nyberg, L., Hartley-Asp, B., and Borgstrom, P. 2005. Novel syngeneic pseudo-orthotopic prostate cancer model: vascular, mitotic and apoptotic responses to castration. *Microvasc Res* 69:1-9.(PMID: 15797254)
19. Perez-Llamas, C., and Lopez-Bigas, N. 2011. Gitoools: analysis and visualisation of genomic data using interactive heat-maps. *PLoS One* 6:e19541.(PMID: 21602921)
20. Benjamini, Y., and Hochberg, Y. 1995. Controlling the false discovery rate: a practical and powerful approach to multiple testing. *Journal of the Royal Statistical Society Series B* 57:289-300.(PMID: 1121578)
21. Piekny, A., Werner, M., and Glotzer, M. 2005. Cytokinesis: welcome to the Rho zone. *Trends Cell Biol* 15:651-658.(PMID: 16243528)
22. Parsons, J.T., Horwitz, A.R., and Schwartz, M.A. 2010. Cell adhesion: integrating cytoskeletal dynamics and cellular tension. *Nat Rev Mol Cell Biol* 11:633-643.(PMID: 20729930)
23. Overgaard, K., Nielsen, O.B., Flatman, J.A., and Clausen, T. 1999. Relations between excitability and contractility in rat soleus muscle: role of the Na⁺-K⁺ pump and Na⁺/K⁺ gradients. *J Physiol* 518 (Pt 1):215-225.(PMID: 10373703)
24. Brochner, C.B., Johansen, J.S., Larsen, L.A., Bak, M., Mikkelsen, H.B., Byskov, A.G., Andersen, C.Y., and Mollgard, K. 2012. YKL-40 is differentially expressed in human embryonic stem cells and in cell progeny of the three germ layers. *J Histochem Cytochem* 60:188-204.(PMID: 22140133)
25. Yamamori, H., Hashimoto, R., Ohi, K., Yasuda, Y., Fukumoto, M., Kasahara, E., Sekiyama, A., Umeda-Yano, S., Okada, T., Iwase, M., et al. 2012. A promoter variant in the chitinase 3-like 1 gene is associated with serum YKL-40 level and personality trait. *Neurosci Lett* 513:204-208.(PMID: 22366530)
26. Kruse, A.C., Hu, J., Pan, A.C., Arlow, D.H., Rosenbaum, D.M., Rosemond, E., Green, H.F., Liu, T., Chae, P.S., Dror, R.O., et al. 2012. Structure and dynamics of the M3 muscarinic acetylcholine receptor. *Nature* 482:552-556.(PMID: 22358844)
27. Singh, A., Mishra, A.K., Ylaya, K., Hewitt, S.M., Sharma, K.C., and Saxena, S. 2012. Wilms tumor-1, claudin-1 and ezrin are useful immunohistochemical markers that help to distinguish schwannoma from fibroblastic meningioma. *Pathol Oncol Res* 18:383-389.(PMID: 21909685)
28. Molinari, F., Rio, M., Meskenaitė, V., Encha-Razavi, F., Auge, J., Bacq, D., Briault, S., Vekemans, M., Munnich, A., Attie-Bitach, T., et al. 2002. Truncating neurotropsin mutation in autosomal recessive nonsyndromic mental retardation. *Science* 298:1779-1781.(PMID: 12459588)
29. Hagglund, M.G., Sreedharan, S., Nilsson, V.C., Shaik, J.H., Almkvist, I.M., Backlin, S., Wrangé, O., and Fredriksson, R. 2011. Identification of SLC38A7 (SNAT7) protein as a glutamine transporter expressed in neurons. *J Biol Chem* 286:20500-20511.(PMID: 21511949)
30. Gros-Louis, F., Dupre, N., Dion, P., Fox, M.A., Laurent, S., Verreault, S., Sanes, J.R., Bouchard, J.P., and Rouleau, G.A. 2007. Mutations in SYNE1 lead to a newly discovered form of autosomal recessive cerebellar ataxia. *Nat Genet* 39:80-85.(PMID: 17159980)
31. Christophe-Hobertus, C., Szpirer, C., Guyon, R., and Christophe, D. 2001. Identification of the gene encoding Brain Cell Membrane Protein 1 (BCMP1), a putative four-transmembrane protein distantly related to the Peripheral Myelin Protein 22 / Epithelial Membrane Proteins and the Claudins. *BMC Genomics* 2:3.(PMID: 11472633)
32. Saadat, L., Dupree, J.L., Kilkus, J., Han, X., Traka, M., Proia, R.L., Dawson, G., and Popko, B. 2010. Absence of oligodendroglial glucosylceramide synthesis does not result in CNS myelin abnormalities or alter the dysmyelinating phenotype of CGT-deficient mice. *Glia* 58:391-398.(PMID: 19705459)
33. Lombard, Z., Park, C., Makova, K.D., and Ramsay, M. 2011. A computational approach to candidate gene prioritization for X-linked mental retardation using annotation-based binary filtering and motif-based linear discriminatory analysis. *Biol Direct* 6:30.(PMID: 21668950)
34. Metz, M., Gassmann, M., Fakler, B., Schaeren-Wiemers, N., and Bettler, B. 2011. Distribution of the auxiliary GABAB receptor subunits KCTD8, 12, 12b, and 16 in the mouse brain. *J Comp Neurol* 519:1435-1454.(PMID: 21452234)

35. Funayama, M., Hasegawa, K., Kowa, H., Saito, M., Tsuji, S., and Obata, F. 2002. A new locus for Parkinson's disease (PARK8) maps to chromosome 12p11.2-q13.1. *Ann Neurol* 51:296-301.(PMID: 11891824)
36. Cases, O., Seif, I., Grimsby, J., Gaspar, P., Chen, K., Pournin, S., Muller, U., Aguet, M., Babinet, C., Shih, J.C., et al. 1995. Aggressive behavior and altered amounts of brain serotonin and norepinephrine in mice lacking MAOA. *Science* 268:1763-1766.(PMID: 7792602)
37. Chambers, K.J., Tonkin, L.A., Chang, E., Shelton, D.N., Linskens, M.H., and Funk, W.D. 1998. Identification and cloning of a sequence homologue of dopamine beta-hydroxylase. *Gene* 218:111-120.(PMID: 9751809)
38. Le, W.D., Xu, P., Jankovic, J., Jiang, H., Appel, S.H., Smith, R.G., and Vassilatis, D.K. 2003. Mutations in NR4A2 associated with familial Parkinson disease. *Nat Genet* 33:85-89.(PMID: 12496759)
39. Straub, C., Zhang, W., and Howe, J.R. 2011. Neto2 modulation of kainate receptors with different subunit compositions. *J Neurosci* 31:8078-8082.(PMID: 21632929)
40. Buervenich, S., Carmine, A., Arvidsson, M., Xiang, F., Zhang, Z., Sydow, O., Jonsson, E.G., Sedvall, G.C., Leonard, S., Ross, R.G., et al. 2000. NURR1 mutations in cases of schizophrenia and manic-depressive disorder. *Am J Med Genet* 96:808-813.(PMID: 11121187)
41. Rojas, P., Joodmardi, E., Hong, Y., Perlmann, T., and Ogren, S.O. 2007. Adult mice with reduced Nurr1 expression: an animal model for schizophrenia. *Mol Psychiatry* 12:756-766.(PMID: 17457314)
42. Kim, S.Y., Yasuda, S., Tanaka, H., Yamagata, K., and Kim, H. 2011. Non-clustered protocadherin. *Cell Adh Migr* 5:97-105.(PMID: 21173574)
43. Ueda, Y., Yamaguchi, R., Ikawa, M., Okabe, M., Morii, E., Maeda, Y., and Kinoshita, T. 2007. PGAP1 knock-out mice show otocephaly and male infertility. *J Biol Chem* 282:30373-30380.(PMID: 17711852)
44. Horiuchi, Y., Iida, S., Koga, M., Ishiguro, H., Iijima, Y., Inada, T., Watanabe, Y., Someya, T., Ujike, H., Iwata, N., et al. 2012. Association of SNPs linked to increased expression of SLC1A1 with schizophrenia. *Am J Med Genet B Neuropsychiatr Genet* 159B:30-37.(PMID: 22095641)
45. Samuels, J., Wang, Y., Riddle, M.A., Greenberg, B.D., Fyer, A.J., McCracken, J.T., Rauch, S.L., Murphy, D.L., Grados, M.A., Knowles, J.A., et al. 2011. Comprehensive family-based association study of the glutamate transporter gene SLC1A1 in obsessive-compulsive disorder. *Am J Med Genet B Neuropsychiatr Genet* 156B:472-477.(PMID: 21445956)
46. Arnold, P.D., Sicard, T., Burroughs, E., Richter, M.A., and Kennedy, J.L. 2006. Glutamate transporter gene SLC1A1 associated with obsessive-compulsive disorder. *Arch Gen Psychiatry* 63:769-776.(PMID: 16818866)
47. Han, H.X., and Geng, J.G. 2011. Over-expression of Slit2 induces vessel formation and changes blood vessel permeability in mouse brain. *Acta Pharmacol Sin* 32:1327-1336.(PMID: 21986575)
48. Moreira, L.O., El Kasmi, K.C., Smith, A.M., Finkelstein, D., Fillon, S., Kim, Y.G., Nunez, G., Tuomanen, E., and Murray, P.J. 2008. The TLR2-MyD88-NOD2-RIPK2 signalling axis regulates a balanced pro-inflammatory and IL-10-mediated anti-inflammatory cytokine response to Gram-positive cell walls. *Cell Microbiol* 10:2067-2077.(PMID: 18549453)
49. Miles, R.R., Sluka, J.P., Halladay, D.L., Santerre, R.F., Hale, L.V., Bloem, L., Thirunavukkarasu, K., Galvin, R.J., Hock, J.M., and Onyia, J.E. 2000. ADAMTS-1: A cellular disintegrin and metalloprotease with thrombospondin motifs is a target for parathyroid hormone in bone. *Endocrinology* 141:4533-4542.(PMID: 11108265)
50. Lu, X., and Kang, Y. 2009. Metalloproteinases and osteoblast EGFR signaling in osteolytic bone metastasis of breast cancer. *Cell Cycle* 8:3804-3805.(PMID: 19934661)
51. Sabrautski, S., Rubio-Aliaga, I., Hans, W., Fuchs, H., Rathkolb, B., Calzada-Wack, J., Cohrs, C.M., Klaften, M., Seedorf, H., Eck, S., et al. 2012. New mouse models for metabolic bone diseases generated by genome-wide ENU mutagenesis. *Mamm Genome* 23:416-430.(PMID: 22527485)
52. Khoo, M.L., Tao, H., Meedeniya, A.C., Mackay-Sim, A., and Ma, D.D. 2011. Transplantation of neuronal-primed human bone marrow mesenchymal stem cells in hemiparkinsonian rodents. *PLoS One* 6:e19025.(PMID: 21625433)

53. Velasco, J., Zarrabeitia, M.T., Prieto, J.R., Perez-Castrillon, J.L., Perez-Aguilar, M.D., Perez-Nunez, M.I., Sanudo, C., Hernandez-Elena, J., Calvo, I., Ortiz, F., et al. 2011. Wnt pathway genes in osteoporosis and osteoarthritis: differential expression and genetic association study. *Osteoporos Int* 21:109-118.(PMID: 19373426)
54. Johnston, J., Ramos-Valdes, Y., Stanton, L.A., Ladhani, S., Beier, F., and Dimattia, G.E. 2010. Human stanniocalcin-1 or -2 expressed in mice reduces bone size and severely inhibits cranial intramembranous bone growth. *Transgenic Res* 19:1017-1039.(PMID: 20174869)
55. McCullough, K.D., Martindale, J.L., Klotz, L.O., Aw, T.Y., and Holbrook, N.J. 2001. Gadd153 sensitizes cells to endoplasmic reticulum stress by down-regulating Bcl2 and perturbing the cellular redox state. *Mol Cell Biol* 21:1249-1259.(PMID: 11158311)
56. Tsujimoto, Y., Finger, L.R., Yunis, J., Nowell, P.C., and Croce, C.M. 1984. Cloning of the chromosome breakpoint of neoplastic B cells with the t(14;18) chromosome translocation. *Science* 226:1097-1099.(PMID: 6093263)
57. Cory, S., and Adams, J.M. 2002. The Bcl2 family: regulators of the cellular life-or-death switch. *Nat Rev Cancer* 2:647-656.(PMID: 12209154)
58. Zhang, P., Hu, X., Xu, X., Chen, Y., and Bache, R.J. 2011. Dimethylarginine dimethylaminohydrolase 1 modulates endothelial cell growth through nitric oxide and Akt. *Arterioscler Thromb Vasc Biol* 31:890-897.(PMID: 21212404)
59. Eilken, H.M., and Adams, R.H. 2010. Dynamics of endothelial cell behavior in sprouting angiogenesis. *Curr Opin Cell Biol* 22:617-625.(PMID: 20817428)

Supplemental Material

for

Cancer adaptomes: gene expression requirements for cancer cell growth in foreign tissue microenvironments

Gaelle Rondeau¹

Parisa Abedinpour¹

Prerak Desai¹

Veronique Baron^{1,2}

Per Borgstrom^{1,2,4}

John Welsh^{1,3,4}

¹Vaccine Research Institute of San Diego

²Pelficure, Inc.

³San Diego Institute of Biological Research

Table S1

Kmeans group	GO ID	GO Biological Process Term	qval*	Genes annotated with GO term
Brain*				
BN₂₅ 2	GO:0032321	<i>positive regulation of Rho GTPase activity</i>	0.001	Cdc42ep2, Jun, Grhl3
	GO:0030036	<i>actin cytoskeletal organization</i>	0.003	Coro6, Pdgfb, Cdc42ep2, Phactr4, Fscn1
	GO:0032956	<i>regulation of actin cytoskeleton organization</i>	0.016	Grhl3, Palld
	GO:0051017	<i>actin filament bundle assembly</i>	0.019	Actn1, Fscn1
BN₂₅ 4	GO:0007049	<i>cell cycle</i>	7×10^{-11}	Terf1, Sgol2, Aspm, Nuf2, Fbxo5, E2f7, Aurkb, Cdc6, E2f6, Vrk1, Ncapg2, C79407, Cinp, Cks2, Dlgap5, F630043A04Rik, Esco2, Cdca2, Racgap1, Cdc45, Mapre2, Cdca5, Kif20b, Kif11, Cep55, Incenp, Anxa1, Fam83d, Spc25, Bub1, Smc4, Psr1, Sass6, Ect2, Ccna2, Ccne2, Casp8ap2, Smc2, Nasp, Kif2c, Nudc, Kntc1, Stard13, Mad2l1, Cdca3, Ncapd2, Fanci, E2f8, Spc24, Ccnb2, Cctn2
	GO:0051301	<i>cell division</i>	4×10^{-7}	Terf1, Sgol2, Aspm, Nuf2, Fbxo5, Aurkb, Cdc6, Vrk1, Ncapg2, C79407, Cinp, Cks2, F630043A04Rik, Cdca2, Racgap1, Cdc45, Mapre2, Cdca5, Kif20b, Kif11, Cep55, Incenp, Fam83d, Spc25, Bub1, Smc4, Psr1, Ect2, Ccna2, Ccne2, Smc2, Kif2c, Nudc, Kntc1, Mad2l1, Cdca3, Ncapd2, Spc24, Ccnb2, Cctn2
	GO:0007067	<i>mitosis</i>	2×10^{-6}	Terf1, Aspm, Nuf2, Fbxo5, Aurkb, Cdc6, Vrk1, Ncapg2, C79407, F630043A04Rik, Cdca2, Mapre2, Cdca5, Kif20b, Kif11, Cep55, Incenp, Fam83d, Spc25, Bub1, Smc4, Psr1, Ccna2, Smc2, Kif2c, Nudc, Kntc1, Mad2l1, Cdca3, Ncapd2, Spc24, Ccnb2, Cctn2
	GO:0006260	<i>DNA replication</i>	8×10^{-6}	Dna2, Prim1, Cdc6, Pold2, Tk1, Rrm2, Pole2, Cinp, Cdc45, Pola2, Fen1, Mcm10, Orc1, Orc3, Nasp, Rfc5, Rpa3
	GO:0007076	<i>mitotic chromosome condensation</i>	4×10^{-7}	Cdca5, Smc4, Smc2, Ncapg, Ncapd2
	GO:0006281	<i>DNA repair</i>	2×10^{-4}	Exo1, Brip1, Tdp1, Gen1, Cinp, Parp2, Esco2, Fen1, Smc4, Rad54b, Smc2, Usp1, Rad54l, Gtf2h3, Rpa3, Mbd4, Fanci, Neil3, Fancb, Cctn2
	GO:0030261	<i>chromosome condensation</i>	4.14×10^{-4}	Top2a, Ncapg2, Smc4, Smc2, Ncapd2
	GO:0007059	<i>chromosome segregation</i>	9.66×10^{-4}	Sgol2, Top2a, F630043A04Rik, Incenp, Spc25, Bub1, Ebna1bp2, Cdk5rap2, Kif2c
	GO:0006334	<i>nucleosome assembly</i>	0.001	Hist1h2bb, Hist1h1b, Hist1h2bh, Hist2h2ab, Hist2h2ac, Cenpa, Asf1b
	GO:0006487	<i>protein N-linked glycosylation</i>	0.002	Entpd5, Alg6, Pomgnt1, Ddost
	GO:0006284	<i>base-excision repair</i>	0.006	Dna2, Parp2, Mbd4, Neil3
	GO:0007099	<i>centriole replication</i>	0.009	Plk4, Sass6, Cctn2
BN₂₅ 6	GO:0006814	<i>sodium ion transport</i>	0.0006	Atp1b1, Slc38a1, Slc5a3, Slc34a2
	GO:0015807	<i>L-amino acid transport</i>	0.0008	Slc38a1, Slc1a1, Slc7a5
	GO:0006811	<i>ion transport</i>	0.0009	Atp1b1, Tcn2, Chrn1, Slc38a1, Slc5a3, Lrrc26, Slc34a2, Atp6v0e2
	GO:0003333	<i>amino acid transmembrane transport</i>	0.006	Slc38a1, Slc1a1, Slc7a5
BN₂₅ 15	GO:0006811	<i>ion transport</i>	0.008	Slc5a8, G630090E17Rik, Cacnb3, Slc39a4, Atp6v1f, Atp6v0a4, Atp6v1b2, Slc38a7
	GO:0006820	<i>anion transport</i>	0.03	Slc1a4, Slc1a2
	GO:0015991	<i>ATP hydrolysis coupled proton transport</i>	0.004	Atp6v1f, Atp6v0a4, Atp6v1b2
	GO:0001569	<i>patterning of blood vessels</i>	0.004	Plxnd1, Vangl2, Vegfa
	GO:0001944	<i>vascular development</i>	0.004	Fzd5, Fzd2, Vegfa
	GO:0034976	<i>response to endoplasmic</i>	0.001	Fam129a, Ddit3, Scamp5

		<i>reticulum stress</i>		
	GO:0030968	<i>endoplasmic reticulum unfolded protein response</i>	0.006	Ddit3, Ppp1r15a, Herpud1
BN₂₅ 18	GO:0055072	<i>iron ion homeostasis</i>	0.0009	Steap2, Steap1, Hmox1
	GO:0015809	<i>arginine transport</i>	0.042	Slc7a2
BN₂₅ 19	GO:0015837	<i>amine transport</i>	0.018	Slc6a14
	GO:0008228	<i>opsonization</i>	0.0003	Sftpd, Lbp
	GO:0006935	<i>chemotaxis</i>	0.0004	S100a8, Kit, Cxcl5
	GO:0043032	<i>positive regulation of macrophage activation</i>	0.0007	Il33, Lbp
	GO:00507866	<i>positive regulation of phagocytosis</i>	0.002	Sftpd, Sirpa
BN₂₅ 20	GO:0001525	<i>angiogenesis</i>	0.003	Plau, Col8a1, Nrp1
BN₂₅ 25	GO:0015833	<i>peptide transport</i>	0.008	Tap1, Tap2
	GO:0006508	<i>proteolysis</i>	0.01	Lgmn, Adamts1, Adamts5, Psmb9, Eml3, Ctsw, Ermp1, Ctso, Ece1
	GO:0045087	<i>innate immune response</i>	0.02	Jak2, Ifih1, Zbp1, Sp110
Bone				
BM₂₅ 4	GO:0045670	<i>regulation of osteoclast differentiation</i>	0.0006	5730469M10Rik, Adam8
BM₂₅ 19	GO:0030500	<i>regulation of bone mineralization</i>	0.0004	Ank, Ecm1, Mgp
	GO:0001525	<i>angiogenesis</i>	0.0006	Elk3, Plau, Hbegf, Ccbe1, Ecm1, Eph2
Lung				
LN₂₅ 19	GO:0060484	<i>lung-associated mesenchyme development</i>	0.001	Ptk7, Hoxa5, Fgfr1

Table S2: Genes induced in different passages in brain tissue				
Timing				
highest in P1	≥4-fold up-regulated			Akr1b3, Ccl9, Crct1, Gm6644, Jam2, Kctd12b, Klk6, Klk9, Lrrk2, Maoa, Mcpt8, Moxd1, Neto2, Nr4a2, Nt5dc2, Pcdh7, Pgap1, Pilrb2, Rnasel, Slc1a1, Slc7a2, Slit2, Sparc, Steap1
highest in P1 and P2	≥4-fold up-regulated, approximately equal in P1 and P2			Atp1b1, Car6, Chi3l1, Chrm3, Cldn1, Cxcl5, Fam73a, Gpx2, Hlf, Il1f6, Isyna1, Itga1, Kit, Lass6, Ltf, Man1c1, Pilrb1, Prss12, S100a8, Sftpd, Sirpa, Slc38a1, Slc6a14, Syne1, Tmem47, Tnfrsf21, Ugt8a, Zc4h2.
highest in P2	≥4-fold up-regulated	None of these is similarly regulated in the bone marrow or lung.		Akap12, Aldh1l2, Armcx2, Chac1, Chrm3, Csn3, Ctxn1, Cxx1a, Dbn1, Ddit3, Dip2c, Ehf, Fam129a, Fndc1, Gadd45a, Gdpd1, Gjb3, Gm129, Gpt2, Gpx2, Gvin1, Il33, Klhl38, Klk14, Lbp, Milana, Mthfd2, Phyhd1, Pigr, Plekhhb1, Reep6, Renbp, Tc2n, Tmem150a, Trib3, Wif1.
highest in P3	≥4-fold up-regulated			2310002L13Rik, Aicda, Akr1b8, Anxa8, Gsta1, Has2, Lce1h, Lce1i, Ly6c1, , Ly6d, Rbp7, Serpine1
highest in P3 and P4	≥4-fold up-regulated, approximately equal in P3 and P4			Lce1g, Ly6a, Ly6c2
highest in P4	≥4-fold up-regulated			Aicda, Car9, Ddr2, Il2rg, Ly6a, Ly6c2, Olfml3, Orm1
high in P4 in all tissues	≥2-fold up-regulated			2310002L13Rik, Aicda, Akr1b8, Anxa8, Arhgdib, Cbr2, Cxcl5, Gsta1, Has2, Il1f6, Il2rg, Lass3, Ly6a, Ly6c1, Ly6c2, Ly6d, Mela, Olfml3, Pcolce, Pcolce2, Pbbp, Prnd, Rbp7, Reep6, Rnd1, S100a8, Samd12, Serpine1, Tnlp3, U90926
	~4-fold down-regulated in P4			1300014I06Rik, 1500015010Rik, Adamts9, Atp10b, BC005685, Ccdc141, Clca5, Cldn2, Cpm, Eph4, Eya1, Eya2, Gadpr, Gstm1, Hey1, Lrt23, Lect1, Ms4a6d, Ppargc1a, Sd[r, Sema7a, Slc38a1, Slco1a5, St8sia1, Trpm3
higher than control in all tissues in at least one passage	≥2-fold up-regulated in all tissues in at least one passage			2310002L13Rik, 9930023K05Rik, Adam8, Afap1l1, Aicda, Akr1b8, Alpl, Anxa8, Apobec1, Arhgdib, Ass1, Atp10d, Atp6v0a4, C630004H02Rik, Car9, Cbr2, Cdc42ep2, Cdhr1, Cldn1, Csf3, Cxcl1, Cxcl5, Dse, Edn1, Fosl1, Fxyd5, Gatsl3, Gm10639, Gsta1, Gsta2, Has2, Il1f6, Il2rg, Itgb6, Lass3, Lipg, Ltf, Ly6a, Ly6c1, Ly6c2, Ly6d, Ly96, Lypd3, Mela, Muc20, Ndrgr1, Olfml3, Pak3, Palld, Pcolce, Pcolce2, Pdgfb, Pilrb2, Plscr2, Pbbp, Prkch, Prnd, Ptgs2, Rbp7, Reep6, Rgs16, Rnasel, Rnd1, S100a14, S100a8, Samd12, Serpine1, Sh3bp1, Slco2a1, Stc2, Tigit, Timp1, Tlr2, Tnlp3, Tspan1, U90926
lower than control in P4 in all tissues	≥2-fold down-regulated in all tissues in P4			1500015O10Rik, Ak3, Atp10b, Atp6v1b1, BC005685, Ccl5, Cldn2, Eph4, Eya1, Gabpr, Gstm1, Gzme, Hey1, Lect1, Maoa, Mcpt8, Ms4a6d, Plekhhb1, Ppargc1a, Sdpr, Sema7a, Slco1a5, Slit2, Trpm3, Zc4h2.
down-regulated in all tissues	≥2-fold down-regulated in all tissues in any passage			1500015O10Rik, Adamts9, Ak3, Aldh3a1, Anxa9, Atp10b, Atp6v1b1, AW112010, BC005685, Cadm1, Car2, Ccl5, Ceacam1, Clca5, Cldn2, D10Bwg1379e, Dll1, Dusp6,

in at least one passage				Efna3, Eph4, Etv1, Eya1, Eya2, Fn1, Foxi1, Gabrp, Galnt7, Gm14005, Grb14, Gstm1, Gtpbp10, Gzme, Hey1, Hsd11b1, Ifi44, Kcnn4, Krt23, Lama4, Lbh, Lect1, Maoa, Mcpt8, Mlst8, Ms4a6d, Papln, Pgf, Pilra, Pla2g16, Plekhhb1, Ppargc1a, Ramp1, Rny1, S100a4, Saa3, Sdpr, Sema5a, Sema7a, Sftpd, Slc1a1, Slco1a5, Slit2, Snora44, St8sia1, St8sia6, Tgfbr3, Timp3, Trpm3, Tspan13, Txnip, Unc80, Zc4h2
	strongly up-regulated (≥4-fold) in all three tissues by P4			Aicda, Akr1b8, Anxa8, Has2, Il2rg, Ly6a, Ly6d, Orm1, Serpine1 and Rpb7

Supplemental Material Table 1: Summary of GO Biological Process terms discussed in the text.

*See **Supplemental Material: Analysis of BN₉ groups 1-9, below.**

Color coding: **Neurobiological**, **Cell cycle**, **adhesion**, and **motility**, **Homeostasis**, **Bone marrow**, **Angiogenesis**, **Protein synthesis**, **Stress**, **Various**.

Table S3 Gene-Drug pairs		
Gene	Drug	Ref
Alpl	levamisole	(1)
Arg2	difluoromethylornithine	(2)
Bcl2	AT-101 , ABT-263, oblimersen and others	(3-5)
C3	peptide inhibitors	(6)
Chrm3	cevimeline, others,	(7-10)
Kit	imatinib, others	(11-14)
Maoa	tranylcypromine, others	(15-17)
Odc1	difluoromethylornithine	(18))
Plat	6-aminohexanoic acid	(19)
Pnp	BCX-34, others	(20-22)
Hdac1	MI-129, others	(23-25)
Jun	T5224	(26)
Vdr	Paricalcitol, others	(27-29)

Materials and Methods

Platinum chambers were fitted in the dorsal skinfold of male nude mice by surgery as described extensively in (30-32). Brain and lung tissue were obtained from donor mice, minced with a razor blade and introduced into the chamber. These tissues were allowed to revascularize for 7-10 days, whereupon spheroids prepared from the HER2-positive mouse breast cancer cell line N202 (9) were implanted on top of the bone marrow, lung tissue, or brain tissue. These N202 cells expressed GFP from a stably integrated H2B-GFP construct. Growth of the N202 cells was followed via the GFP using fluorescence microscopy through the window of the dorsal skin fold chamber. After 21 days, the developing tumors were removed from the chambers and placed back into cell culture for 2-4 weeks, whereupon new spheroids were again prepared and a new cycle of implantation into freshly prepared dorsal skin fold chambers was initiated. This was repeated for a total of 4 cycles.

At each cycle, RNA was harvested from the same cell cultures that were used to form the spheroids for gene expression analysis on Affymetrix GeneChip™ mouse gene 1.0 St array, following the manufacturer's protocol for target preparation, hybridization, washing and scanning. Briefly, the cells were grown to 60-70% confluency. Total RNA was extracted using an RNeasy Mini Kit (Qiagen, Valencia, CA) following the manufacturer's instructions. RNA concentration was determined spectroscopically, and integrity was assessed qualitatively by agarose gel electrophoresis. 100ng of total RNA was used for target preparation.

The parental cell line served as a common control. Technical replicates starting with cells in culture for the common control (P0) and for the cells harvested at the four time points (P1-4) for cells adapted to brain tissue were performed. Cells harvested from bone marrow and lung tissue were analyzed once per time point. Gene expression data were processed using RMA (Robust Multiarray Average) (33) from within Affymetrix Expression Console Software (**Figure 1S**). Data were analyzed using routines written in R (34).

Genes were filtered for those having signal intensities exceeding 95% of the signals from negative hybridization controls, which yielded 10,522 positive probe sets (**Figure S2**).

Ratios were obtained by dividing the signal log ratios of intensities obtained for each gene after each of

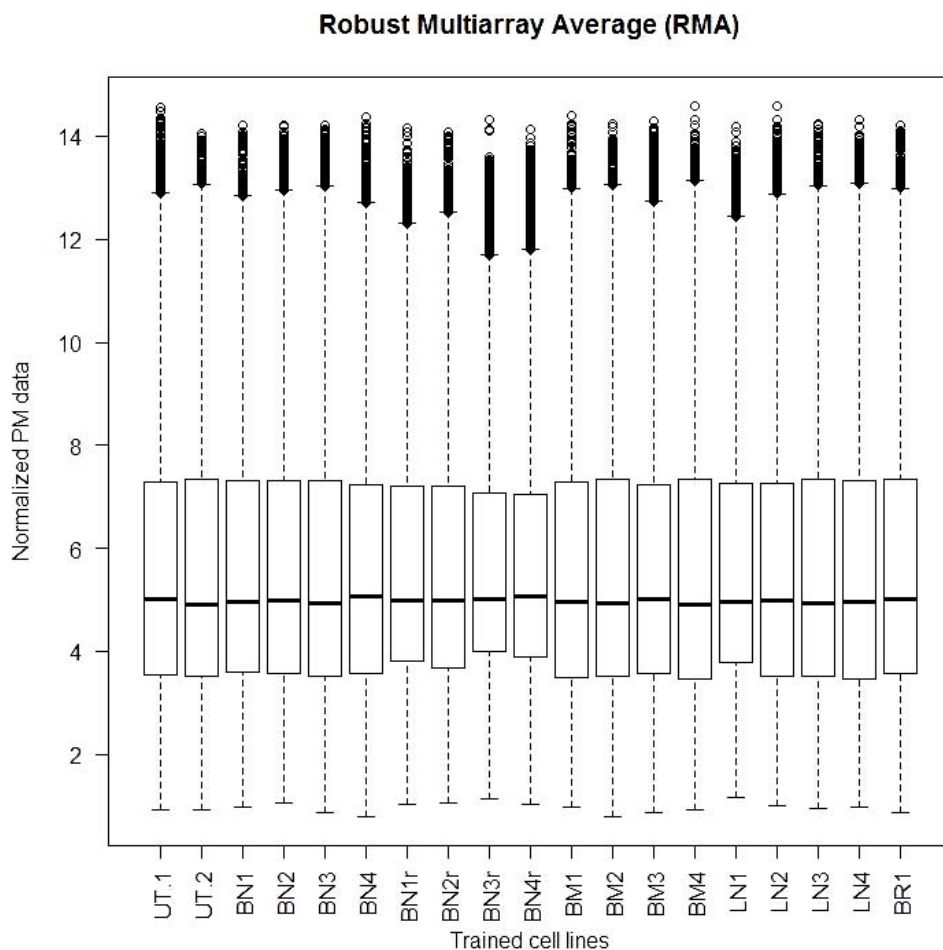


Figure S1. The robust multiarray average implemented in Affymetrix Expression Array Console Software. UT = Untrained, BN=brain, BNr=brain technical repeat, BM=bone marrow, LN=lung, BR=breast.

the four serial passages described above, creating a 5 element vector for each gene of the form $(0, x_1, x_2, x_3, x_4)$ where x_n are the ratios for each passage, and these vectors were sorted into kmeans groups. When using kmeans, a decision must be made regarding the number of groups, N , and there is no rigorously correct way to do this. One approach is to set a maximum acceptable fitting error (i.e. the 'sum of squares within'), another is to track the error assuming different numbers of groups and to choose a number of groups beyond which the error no longer decreases rapidly (i.e. identify an "elbow"), and a third is to try different numbers of groups and test them post hoc for statistically significant biological correlations. We find statistically significant correlations with GO biological process terms using different assumptions for N . P-values were determined by Fisher's exact test and corrected to yield the false discovery rate (FDR) according to Benjamini and Hochberg(35).

This was done assuming $N=9, 16, 25, 36, 49$, and 64 , where N corresponds to the number of kmeans groups. Duplicate microarrays were performed for the parental (unadapted) cell line (**Figure S3**) and for each time point of the brain experiment (**Figure S4**), and duplicate signal measurements were averaged after RMA. For the bone marrow and lung experiments, a single microarray experiment was done for each time point.

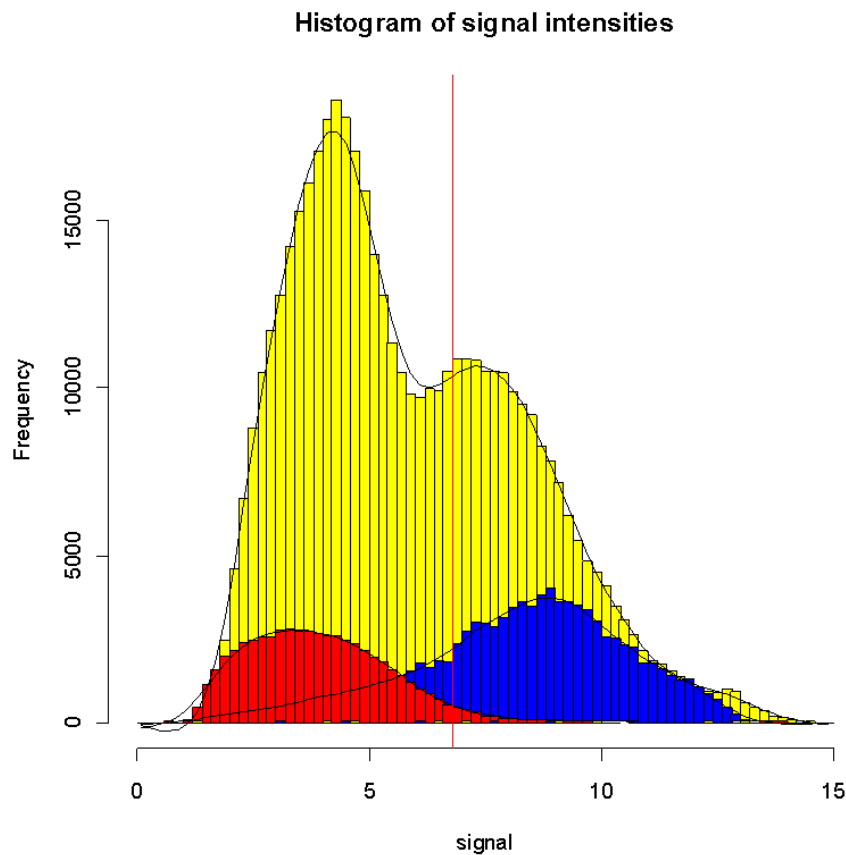


Figure S2. Histogram of PM signals on Affymetrix arrays. Yellow=all PM scores, Red=negative hybridization controls, Blue=positive hybridization "spike-in" controls provided by the manufacturer. The vertical red line is placed at the position above 95% of the negative controls. Genes were included for which the signal exceeded this threshold for at least one trained or untrained cell line.

Each gene was matched to GO Biological Process Terms. Annotations were the union of the original Affymetrix GeneChip™ mouse gene1.0 St array provided by the Affymetrix Expression Console software and annotations from Mouse Genome Informatics (<http://www.informatics.jax.org>). For each value of N , the frequency of each GO Biological Process Term within N kmeans groups was calculated. Values for the expected frequencies were calculated based on the number of genes in each group. For each GO term and for each group, a 2x2 contingency table was generated containing the expected and observed frequencies, compared with the frequency of the term and the total number of genes. Fisher's exact test was performed on each contingency table to give a list of terms and p-values associated with kmeans group. This is a multiple

testing situation, so false discovery rates (qval) were calculated by sorting p-values from largest to smallest and dividing by their rank, according to Benjamini and Hochberg(35). These lists were then sorted by qval from smallest to largest and stored in a MySQL database. A web interface was built to access this database. Genes and GO terms are cross-referenced by links to NCBI/Gene and AmiGO (<http://amigo.geneontology.org>), re

We used Therapeutic Targets Database drug-gene database (<http://bidd.nus.edu.sg/group/ttd/>) and biobnet (<http://biobnet.abcc.ncifcrf.gov/>) for conversions, the latter was necessary to recover official gene

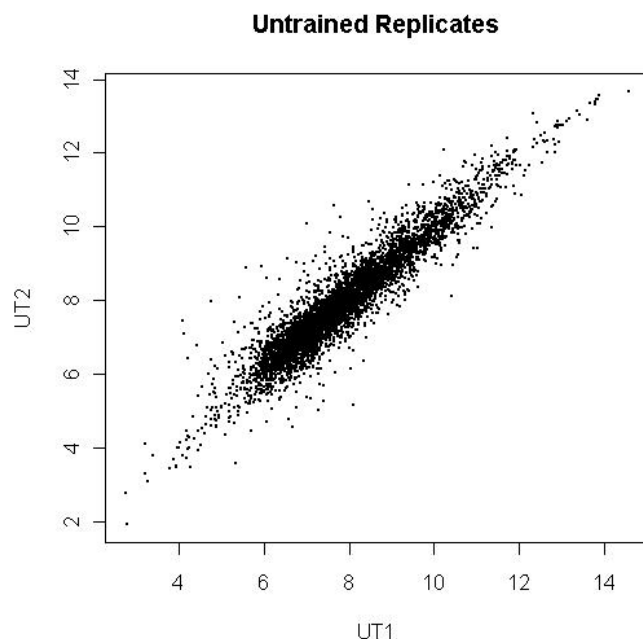


Figure S3. Scatterplot of RMA-normalized untrained control replicates. UT1 and UT2 microarrays were repeated beginning with two independent cell cultures and corresponding RNA preparations.

symbols for cross-species comparison. It should be kept in mind that identical or similar drug effects across species cannot be assured.

Each passage of N2O2 for the three tissues were seeded at 30000 cells in triplicate and counted every three days during two weeks. Two independent measurements of each cell culture were done and a third one was done if discrepancies were seen between these measurements. The mean was calculated for each time, using these 6 + values.

Table 2 was generated by identifying GO Biological Process Terms that pertained to brain by partial matches between the GO term and the words or partial words “axon”, “neuro”, “neural”, “brain”, “neocortex”, “nerve”, “glial”, “hippocampal”, “hippocampus”, “cerebellar”, “cerebral”, “dopa”, “synaptic”, “sensory”, “astrocyte”, “olfactory”, and “memory”.

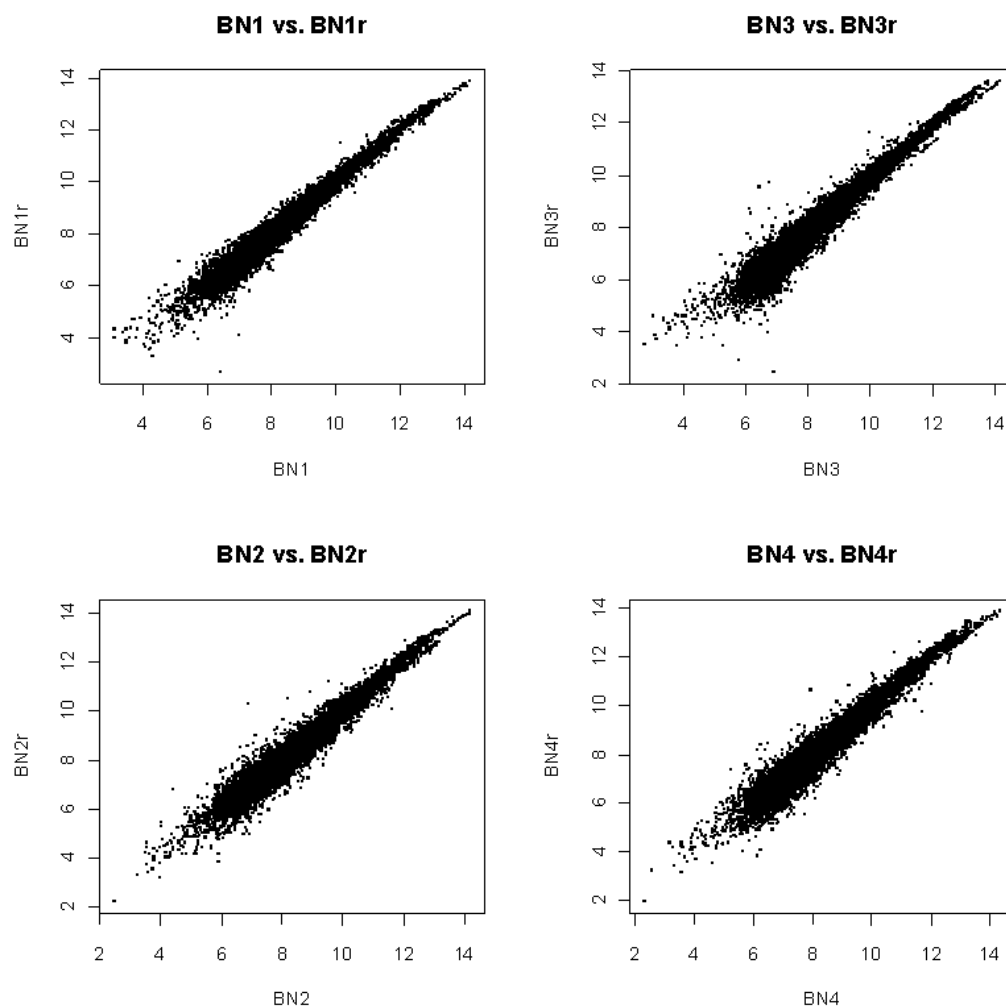


Figure S4. Technical replicates of microarrays for cells trained to grow on brain tissue, beginning with independent cell cultures and corresponding RNA preparations.

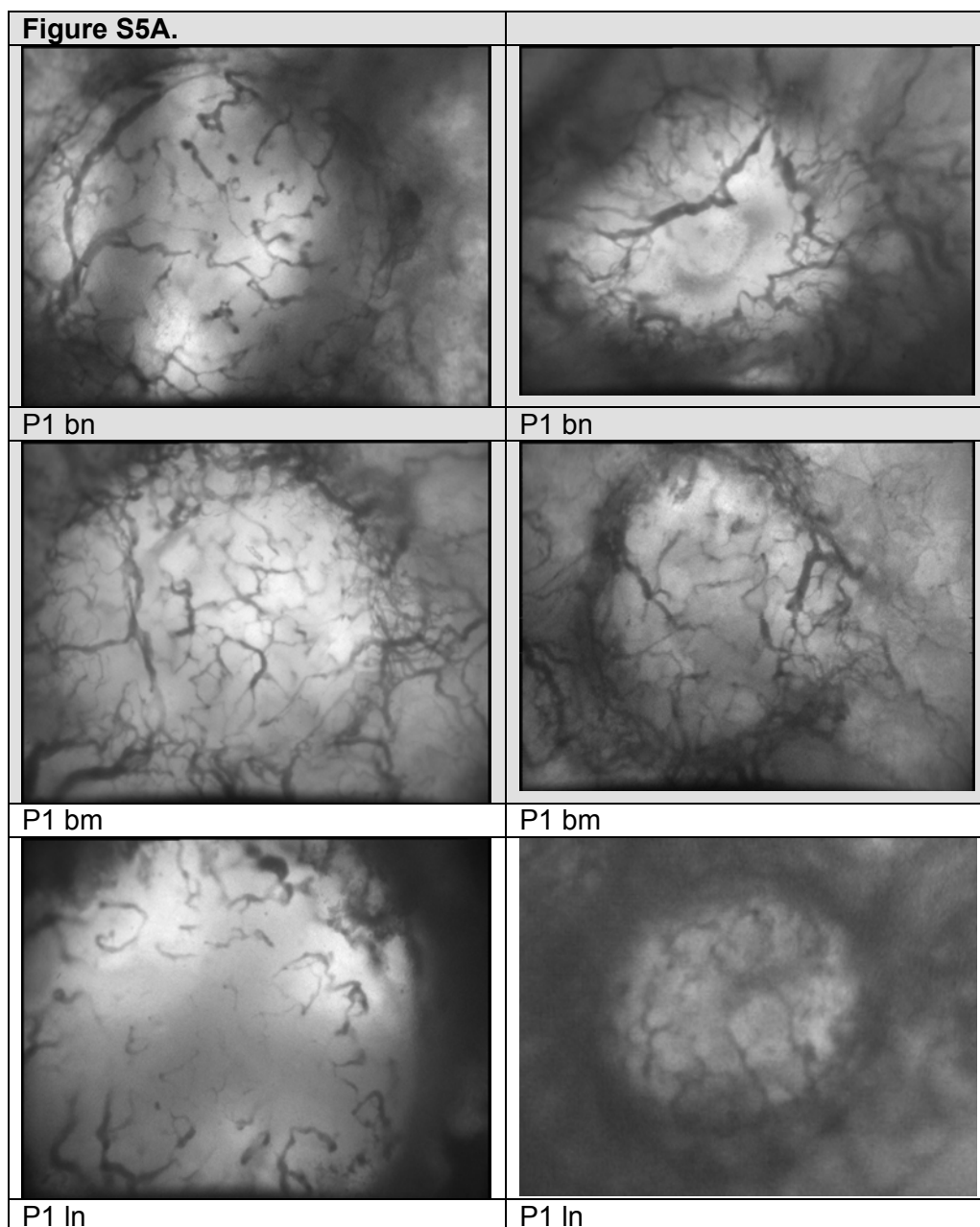


Figure S5A. Bright field images showing that neovascularization of the developing tumor (evident as a raised, bright nodule) becomes robustly in the first passage (P1) in all three tissues, brain (bn), bone marrow (bm), and lung (ln).

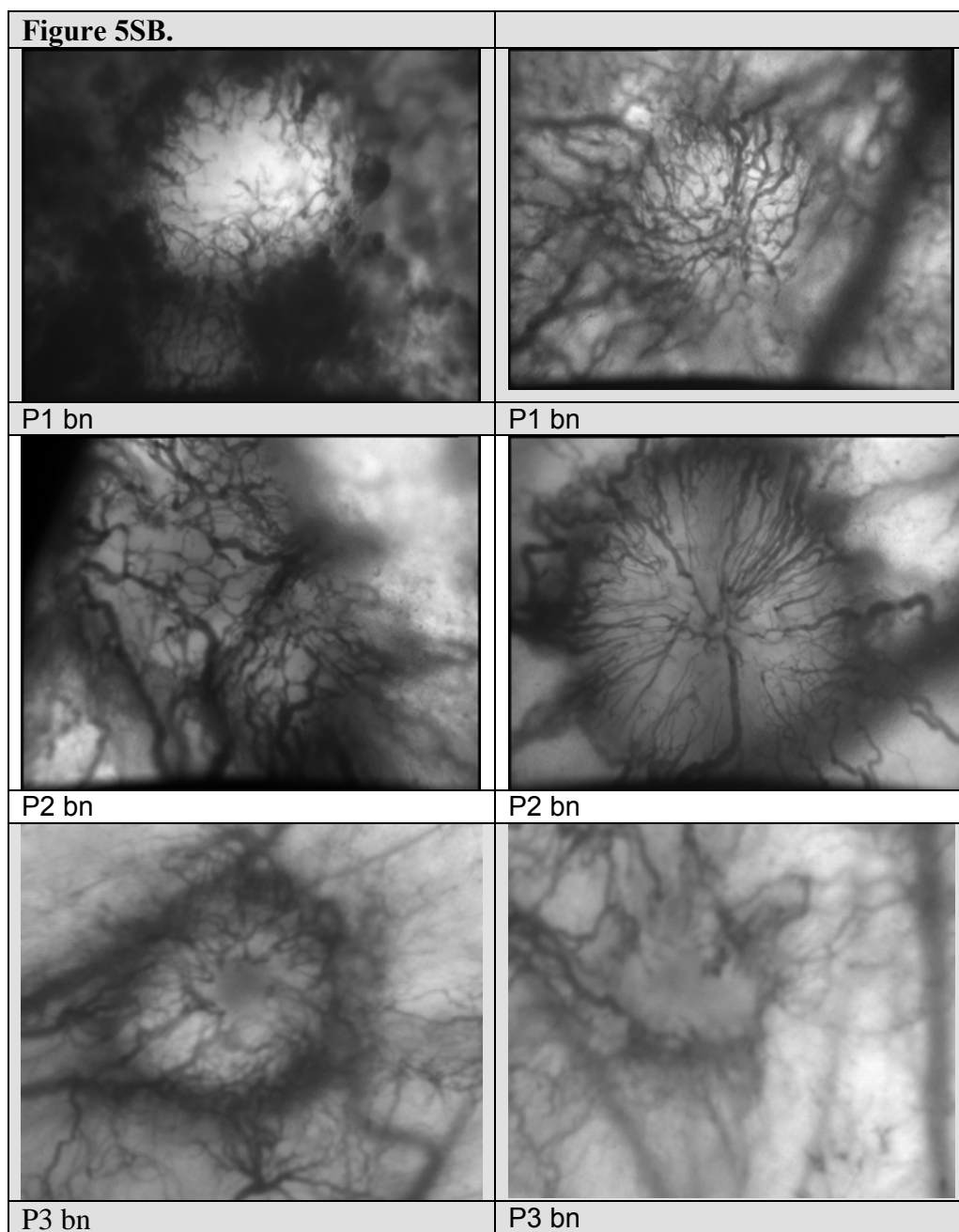
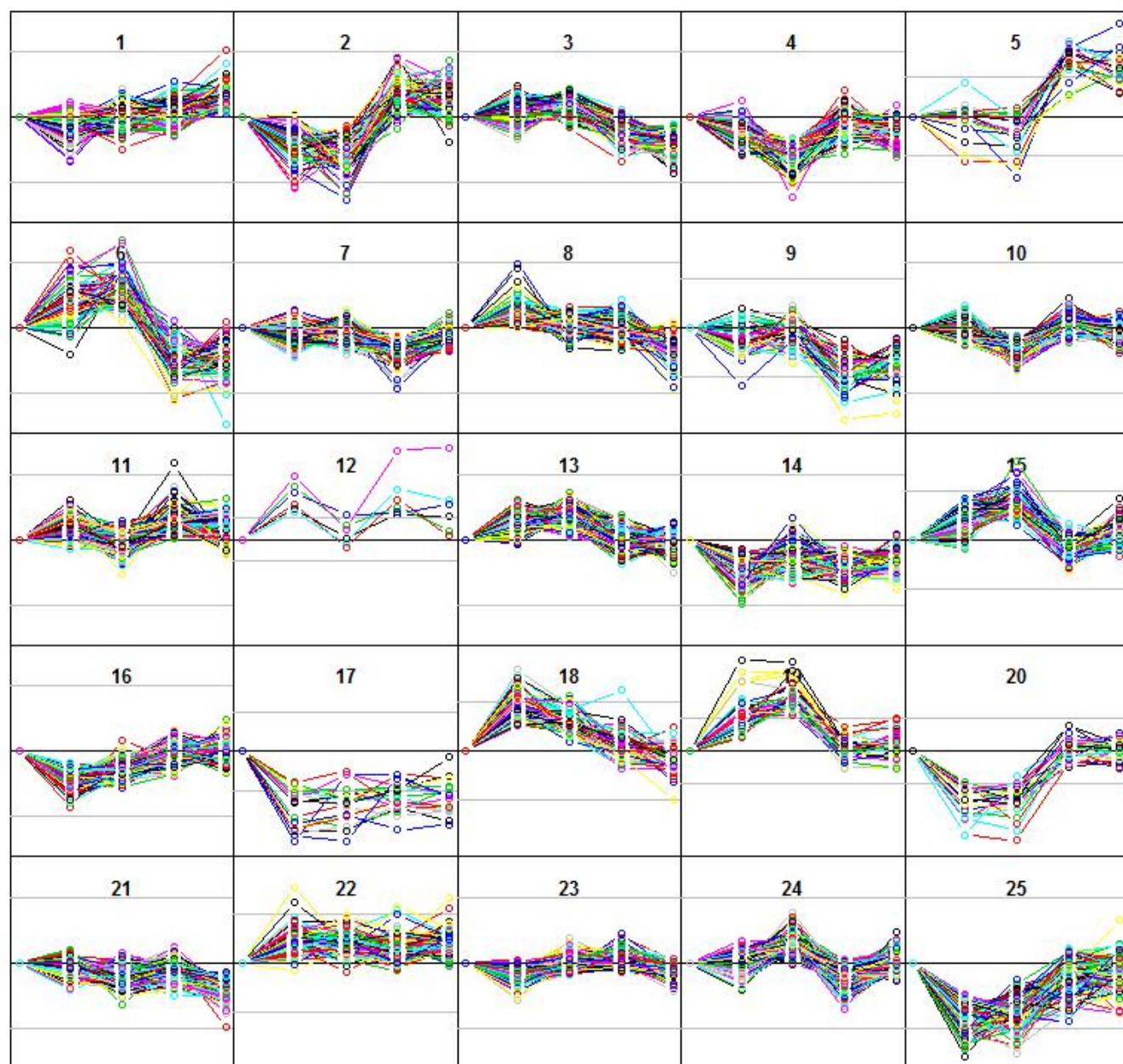


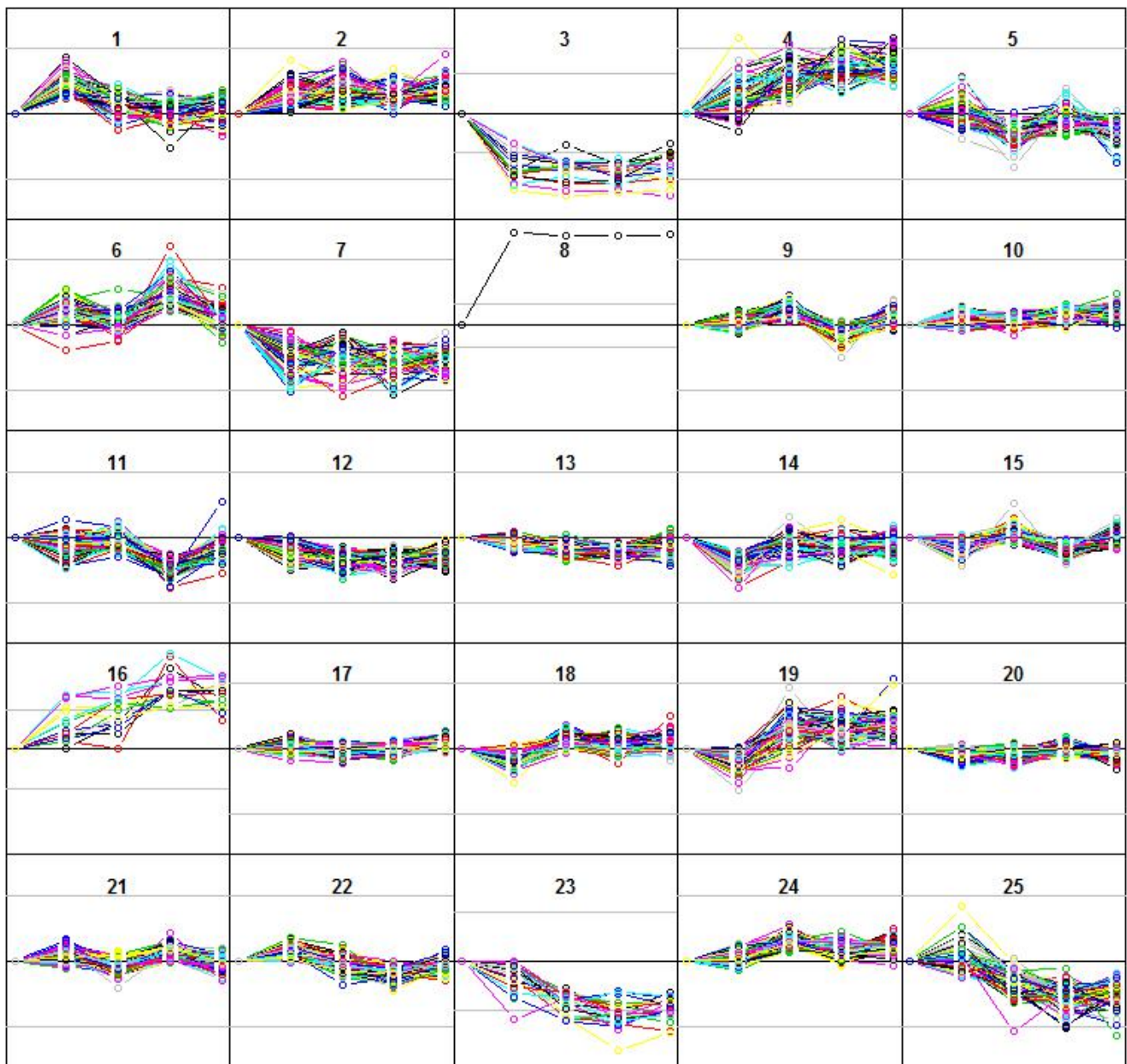
Figure S5B. Bright field images of N202 cells growing in three successive passages (P1-3) of independently adapting lineages on brain tissue illustrating that vascularization is robust for all passages.

Figure S6. Biological replicate of transplantation of N202 tumor cell spheroids to brain tissue. This biological replicate was performed exactly as the initial experiment. There is no reason to anticipate that the rate of evolution in two independent experiments would be identical. Therefore, we sought to match the two sequential passages repP1 and repP2 from the replicate experiment to the appropriate position in the original time course, P0-P4. To achieve this, a spline curve was fit to every gene in the plot of passage vs. RMA-normalized gene expression signal. We used these spline curves to fill a matrix of interpolated intermediate values for each gene at intermediate passages, e.g. P0, P0.002, P0.004,...P4.000. We then calculated the sum of absolute differences between repP1 and every column in this matrix, and assigned repP1 to the column in the matrix where this statistic was minimum. The position assignment was based on 1000 random “bootstrap” samples of 100 randomly sampled genes. This was repeated for repP2. Histograms indicated that repP1 and repP2 fit best at P2.65 (blue) and P3.82 (red), respectively. The grey line corresponds to original P2 as an algorithm check.

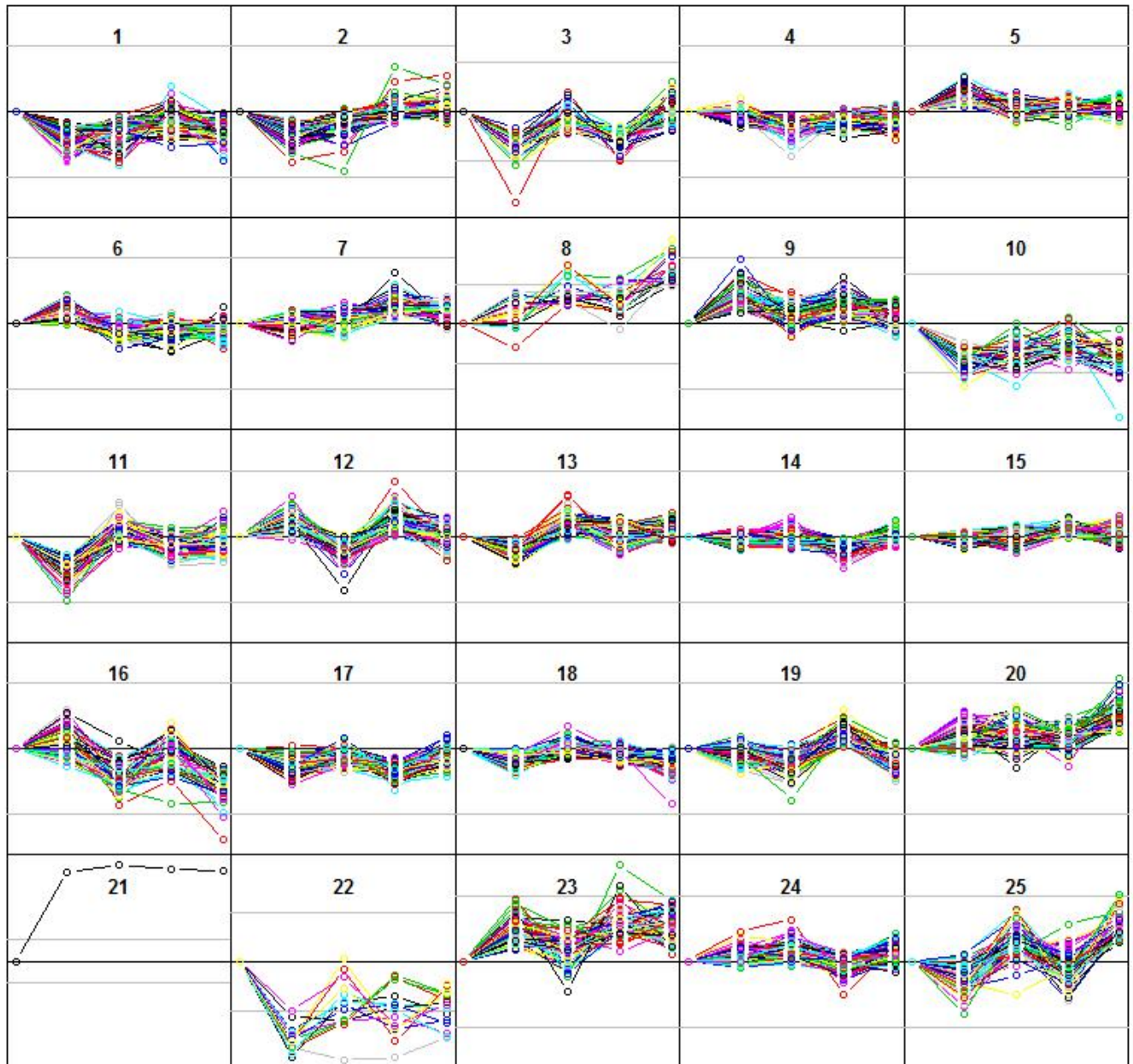
Adaptation to Pseudo-Brain



Adaptation to Pseudo-Bone Marrow



Adaptation to Pseudo-Lung



1. A. Kozlenkov *et al.*, *J Bone Miner Res* **19**, 1862 (Nov, 2004).
2. M. Selamnia, C. Mayeur, V. Robert, F. Blachier, *Biochem Pharmacol* **55**, 1241 (Apr 15, 1998).
3. A. Masood *et al.*, *Br J Haematol* (Dec 15, 2011).
4. T. Oltersdorf *et al.*, *Nature* **435**, 677 (Jun 2, 2005).
5. M. H. Kang, C. P. Reynolds, *Clin Cancer Res* **15**, 1126 (Feb 15, 2009).
6. D. Morikis *et al.*, *Biochem Soc Trans* **32**, 28 (Feb, 2004).
7. S. Ono, Y. Saito, N. Ohgane, G. Kawanishi, F. Mizobe, *Eur J Pharmacol* **155**, 77 (Oct 11, 1988).
8. B. Disse *et al.*, *Life Sci* **52**, 537 (1993).
9. M. M. Stahl, B. Ekstrom, B. Sparf, A. Mattiasson, K. E. Andersson, *Neurourol Urodyn* **14**, 647 (1995).
10. S. Kobayashi, K. Ikeda, M. Suzuki, T. Yamada, K. Miyata, *Jpn J Pharmacol* **86**, 281 (Jul, 2001).
11. E. Buchdunger *et al.*, *Cancer Res* **56**, 100 (Jan 1, 1996).
12. M. C. Heinrich *et al.*, *Blood* **96**, 925 (Aug 1, 2000).
13. D. B. Mendel *et al.*, *Clin Cancer Res* **9**, 327 (Jan, 2003).
14. K. V. Gleixner *et al.*, *Blood* **107**, 752 (Jan 15, 2006).
15. R. E. Tedeschi *et al.*, *Proc Soc Exp Biol Med* **102**, 380 (Nov, 1959).
16. C. N. Stefanis, B. H. Alevizos, G. N. Papadimitriou, *Int Pharmacopsychiatry* **17**, 43 (1982).
17. C. J. Coulson, *Biochem J* **121**, 38P (Feb, 1971).
18. J. A. Zell *et al.*, *J Natl Cancer Inst* **102**, 1513 (Oct 6, 2010).
19. B. Simard *et al.*, *Microvasc Res* **82**, 6 (Jul, 2011).
20. M. Duvic *et al.*, *J Am Acad Dermatol* **44**, 940 (Jun, 2001).
21. S. Bantia *et al.*, *Int Immunopharmacol* **10**, 784 (Jul, 2010).
22. M. Ogura *et al.*, *Cancer Sci* (Mar 26, 2012).
23. M. Boissinot *et al.*, *Leuk Res* **36**, 1304 (Oct, 2012).
24. J. S. Jin, T. Y. Tsao, P. C. Sun, C. P. Yu, C. Tzao, *Pathol Oncol Res* **18**, 713 (Jul, 2012).
25. H. Ueda *et al.*, *J Antibiot (Tokyo)* **47**, 301 (Mar, 1994).
26. J. Avouac *et al.*, *Arthritis Rheum* **64**, 1642 (May, 2012).
27. F. Takahashi *et al.*, *Am J Kidney Dis* **30**, 105 (Jul, 1997).
28. M. R. Hughes *et al.*, *Science* **242**, 1702 (Dec 23, 1988).
29. A. J. Brown, *Am J Kidney Dis* **38**, S3 (Nov, 2001).
30. G. I. Frost, P. Borgstrom, *Methods Mol Med* **85**, 65 (2003).
31. G. I. Frost *et al.*, *Microvasc Res* **69**, 1 (Jan, 2005).
32. P. Oh *et al.*, *Nat Biotechnol* **25**, 327 (Mar, 2007).
33. R. A. Irizarry *et al.*, *Biostatistics* **4**, 249 (Apr, 2003).
34. "R_Development_Core_Team". (2003).
35. Y. Benjamini, Y. Hochberg, *Journal of the Royal Statistical Society Series B* **57**, 289 (1995).

Original Article

Intravital microscopy in the mouse dorsal chamber model for the study of solid tumors

Véronique T. Baron, John Welsh, Parisa Abedinpour, Per Borgström

Vaccine Research Institute of San Diego, San Diego, CA 92121, USA

Received April 11, 2011; accepted April 26, 2011; Epub May 1, 2011; published May 15, 2011

Abstract: Intra-Vital Microscopy (IVM) is used to visualize tumors in animals and analyze various aspects of cancer physiology such as tumor vascularization, cell migration and metastasis. The main advantages of IVM include the real-time analysis of dynamic processes with single-cell resolution. The application of IVM, however, is limited by the availability of animal models that carry visually accessible tumors. These models have evolved over time to become more and more relevant to human tumors. The latest step is the development of a pseudo-orthotopic, syngeneic model for tumor growth and metastasis. In this model, tissue from a variety of mouse organs are grafted in a dorsal skinfold chamber and allowed to revascularize, whereupon tumor cell spheroids are implanted. These spheroids develop into tumors that bear a much closer resemblance to human tumors than xenografts. Unlike xenografts, the vasculature is well-ordered and, because the model is syngeneic, there are no cross-species host immune reactions. The use of fluorescence-tagged pseudo-organs and tumor cells allows IVM analysis and provides real-time access to the development of tumors that closely resemble the real disease. This model can be used to test therapeutics and to image tumor development and stroma-tumor interactions.

Keywords: Intra-Vital Microscopy (IVM), mouse dorsal chamber model, solid tumor, cancer, vascularization, cell migration and metastasis

Introduction

Over 1,5 million new cancer cases and 569,490 deaths from cancer were projected to occur in the United States in 2010 [1]. Cancer incidence rates have decreased in recent times, but despite progress in detection and treatment the death toll remains high and new therapeutic approaches are needed.

There are many physiological aspects to cancer progression that must be understood if we are to fight cancer more effectively [2]. A tumor is not just a mass of cancer cells that are proliferating without control. There are many stresses associated with the development of a tumor that cancer cells need to overcome such as, for example, the lack of oxygen when the tumor mass increases (hypoxia) and the resulting decrease in extracellular pH (acidification), or even the stresses caused by chemo or radiotherapy. As a result, a fraction of cancer cells develop resistance to various forms of cell death. In addition, myriad changes take place in the sur-

rounding tissue that apparently promote tumor survival.

This concept was proposed by Paget in his famous 'seed and soil' hypothesis as early as 1889 [3] and has since been supported by large amounts of data. While a normal tissue environment inhibits the proliferation of cancer cells and slows down tumor formation, disruption of this environment caused by chronic injury, inflammation or hereditary alterations in key genes regulating tissue remodeling may help initiate cancer. In any case, the environment found in the vicinity of tumors is hardly normal, as the stroma reacts to the presence of cancer cells [4, 5]. Stroma changes include the recruitment of cancer-associated fibroblasts, smooth muscle cells and endothelial cells, and of immune cells such as tumor associated macrophages, tumor-infiltrating lymphocytes and leukocytes [6, 7]. Conversely, stroma cells alter the behavior of epithelial cancer cells by secreting extracellular proteins, cytokines, growth factors, proteases, etc. Dramatic changes in gene ex-

pression can be measured in all cell types during cancer progression, including tumor epithelial, stroma endothelial, myofibroblasts, and immune cells. In addition, it now appears that genetic alterations can also arise in the microenvironment of tumors (reviewed in [8]). Thus, reciprocal interactions take place between stromal and epithelial cancer cells that promote cancer progression by increasing cell proliferation, causing the formation of new blood vessels through angiogenesis, remodeling the extracellular matrix, and supporting the metastatic spread of the tumor cells [5, 9, 10].

Metastasis is a complex process in which cancer cells leave a primary organ, migrate through basement membranes and connective tissue into lymphatic or blood vessels, then extravasate into a distant organ to establish a new tumor [11, 12]. Complications resulting from the development of metastases are responsible for 90% of cancer-related death [13]. Designing therapeutic strategies to kill metastatic cells or to prevent their colonization of recipient tissues is, therefore, a major goal of cancer research. Despite its clinical relevance however, metastasis is still poorly understood. There are many unanswered questions regarding how metastatic cells leave the tumor and establish themselves in a new tissue, where they may stay dormant for a long time or immediately grow into a new tumor [14, 15]. It is thought that accumulated genetic and epigenetic changes in a subpopulation of tumor cells eventually allow these cells to undergo the metastatic voyage. In this hypothesis, metastasis is a late result of tumor progression. Another hypothesis, supported by evidence from epidemiological studies, contends that pre-malignant tumor cells can disseminate early and evolve independently from the primary tumor (discussed in [12, 16-18]).

The inability to directly observe dynamic processes in vivo has been a major obstacle to the study of cancer. At present the most relevant animal models of human cancer, such as transgenic mouse models, do not allow for the visualization of the molecular and microenvironmental events that influence tumor formation, growth, vascularization and metastasis. Indeed, solid tumors are often buried inside the body, which precludes direct observation, and metastatic lesions can be detected only once they are established and after the animal is sacrificed. Histological studies (epidemiologic studies in

human, or studies in animal models of cancer) and measurements of tumor size or number of metastatic foci have provided important clues, but with a static view. Thus, extensive autopsies must be performed to reconstruct a time-resolved model of progression. Revascularization, cell migration or adaptation to a new environment during colonization cannot be observed directly, and reconstruction of these parameters using comparative histology is problematic because each tumor is different. New whole-body imaging technologies represent a real progress in cancer research as they now measure tumor growth in real-time and detect metastasis at relatively early stages [19-22]. However, it is still very difficult to detect small metastases either in patients or in animal models, and events that occur at intermediate phases of cancer progression cannot be monitored. Intravital Microscopy (IVM) is a powerful tool for the real-time visualization of previously unobserved mechanisms, thereby providing crucial information regarding several aspects of cancer progression and metastasis. In this review, we discuss the design of animal models of cancer that are compatible with the use of IVM.

Advantages of IVM

Interest in IVM has been renewed by the recent availability of very sophisticated imaging technologies and the constant improvements in molecular probes and analysis tools.

The history of IVM and new advances in imaging techniques are thoroughly reviewed in [23], whereas detailed descriptions of imaging technologies including fluorescent light microscopy, laser-scanning confocal microscopy, laser-scanning multiphoton microscopy, are described in [24]. Earlier studies commonly used in vivo dyes such as rhodamine-based CMTMR to visualize cancer cells or animal tissue. Later on, cells were rendered permanently fluorescent by stable expression of GFP-fusion proteins. There are now many more options with the availability of multiple fluorescence colors, FRET, the possibility to distinguish tissues in the recipient animals using fluorescent transgenics [25, 26], and the possibility to stain tumor cells cytoplasm and nucleus with different colors [27].

The main advantage of IVM is the real-time visualization of cellular events at a very high resolu-

tion. IVM permits the direct observation of dynamic cellular processes while they are taking place and the high magnification of images shows transitional mechanisms at the cellular level, or even at the molecular level. For example Tada et al. successfully tracked single-particle quantum dots conjugated with HER-antibodies to analyze the molecular mechanism behind the transport of drug carriers in vivo [28]. Time scales of observation vary from seconds to several weeks. In a study that strikingly illustrates the real-time possibilities of dynamic IVM, the binding of fluorophore-conjugated antibody to endothelial cells could be visualized in vivo, demonstrating that caveolae operate as pumps and move the antibody *within seconds* from the blood across the endothelium into lung tissue [29]. Events that take place within hours are extremely easy to follow, whereas observations can be made over days or weeks if precautions are taken to “label” the area of observation and ensure that the same region is being observed. For example, in their study in mouse mammary chambers, Kedrin et al. “optically marked individual tumor cells expressing photoswitchable proteins” to monitor the migration of defined groups of cells over time [30].

Importantly, IVM offers the possibility to follow tumor growth in a non-invasive, non-destructive manner. Tumor-related parameters can be measured in living animals and in real-time, including tumor growth or regression, angiogenesis, infiltration by immune cells, tumor cell migration, all in the context of the host. Since repeated measurements of physiological parameters can be made from the same animal, the technique considerably reduces the number of animals needed to obtain a time-resolved picture of cancer progression compared to methods that require euthanizing animals at each time-point.

Unique observations have been made in several areas of cancer, particularly angiogenesis and cancer cells migration. For example, IVM was applied to the study of tumor microcirculation and lymphatic systems and showed that the tumor vasculature in xenograft tumors is characterized by a variety of structural and functional abnormalities that impair blood flow, resulting in the appearance of zones of necrosis and/or hypoxia (reviewed in [31]). The high resolution of IVM also allows the visualization of microvessels and capillaries. Therefore, very

detailed studies can be performed about blood vessel formation, blood flow, leakage, migration of cancer cells through vessel walls during intravasation or extravasation (migration of cells from the tumor into a blood vessel, or migration of tumor cells from the blood vessel into the tissue, respectively). The reader will find further review of the use of IVM applied to angiogenesis research in [32] and [33].

Another remarkable application of IVM is the observation of cell migration patterns within primary tumors, which is impossible to track in real-time using other approaches (See [23, 34] for reviews of IVM works on metastasis). Indeed, high resolution IVM allows one to visualize how cancer cells migrate within a tumor, then break away from the tumor and intravasate into blood vessels [35, 36]. Tracking cells inside tumors using IVM revealed heterogeneity within a tumor, with differences in how cells migrate in different areas of the tumor. Sahai’s laboratory suggested that cancer cells chose between several migratory mechanisms depending on the microenvironment. Cancer cells undergo an epithelial-to-mesenchymal transition and acquire fibroblast-like migratory properties, or they use amoeboid moves similar to leukocytes in order to invade surrounding tissue [37, 38].

The mouse dorsal skinfold chamber model

The application of IVM to the study of cancer is limited by the availability of animal models that bear visually accessible tumors. Therefore, the implantation of transparent windows (“chambers”) on rodents was invented to enable microscopic observations in cancer research. The dorsal skinfold chamber model is used extensively with hamsters for the study of microcirculation and angiogenesis [39]. Chambers in rats have also been used to investigate cancer, but rat models lack the versatility of mouse models. The elegant dorsal skinfold model was described by Algire in 1943. Recent reviews provide an excellent technical description of the model, including apparatus and surgical procedures, examples of applications and model variations [24, 40]. Briefly, platinum chambers with a viewing transparent window are placed by surgery into the dorsal skin of mice as shown in **Figure 1**, an adaptation described in [41]. Plastic frames, described recently, are lighter than metal ones while maintaining the characteristics of the windows [42].

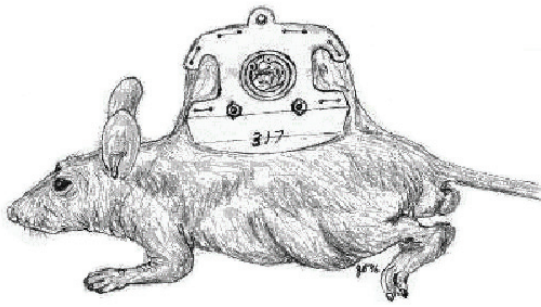


Figure 1. Cartoon illustrating the dorsal skinfold chamber in a nude mouse

An implanted tumor, blood vessels, and host tissue are observed directly through the transparent window. Thus, tumor growth can be visualized and quantified over time along with the development of the vasculature, at high resolution and without tissue damage. This permits “chronic” studies in which repeated analysis are made over a prolonged period. In our laboratory for example, it is now possible to observe tumors for up to 90 days.

Fluorescent tumor-derived cells are implanted under the glass of the chambers. Virtually any strain of mouse can be used. Nude or SCID immunodeficient mice are used to implant human cells, whereas syngeneic mice may be used for the implantation of mouse cancer cells, such as tumor cell lines derived from transgenic models of cancer. Alternatively, small pieces of a growing tumor, originating from xenografts or from transgenic mice, can be implanted either dissociated or as small fragments. This provides less control over cell composition, since tumors are more heterogeneous than cell lines (although cells dissociated from tumors can be sorted by flow cytometry). However, tumor tissues usually do not stably express fluorescent proteins and vital dyes need to be used instead, limiting the total period of observation. Alternatively, tumor tissue can be obtained from human patients.

A few laboratories, including ours, use tumor cells transfected with histone H2B-GFP fusion protein, which was initially developed by Kanda et al. for the observation of chromosome dynamics in living cells [43]. Histone H2B-GFP is incorporated into the chromatin without affecting cell cycle progression. Following implantation of H2B-GFP-transfected cells in mouse chambers, the development of the resultant tumors is followed by IVM in living animals and

as a function of time. Tumor cell fluorescence allows one to measure angiogenic activity, infiltration by immune cells, tumor cell migration, and parameters pertaining to tumor growth or regression such as mitosis, apoptosis and cell cycle arrest [44-47]. The number of cancer cells in a growing tumor can be determined accurately from the fluorescence intensity by using a calibration curve [47, 48]. H2B-GFP makes it very simple to visualize metaphase-telophase DNA and apoptotic/pyknotic nuclei using high magnification images. Therefore the number of cells undergoing mitosis or apoptosis can be calculated. Finally, vascular parameters (vascular area, vascular length; average tumor vessel diameter and vascular density) are analyzed and calculated from video recordings using a photodensitometric computer software [49, 50]. Dual color analysis is achieved by implanting red-fluorescent cells in GFP-mice, or green-fluorescent tumor cells into red fluorescent mice [26, 51]. This strategy provides high-resolution images in which the vasculature, the host tissue, and immune cells can easily be distinguished from the implanted tumor cells.

A major drawback of the dorsal skinfold chamber model, however, lies in its limited relevance to tumor physiology. This model is, in fact, quite similar to the traditional sub-cutaneous xenograft model and similarly fails to represent many aspects of clinical cancer, especially with regard to metastasis, drug sensitivity and angiogenesis (xenograft tumors are notoriously poorly vascularized). Mouse cancer cells can be implanted in syngeneic animals, whereas human tumors can be studied using nude or SCID mice [52], but large numbers of human cells, usually between 10^6 and 10^7 cells, have to be injected for the tumor to survive and grow. While many human tumor cells successfully form tumors in the chamber model in these conditions, some cell lines fail to grow and undergo massive apoptosis [46]. We have found that the human tumors that do grow in the chamber often become encapsulated, thereby excluding macrophages and other immune cells that normally infiltrate the tumor mass. Tumor-associated macrophages (TAMs) have a dual influence. On the one hand, they may facilitate angiogenesis, tumor cell proliferation, and metastasis during tumor progression. On the other hand, TAMs also participate in the immune anti-tumor defense through cytotoxic activities [53]. **Figure 2** (A, B) shows micro-photographs obtained after implantation of HT1080 human fibrosarcoma

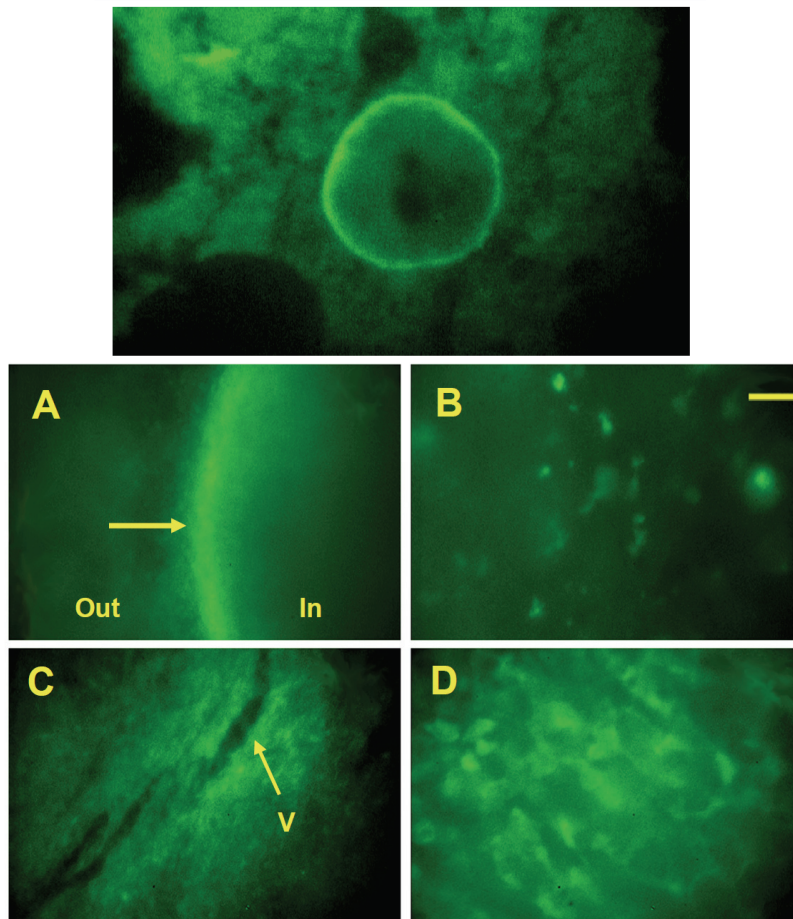


Figure 2. Growth of human tumor cells HT1080 (A, B) and growth of mouse tumor cells (C, D) in the dorsal skinfold chamber. Non-fluorescent tumor cells were implanted in the dorsal chambers of nude mice that had previously been irradiated and transplanted with GFP+ bone marrow. A successfully growing human tumor becomes encapsulated (arrow in panel A), effectively excluding bone marrow-derived cells from the tumor, and is poorly vascularized. Mouse tumors do not become encapsulated, but vascularize (V=blood vessel in panel C). Note the denser bone marrow-derived microenvironment (green cells) in mouse tumors (panel D) compared to human tumors (panel B). Yellow bar = 25 μ m in panels B and D; 100 μ m in panels A and C. Reproduced with permission from Frost et al., *In Vivo* (2003) 17(5):377-88.

cells, which became encapsulated. We were able to demonstrate that human tumors that failed to encapsulate were massively infiltrated by macrophages, and that these tumors were, in fact, eliminated by the mouse innate immune system [46]. In contrast, syngeneic tumors formed from mouse LLC cells (Lewis Lung Carcinoma) were not encapsulated and bone marrow cells, including macrophages, were recruited as shown in **Figure 2C, D**. Thus, the inability to effectively exclude the innate immune system by encapsulation was a main impediment to the survival of small human micro-tumors in the dorsal skinfold chamber in nude mice.

Stroma in the chamber model: the syngeneic pseudo-orthotopic dorsal chamber model

There is now a large body of literature indicating that the tumor microenvironment is crucial for the progression of almost every type of cancer and that orthotopic implantation of cancer cells

recapitulate human disease much more closely than subcutaneous implantation [54]. Tumors grow faster and develop better vasculature when the cancer cells are implanted into the relevant organ. In addition, many tumors do not form metastases unless they are implanted orthotopically. Orthotopic implantation also enhances the tumorigenicity with respect to tumor growth and penetrance. This explains, in part, why the various types of cancer that have been modeled in transgenic mice mimic human cancer much more faithfully than xenograft models. However, many solid epithelial tumors that develop in transgenic animals or following orthotopic implantation are difficult to observe because they arise deep in the body.

The very distinctive benefit of the chamber model is to make possible the visualization of tumors that are normally buried and inaccessible, such as pancreatic, prostate or lung tumors. Still, the dorsal skinfold represents a non-

orthotopic environment for most tumors except melanomas. In an insightful study, Shan et al. describe a method in which a microscope window was placed over the mammary gland of female rats to examine angiogenesis and the proliferation of breast cancer cells in an orthotopic environment [55]. Through the use of fluorescent tags and “photoswitching” in mouse mammary windows, Kedrin et al. stained tumor cells differently in various tumor areas to demonstrate that the microenvironment around tumor blood vessels was more supportive of metastatic behaviors than areas away from blood vessels [30]. Thus, mammary windows will allow one to directly observe cancer cell growth and division, migration, invasion and intravasation within mammary gland microenvironments. While this approach does, indeed, elegantly solve the problem of monitoring tumor development in the orthotopic environment for mammary tumors, it does not apply to other tumors of interest such as prostate or lung cancer.

To resolve this issue, a novel “pseudo-orthotopic” model has been developed in our laboratory. This method emerged from early experiments showing that various syngeneic tissues grafted in rodent dorsal chambers could re-vascularize and survive over long periods of time [56]. Successfully grafted tissues include spleen, myocardium, spongy bone [56] and adipose tissue [57]. Endometrial tissue was also successfully implanted in dorsal chambers to study angiogenesis and test the efficacy of drugs against endometriosis [58, 59]. In our “pseudo-orthotopic” model, small pieces of orthotopic tissue from donor mice were co-implanted with the tumor cells into the dorsal skinfold chamber of syngeneic C57BL/6 mice to mimic the microenvironment of the tumor. We observed that various types of tissue implanted in the chambers survived and revascularized, and that tumor-derived cell lines thrived upon co-implantation with their respective stroma. For example, we compared the growth characteristics of mouse prostate cancer cells implanted in dorsal chambers with or without prostate tissue. The proliferation of tumor cells was 5 times higher when prostate tissue was present. The vascular area, average vessel diameter, and vascular density were also consistently higher, whereas tumors implanted without prostate tissue were poorly angiogenic [47]. Thus, co-implanting mouse prostate cancer cells with prostate stroma provides the tumor cells with

an environment that better reflects the clinical disease compared to purely subcutaneous models. Importantly, re-vascularized stromal tissue remains viable for long periods of time (up to 2-3 months in our laboratory).

Using this model we demonstrated that androgen ablation through surgical castration induces a profound regression of the vasculature surrounding prostate tumors [47, 60]. Androgen ablation is the standard therapeutic approach to prostate cancer that progresses after surgery and/or radiation therapy. Although control of the disease is always achieved at first, almost all patients then progress to androgen-independent disease. It is generally believed that the initial population of androgen-dependent cells undergoes rapid apoptosis upon hormone withdrawal. However, our data indicate that castration decreases cell proliferation rather than induce apoptosis, and also has anti-angiogenic effects.

The source of the vasculature surrounding the tumor was determined by implanting minced prostate tissue derived from GFP transgenic mice into mouse dorsal chambers. Thus, the implanted green-fluorescent stromal cells can be distinguished from host tissues. We observed that the GFP-positive endothelium in the prostate stroma revascularized with GFP-positive vessels rather than with host vasculature. Thereafter the GFP-positive endothelial cells reattached to the pre-existing vasculature underneath the tumor spheroid and flowing red blood cells could be seen [47]. In another set of experiments, breast cancer cells stably transfected with H2B-mCherry (red) were co-implanted with mammary fat pad tissue from a lactating GFP⁺ mouse and allowed to grow for 2 weeks. Intense GFP fluorescence was detected in the vasculature of the growing tumor, indicating that the engrafted tissue provided the blood vessels to the tumor (unpublished). Thus, tumor-associated vascularization occurs through recruitment of vessels from the co-implanted stromal tissue.

A variety of tissues were successfully implanted including lymph node, prostate, liver, lung, bone marrow, and mammary fat pad. In addition, several cancer cell lines have been successfully grown in the corresponding tissue such as prostate TRAMP-C2 [47, 60], breast N202 [61, 62], ovarian MOVCAR, and renal carcinoma RenCa,

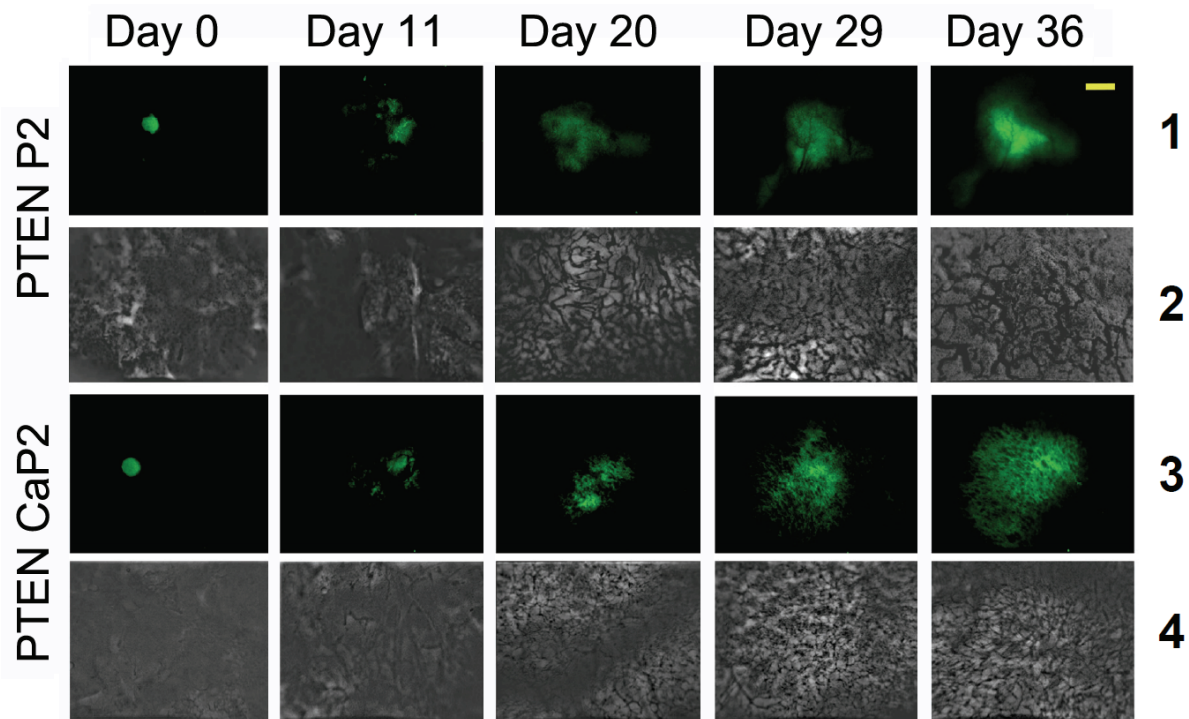


Figure 3. H2B-GFP-positive PTEN-P2 and PTEN-CaP2 cell spheroids were co-implanted with prostate tissue into mouse dorsal chambers. Tumors were imaged at the indicated times using IVM. One can see the increase in tumor size and in tissue vascularization. Yellow bar = 1mm in the tumor panels 1 and 3; 100 μ m in panels 2 and 4.

most of them generated from relevant transgenic models. To improve our prostate cancer model, we now use PTEN-P2 and PTEN-CaP2 mouse carcinoma cell lines. These cells, generated in Dr. H. Wu's laboratory, were derived from PTEN^{+/+} and PTEN^{-/-} transgenic mice, respectively, [63]. The prostate-specific PTEN-deficient mouse model is considered one of the most relevant to human prostate cancer. H2B-GFP was transfected into these cells and green-fluorescent PTEN-P2 and PTEN-CaP2 cell spheroids were implanted on top of prostate tissue from donor mice in the dorsal chamber of recipient mice. **Figure 3** shows pictures of the PTEN-P2 and PTEN-CaP2 micro-tumors growing as a function of time. Tumor growth was reflected by an increase in overall size as well as an increase in the brightness of the tumor area due to a higher density of fluorescent cells within the tumor. These tumors were highly angiogenic. Importantly, the growth characteristics and hormone-dependency of hormone-sensitive prostate tumors (P2 cells) and hormone-insensitive (CaP2 cells) in the pseudo-orthotopic chamber model corresponded to previously pub-

lished data [63]. These tumor cells will be co-implanted with prostate tissue from a tomato mouse [64] for dual-color imaging studies.

Study of metastasis in the chamber model

After cancer cells break away from the primary tumor, enter lymphatic and blood vessels and circulate through the bloodstream, they extravasate and colonize the microenvironment of the distant organ in which they grow into a new tumor [11, 12, 14, 15]. Colonization of distant organs is a rate-limiting step to the formation of metastatic tumors [65]. This process depends greatly on the new microenvironment and on the dynamic and reciprocal interactions that take place between the tumor cells and the stromal cells of the metastatic organ [5, 9, 66]. Unfortunately, what happens during the early stages of development of a metastatic tumor is still unknown. The interactions between disseminated cancer cells and their microenvironment during metastasis have been mostly based on correlation and logically inferred since most animal models of cancer provide only end-

point outcomes. Transgenic mouse models or methods such as tail vein injection of metastatic cells (a model for lung metastasis) do not permit the detection of micrometastases or the measurement of tumor growth in real time, and the metastatic lesions can be analyzed only after the mice are sacrificed. Indeed, it is impossible to predict where metastasis will arise and metastatic tumors are detected only after they are well-established, precluding the study of the early steps of the process. Consequently it is impossible, for example, to tell whether a small tumor in the bone at the time of necropsy is new and aggressive or old and relatively slow-growing. Data must be inferred indirectly and on a statistical basis. Certain inferences are impractical to achieve because the mouse has to be sacrificed for each observation, and therefore can only be done on an average basis. IVM has the potential to solve this problem *almost* completely by continuous monitoring of individual tumors, thereby eliminating uncertainties in interpolation.

Ex-vivo metastasis assays use fluorescent metastatic cancer cells orthotopically implanted in the relevant organ, which then lodge into secondary organs. Cells can also be injected into the tail-vein of mice to lodge in the lungs. Animals are usually sacrificed and the organs resected for IVM measurements as in [67]. Other laboratories use tissue perfusion and direct injection of tumor cells into the perfusion system to extend the time of observation [68]. Using a similar model, Gassman et al. demonstrated that CXCL12, expressed in the endothelial cells of the liver blood vessels, interacted with CXCR4 expressed in the tumor cells, and promoted tumor cell adhesion to the liver blood vessels and extravasation into the liver [69]. A study in which the lungs were perfused and sections of tissue placed on agarose-based medium for up to 21 days, allowing the monitoring of metastatic tumor growth, showed that the survival of cells arriving in lung was the limiting step of metastatic efficiency [70]. In these models, the tissue architecture is maintained, with stromal cells and relevant ECM components. However, some aspects of metastatic tumor growth are lacking such as vascularization or infiltration with immune cells.

This problem is solved, for brain metastasis, by the use of cranial windows that were designed to provide visual access and to examine the

microcirculation in the brain environment following implantation of glioma cells or breast cancer cells, thus mimicking a relevant environment for brain tumors or breast cancer metastases to the brain [40, 71]. For example, Monsky et al. used the cranial window to compare physiological parameters including vascularization of breast cancer cells implanted in mammary windows (orthotopic environment) or in cranial windows (brain metastasis environment), showing among other things that the expression of pro-angiogenic growth factors in a tumor depends on its microenvironment [72].

The pseudo-orthotopic model partially remedies the limitation of organ accessibility. In theory, tumors can be grown on any grafted tissue, to the extent that the pseudo-orthotopic tissue retains the properties of the native tissue, and analysis of several steps of metastatic tumor growth and adaptation can be followed by IVM. Thus, we have compared the adaptation and the growth of breast cancer cells H2B-GFP/N202 in several pseudo-organs relevant to breast cancer metastasis. To generate a pseudo-orthotopic metastasis model, minced mammary fat pad, liver, lung and skin obtained from lactating female mice were implanted into dorsal skinfold chambers of nude mice. H2B-GFP/N202 cells were then implanted on these tissues. The importance of the microenvironment for the growth of N202 tumors was apparent, since tumors grew poorly when co-implanted with tissues other than mammary fat pad (manuscript in preparation). This model thus allows one to study many biological parameters underlying the real-time adaptation of tumor cells to a new environment, particularly in the context of a new host tissue relevant to metastasis.

Testing therapeutics in the chamber model

Because vascular events can be accurately quantified, IVM in the dorsal chamber model is ideally suited to evaluate the efficacy of potential anti-angiogenic drugs. Treatment of vascularized tumors implanted into dorsal skinfold or cranial chambers with neutralizing antibodies against growth factor VEGF induced vascular regression [44, 45, 73, 74]. It was later shown that inhibition of the VEGF receptor (Flk-1) reduced angiogenesis in the peritumoral areas but not in the intratumoral area [75]. High angiogenic activity is required for glioma invasion

of adjacent tissue, suggesting that targeting angiogenesis in glioma may reduce metastasis. Indeed, inhibition of Flk-1 reduced invasion as well as angiogenesis [76]. In an attempt to specifically target the tumor vasculature, a thrombogene was linked to the heparin-binding domain of VEGF. The drug localized to tumor blood vessels *in vivo*, and had potent anti-angiogenic activity [77]. Another work showed that the Notch signaling pathway is involved in angiogenesis because neutralizing one of the Notch ligands blocked angiogenesis and pancreatic tumor growth [78]. Finally, this model is widely used to demonstrate the vascular effects of new anti-angiogenic inhibitors [62, 79-86]. In addition to monitoring the vasculature in real-time, IVM discriminates between the direct effects of a drug on tumor cells and its effects on the vasculature and thus provides a clear picture of its mechanism of action [87-91].

Since orthotopic models are much better suited to predict the effectiveness of chemotherapy than are sub-cutaneous models [54], we argue that pseudo-orthotopic chamber models are very relevant to drug therapy testing [61, 62]. As an example, the effect of COX-2 inhibitor Celecoxib (Celebrex) was investigated in the pseudo-orthotopic dorsal chamber model for prostate cancer using H2B-GFP/TRAMP prostate cancer cells (derived from the tumors of a TRAMP mouse [92]). Celecoxib was administered orally, alone or in combination with castration-induced androgen-withdrawal. *In vitro* and *in vivo* experiments indicated that Celecoxib alone had a direct cytostatic effect on tumor cells in which it induced mitotic arrest followed by cell death. The drug had but little effect on vascular parameters *in vivo*, whereas castration alone caused vascular shrinking, as previously observed [47]. Profound tumor regression was observed with the combination of Celecoxib and androgen-withdrawal, causing a synergistic effect due to decreased vascularization upon androgen withdrawal on the one hand, and growth arrest of tumor cells due mostly to Celecoxib on the other hand. Interestingly, the efficacy of the combination was much better *in vivo* than *in vitro*, because of the separate effects of each treatment on distinct biological compartments that are not represented in cultured cell lines.

To conclude, the pseudo-orthotopic dorsal chamber system is a promising model to evaluate novel therapies for the treatment of cancer

without animal necropsy, and to determine vascular parameters as well as cytostatic or cytotoxic effects. The strengths of this system lie in the relative speed and mechanistic detail by which therapies can be evaluated. In addition, this model recapitulates the native three-dimensional architecture and microenvironment (cells and ECM) of the tumor, with the advantages of an observation window. It extends the possibilities of the cranial and mammary windows by allowing other types of cancer to be studied.

Future directions

Stromal cells in cancer tissue display different gene expression patterns than stromal cells in normal tissue, a result of the bi-directional interactions that take place between stroma and tumor [93, 94]. So far, very few transgenic animals have been generated that display tissue-specific alterations of cancer microenvironments. Such models would be extremely useful in exploring novel therapeutic strategies. The pseudo-orthotopic model, in addition to MIW and cranial chambers, will be used to study the stroma at early stages of metastatic tumor development and to examine the effects of therapeutic treatments targeting the tumor microenvironment that could have synergistic effects when combined with current therapies that target the tumor cells. As tumor growth parameters are tracked in real time, tumors can be harvested when they undergo major adaptive transitions. Thus, it becomes possible to study changes in gene expression, signaling pathways, etc.

Finally, the use of donor animals with defined genetic modifications (such as knock-out and transgenic mice) as source of grafted organ will open new avenues of investigation since it will be possible to examine the role of defined signaling pathways in the survival and growth of metastatic tumors.

Conclusion

New probes and whole-body imaging technologies are a major step for real-time measurements of tumor growth and for the detection of metastases, but still do not accurately visualize early events because they do not provide a way to access information (or, in case of early metastasis, a way of even knowing *where* the information is). IVM goes beyond whole-body imag-

ing to measure single-cell mechanisms and early events with very high resolution. Thus, it has provided us with new, unexpected information regarding the mechanisms of angiogenesis, lymphogenesis, cell motility and invasion processes relevant to early steps of dissemination. Animal models in which IVM can be used are evolving too, allowing a more accurate representation of human cancer. Chamber models, through the design of observations windows at various peripheral locations, have become relevant to the study of stroma-tumor interactions and of later steps of metastasis such as colonization of target organs, which, until recently, were not amenable to direct observation.

Acknowledgements

This work was supported by UC/CBRP grant 151B-0133 and DOD-OCRP grant W81XWH-09-1-0280 (PB) and by NIH/NCI grant CA133638 (JW).

Address correspondence to: Véronique Baron and Per Borgström, Vaccine Research Institute of San Diego (VRISD), 10835 Road to the Cure, Suite 150, San Diego, CA 92121, USA. Phone: (858) 775-1736; Email Véronique Baron: vbaron@sdibr.org and Per Borgström: pborgstrom@sdibr.org

References

- [1] Jemal A, Siegel R, Xu J and Ward E. Cancer statistics, 2010. *CA Cancer J Clin* 2010; 60: 277-300.
- [2] Hanahan D and Weinberg RA. Hallmarks of cancer: the next generation. *Cell* 2011; 144: 646-674.
- [3] Paget S. The distribution of secondary growths in cancer of the breast. 1889. *Cancer Metastasis Rev* 1989; 8: 98-101.
- [4] Hu M and Polyak K. Microenvironmental regulation of cancer development. *Curr Opin Genet Dev* 2008; 18: 27-34.
- [5] Psaila B and Lyden D. The metastatic niche: adapting the foreign soil. *Nat Rev Cancer* 2009; 9: 285-293.
- [6] Bhowmick NA and Moses HL. Tumor-stroma interactions. *Curr Opin Genet Dev* 2005; 15: 97-101.
- [7] Fukino K, Shen L, Matsumoto S, Morrison CD, Mutter GL and Eng C. Combined total genome loss of heterozygosity scan of breast cancer stroma and epithelium reveals multiplicity of stromal targets. *Cancer Res* 2004; 64: 7231-7236.
- [8] Eng C, Leone G, Orloff MS and Ostrowski MC. Genomic alterations in tumor stroma. *Cancer Res* 2009; 69: 6759-6764.
- [9] Joyce JA and Pollard JW. Microenvironmental regulation of metastasis. *Nat Rev Cancer* 2009; 9: 239-252.
- [10] Polyak K, Haviv I and Campbell IG. Co-evolution of tumor cells and their microenvironment. *Trends Genet* 2009; 25: 30-38.
- [11] Molloy T and van 't Veer LJ. Recent advances in metastasis research. *Curr Opin Genet Dev* 2008; 18: 35-41.
- [12] Nguyen DX, Bos PD and Massague J. Metastasis: from dissemination to organ-specific colonization. *Nat Rev Cancer* 2009; 9: 274-284.
- [13] Loberg RD, Bradley DA, Tomlins SA, Chinnaiyan AM and Pienta KJ. The lethal phenotype of cancer: the molecular basis of death due to malignancy. *CA Cancer J Clin* 2007; 57: 225-241.
- [14] Talmadge JE and Fidler IJ. AACR centennial series: the biology of cancer metastasis: historical perspective. *Cancer Res* 2010; 70: 5649-5669.
- [15] Chaffer CL and Weinberg RA. A perspective on cancer cell metastasis. *Science* 331: 1559-1564.
- [16] Ansieau S, Hinkal G, Thomas C, Bastid J and Puisieux A. Early origin of cancer metastases: dissemination and evolution of premalignant cells. *Cell Cycle* 2008; 7: 3659-3663.
- [17] Dong F, Budhu AS and Wang XW. Translating the metastasis paradigm from scientific theory to clinical oncology. *Clin Cancer Res* 2009; 15: 2588-2593.
- [18] Klein CA. Parallel progression of primary tumours and metastases. *Nat Rev Cancer* 2009; 9: 302-312.
- [19] Kaijzel EL, van der Pluijm G and Lowik CW. Whole-body optical imaging in animal models to assess cancer development and progression. *Clin Cancer Res* 2007; 13: 3490-3497.
- [20] Dufort S, Sancey L, Wenk C, Josserand V and Coll JL. Optical small animal imaging in the drug discovery process. *Biochim Biophys Acta* 2010; 1798: 2266-2273.
- [21] Luker GD and Luker KE. Optical imaging: current applications and future directions. *J Nucl Med* 2008; 49: 1-4.
- [22] Henriquez NV, van Overveld PG, Que I, Buijs JT, Bachelier R, Kaijzel EL, Lowik CW, Clezardin P and van der Pluijm G. Advances in optical imaging and novel model systems for cancer metastasis research. *Clin Exp Metastasis* 2007; 24: 699-705.
- [23] Beerling E, Ritsma L, Vrizekoop N, Derksen PW and van Rheenen J. Intravital microscopy: new insights into metastasis of tumors. *J Cell Sci* 2011; 124: 299-310.
- [24] Makale M. Intravital imaging and cell invasion. *Methods Enzymol* 2007; 426: 375-401.
- [25] Hoffman RM. The multiple uses of fluorescent proteins to visualize cancer in vivo. *Nat Rev Cancer* 2005; 5: 796-806.
- [26] Hoffman RM. Imaging cancer dynamics in vivo

- at the tumor and cellular level with fluorescent proteins. *Clin Exp Metastasis* 2009; 26: 345-355.
- [27] Hoffman RM. Real-time subcellular imaging in live animals: new visible targets for cancer drug discovery. *IDrugs* 2006; 9: 632-635.
- [28] Tada H, Higuchi H, Wanatabe TM and Ohuchi N. In vivo real-time tracking of single quantum dots conjugated with monoclonal anti-HER2 antibody in tumors of mice. *Cancer Res* 2007; 67: 1138-1144.
- [29] Oh P, Borgstrom P, Witkiewicz H, Li Y, Borgstrom BJ, Chrastina A, Iwata K, Zinn KR, Baldwin R, Testa JE and Schnitzer JE. Live dynamic imaging of caveolae pumping targeted antibody rapidly and specifically across endothelium in the lung. *Nat Biotechnol* 2007; 25: 327-337.
- [30] Kedrin D, Gligorijevic B, Wyckoff J, Verkhusha VV, Condeelis J, Segall JE and van Rheenen J. Intravital imaging of metastatic behavior through a mammary imaging window. *Nat Methods* 2008; 5: 1019-1021.
- [31] Fukumura D, Duda DG, Munn LL and Jain RK. Tumor microvasculature and microenvironment: novel insights through intravital imaging in pre-clinical models. *Microcirculation* 2010; 17: 206-225.
- [32] Sckell A and Leunig M. The dorsal skinfold chamber: studying angiogenesis by intravital microscopy. *Methods Mol Biol* 2009; 467: 305-317.
- [33] Lunt SJ, Gray C, Reyes-Aldasoro CC, Matcher SJ and Tozer GM. Application of intravital microscopy in studies of tumor microcirculation. *J Biomed Opt* 2011; 15: 011113.
- [34] MacDonald IC and Chambers AF. Breast cancer metastasis progression as revealed by intravital videomicroscopy. *Expert Rev Anticancer Ther* 2006; 6: 1271-1279.
- [35] Condeelis J and Segall JE. Intravital imaging of cell movement in tumours. *Nat Rev Cancer* 2003; 3: 921-930.
- [36] Condeelis J, Singer RH and Segall JE. The great escape: when cancer cells hijack the genes for chemotaxis and motility. *Annu Rev Cell Dev Biol* 2005; 21: 695-718.
- [37] Sahai E. Illuminating the metastatic process. *Nat Rev Cancer* 2007; 7: 737-749.
- [38] Madsen CD and Sahai E. Cancer dissemination—lessons from leukocytes. *Dev Cell* 2010; 19: 13-26.
- [39] Menger MD, Laschke MW and Vollmar B. Viewing the microcirculation through the window: some twenty years experience with the hamster dorsal skinfold chamber. *Eur Surg Res* 2002; 34: 83-91.
- [40] Brown E, Munn LL, Fukumura D and Jain RK. In vivo imaging of tumors. *Cold Spring Harb Protoc* 2010; 2010: pdb prot5452.
- [41] Lehr HA, Leunig M, Menger MD, Nolte D and Messmer K. Dorsal skinfold chamber technique for intravital microscopy in nude mice. *Am J Pathol* 1993; 143: 1055-1062.
- [42] Ushiyama A, Yamada S and Ohkubo C. Microcirculatory parameters measured in subcutaneous tissue of the mouse using a novel dorsal skinfold chamber. *Microvasc Res* 2004; 68: 147-152.
- [43] Kanda T, Sullivan KF and Wahl GM. Histone-GFP fusion protein enables sensitive analysis of chromosome dynamics in living mammalian cells. *Curr Biol* 1998; 8: 377-385.
- [44] Borgstrom P, Gold DP, Hillan KJ and Ferrara N. Importance of VEGF for breast cancer angiogenesis in vivo: implications from intravital microscopy of combination treatments with an anti-VEGF neutralizing monoclonal antibody and doxorubicin. *Anticancer Res* 1999; 19: 4203-4214.
- [45] Borgstrom P, Hillan KJ, Sriramaraio P and Ferrara N. Complete inhibition of angiogenesis and growth of microtumors by anti-vascular endothelial growth factor neutralizing antibody: novel concepts of angiostatic therapy from intravital videomicroscopy. *Cancer Res* 1996; 56: 4032-4039.
- [46] Frost GI, Dudouet B, Lustgarten J and Borgstrom P. The roles of epithelial-mesenchymal interactions and the innate immune response on the tumorigenicity of human prostate carcinoma cell lines grown in immuno-compromised mice. *In Vivo* 2003; 17: 377-388.
- [47] Frost GI, Lustgarten J, Dudouet B, Nyberg L, Hartley-Asp B and Borgstrom P. Novel syngeneic pseudo-orthotopic prostate cancer model: vascular, mitotic and apoptotic responses to castration. *Microvasc Res* 2005; 69: 1-9.
- [48] Huang Y, Tyler T, Saadatmandi N, Lee C, Borgstrom P and Gjerset RA. Enhanced tumor suppression by a p14ARF/p53 bicistronic adenovirus through increased p53 protein translation and stability. *Cancer Res* 2003; 63: 3646-3653.
- [49] Frost GI and Borgstrom P. Real time in vivo quantitation of tumor angiogenesis. *Methods Mol Med* 2003; 85: 65-78.
- [50] Torres Filho IP, Hartley-Asp B and Borgstrom P. Quantitative angiogenesis in a syngeneic tumor spheroid model. *Microvasc Res* 1995; 49: 212-226.
- [51] Hoffman RM. Orthotopic metastatic (MetaMouse) models for discovery and development of novel chemotherapy. *Methods Mol Med* 2005; 111: 297-322.
- [52] Leunig M, Yuan F, Menger MD, Boucher Y, Goetz AE, Messmer K and Jain RK. Angiogenesis, microvascular architecture, microhemodynamics, and interstitial fluid pressure during early growth of human adenocarcinoma LS174T in SCID mice. *Cancer Res* 1992; 52: 6553-6560.

- [53] Lissbrant IF, Stattin P, Wikstrom P, Damber JE, Egevad L and Bergh A. Tumor associated macrophages in human prostate cancer: relation to clinicopathological variables and survival. *Int J Oncol* 2000; 17: 445-451.
- [54] Bibby MC. Orthotopic models of cancer for preclinical drug evaluation: advantages and disadvantages. *Eur J Cancer* 2004; 40: 852-857.
- [55] Shan S, Sorg B and Dewhirst MW. A novel rodent mammary window of orthotopic breast cancer for intravital microscopy. *Microvasc Res* 2003; 65: 109-117.
- [56] Funk W, Endrich B and Messmer K. A novel method for follow-up studies of the microcirculation in non-malignant tissue implants. *Res Exp Med (Berl)* 1986; 186: 259-270.
- [57] Langer S, Sinitsina I, Biberthaler P, Krombach F and Messmer K. Revascularization of transplanted adipose tissue: a study in the dorsal skinfold chamber of hamsters. *Ann Plast Surg* 2002; 48: 53-59.
- [58] Laschke MW, Elitzsch A, Vollmar B, Vajkoczy P and Menger MD. Combined inhibition of vascular endothelial growth factor (VEGF), fibroblast growth factor and platelet-derived growth factor, but not inhibition of VEGF alone, effectively suppresses angiogenesis and vessel maturation in endometriotic lesions. *Hum Reprod* 2006; 21: 262-268.
- [59] Laschke MW, Elitzsch A, Scheuer C, Holstein JH, Vollmar B and Menger MD. Rapamycin induces regression of endometriotic lesions by inhibiting neovascularization and cell proliferation. *Br J Pharmacol* 2006; 149: 137-144.
- [60] Abedinpour P, Baron VT, Welsh J and Borgstrom P. Regression of prostate tumors upon combination of hormone ablation therapy and celecoxib in vivo. *Prostate* 2011;
- [61] Jin H, Aiye A, Su J, Borgstrom P, Stupack D, Friedlander M and Varner J. A homing mechanism for bone marrow-derived progenitor cell recruitment to the neovasculature. *J Clin Invest* 2006; 116: 652-662.
- [62] Tang Y, Borgstrom P, Maynard J, Koziol J, Hu Z, Garen A and Deisseroth A. Mapping of angiogenic markers for targeting of vectors to tumor vascular endothelial cells. *Cancer Gene Ther* 2007; 14: 346-353.
- [63] Jiao J, Wang S, Qiao R, Vivanco I, Watson PA, Sawyers CL and Wu H. Murine cell lines derived from Pten null prostate cancer show the critical role of PTEN in hormone refractory prostate cancer development. *Cancer Res* 2007; 67: 6083-6091.
- [64] Muzumdar MD, Tasic B, Miyamichi K, Li L and Luo L. A global double-fluorescent Cre reporter mouse. *Genesis* 2007; 45: 593-605.
- [65] Chambers AF, Groom AC and MacDonald IC. Dissemination and growth of cancer cells in metastatic sites. *Nat Rev Cancer* 2002; 2: 563-572.
- [66] Chung LW, Baseman A, Assikis V and Zhau HE. Molecular insights into prostate cancer progression: the missing link of tumor micro-environment. *J Urol* 2005; 173: 10-20.
- [67] Chishima T, Miyagi Y, Wang X, Yamaoka H, Shimada H, Moossa AR and Hoffman RM. Cancer invasion and micrometastasis visualized in live tissue by green fluorescent protein expression. *Cancer Res* 1997; 57: 2042-2047.
- [68] Yates C, Shepard CR, Papworth G, Dash A, Beer Stolz D, Tannenbaum S, Griffith L and Wells A. Novel three-dimensional organotypic liver bioreactor to directly visualize early events in metastatic progression. *Adv Cancer Res* 2007; 97: 225-246.
- [69] Gassmann P, Haier J, Schluter K, Domikowsky B, Wendel C, Wiesner U, Kubitz R, Engers R, Schneider SW, Homey B and Muller A. CXCR4 regulates the early extravasation of metastatic tumor cells in vivo. *Neoplasia* 2009; 11: 651-661.
- [70] Mendoza A, Hong SH, Osborne T, Khan MA, Campbell K, Briggs J, Eleswarapu A, Buquo L, Ren L, Hewitt SM, Dakir el H, Garfield S, Walker R, Merlino G, Green JE, Hunter KW, Wakefield LM and Khanna C. Modeling metastasis biology and therapy in real time in the mouse lung. *J Clin Invest* 2010; 120: 2979-2988.
- [71] Yuan F, Salehi HA, Boucher Y, Vasthare US, Tuma RF and Jain RK. Vascular permeability and microcirculation of gliomas and mammary carcinomas transplanted in rat and mouse cranial windows. *Cancer Res* 1994; 54: 4564-4568.
- [72] Monsky WL, Mouta Carreira C, Tsuzuki Y, Gohongi T, Fukumura D and Jain RK. Role of host microenvironment in angiogenesis and microvascular functions in human breast cancer xenografts: mammary fat pad versus cranial tumors. *Clin Cancer Res* 2002; 8: 1008-1013.
- [73] Yuan F, Chen Y, Dellian M, Safabakhsh N, Ferrara N and Jain RK. Time-dependent vascular regression and permeability changes in established human tumor xenografts induced by an anti-vascular endothelial growth factor/vascular permeability factor antibody. *Proc Natl Acad Sci U S A* 1996; 93: 14765-14770.
- [74] Borgstrom P, Bourdon MA, Hillan KJ, Sriramarao P and Ferrara N. Neutralizing anti-vascular endothelial growth factor antibody completely inhibits angiogenesis and growth of human prostate carcinoma micro tumors in vivo. *Prostate* 1998; 35: 1-10.
- [75] Vajkoczy P, Thurnher A, Hirth KP, Schilling L, Schmiedek P, Ullrich A and Menger MD. Measuring VEGF-Flk-1 activity and consequences of VEGF-Flk-1 targeting in vivo using intravital microscopy: clinical applications. *Oncologist* 2000; 5 Suppl 1: 16-19.
- [76] Vajkoczy P, Menger MD, Goldbrunner R, Ge S,

- Fong TA, Vollmar B, Schilling L, Ullrich A, Hirth KP, Tonn JC, Schmiedek P and Rempel SA. Targeting angiogenesis inhibits tumor infiltration and expression of the pro-invasive protein SPARC. *Int J Cancer* 2000; 87: 261-268.
- [77] El-Sheikh A, Borgstrom P, Bhattacharjee G, Belting M and Edgington TS. A selective tumor microvasculature thrombogen that targets a novel receptor complex in the tumor angiogenic microenvironment. *Cancer Res* 2005; 65: 11109-11117.
- [78] Oishi H, Sunamura M, Egawa S, Motoi F, Unno M, Furukawa T, Habib NA and Yagita H. Blockade of delta-like ligand 4 signaling inhibits both growth and angiogenesis of pancreatic cancer. *Pancreas* 2010; 39: 897-903.
- [79] Laird AD, Vajkoczy P, Shawver LK, Thurnher A, Liang C, Mohammadi M, Schlessinger J, Ullrich A, Hubbard SR, Blake RA, Fong TA, Strawn LM, Sun L, Tang C, Hawtin R, Tang F, Shenoy N, Hirth KP, McMahon G and Cherrington. SU6668 is a potent antiangiogenic and antitumor agent that induces regression of established tumors. *Cancer Res* 2000; 60: 4152-4160.
- [80] Hoshida T, Sunamura M, Duda DG, Egawa S, Miyazaki S, Shineha R, Hamada H, Ohtani H, Satomi S and Matsuno S. Gene therapy for pancreatic cancer using an adenovirus vector encoding soluble fit-1 vascular endothelial growth factor receptor. *Pancreas* 2002; 25: 111-121.
- [81] Strieth S, Eichhorn ME, Sauer B, Schulze B, Teifel M, Michaelis U and Dellian M. Neovascular targeting chemotherapy: encapsulation of paclitaxel in cationic liposomes impairs functional tumor microvasculature. *Int J Cancer* 2004; 110: 117-124.
- [82] Strieth S, Nussbaum CF, Eichhorn ME, Fuhrmann M, Teifel M, Michaelis U, Berghaus A and Dellian M. Tumor-selective vessel occlusions by platelets after vascular targeting chemotherapy using paclitaxel encapsulated in cationic liposomes. *Int J Cancer* 2008; 122: 452-460.
- [83] Strieth S, Eichhorn ME, Werner A, Sauer B, Teifel M, Michaelis U, Berghaus A and Dellian M. Paclitaxel encapsulated in cationic liposomes increases tumor microvessel leakiness and improves therapeutic efficacy in combination with Cisplatin. *Clin Cancer Res* 2008; 14: 4603-4611.
- [84] Jiang J, Goel R, Schmechel S, Vercellotti G, Forster C and Bischof J. Pre-conditioning cryosurgery: cellular and molecular mechanisms and dynamics of TNF-alpha enhanced cryotherapy in an in vivo prostate cancer model system. *Cryobiology* 2010; 61: 280-288.
- [85] Cuadros C, Dominguez AL, Frost GI, Borgstrom P and Lustgarten J. Cooperative effect between immunotherapy and antiangiogenic therapy leads to effective tumor rejection in tolerant Her-2/neu mice. *Cancer Res* 2003; 63: 5895-5901.
- [86] Cuadros C, Dominguez AL, Lollini PL, Croft M, Mittler RS, Borgstrom P and Lustgarten J. Vaccination with dendritic cells pulsed with apoptotic tumors in combination with anti-OX40 and anti-4-1BB monoclonal antibodies induces T cell-mediated protective immunity in Her-2/neu transgenic mice. *Int J Cancer* 2005; 116: 934-943.
- [87] Natsume T, Watanabe J, Koh Y, Fujio N, Ohe Y, Horiuchi T, Saijo N, Nishio K and Kobayashi M. Antitumor activity of TZT-1027 (Soblidotin) against vascular endothelial growth factor-secreting human lung cancer in vivo. *Cancer Sci* 2003; 94: 826-833.
- [88] Schacht V, Becker K, Szeimies RM and Abels C. Apoptosis and leucocyte-endothelium interactions contribute to the delayed effects of cryotherapy on tumours in vivo. *Arch Dermatol Res* 2002; 294: 341-348.
- [89] Strelczyk D, Eichhorn ME, Luedemann S, Brix G, Dellian M, Berghaus A and Strieth S. Static magnetic fields impair angiogenesis and growth of solid tumors in vivo. *Cancer Biol Ther* 2009; 8: 1756-1762.
- [90] Al-Jamal KT, Al-Jamal WT, Akerman S, Podesta JE, Yilmazer A, Turton JA, Bianco A, Vargesson N, Kanthou C, Florence AT, Tozer GM and Kostarelos K. Systemic antiangiogenic activity of cationic poly-L-lysine dendrimer delays tumor growth. *Proc Natl Acad Sci U S A* 2010; 107: 3966-3971.
- [91] Debergh I, Van Damme N, Pattyn P, Peeters M and Ceelen WP. The low-molecular-weight heparin, nadroparin, inhibits tumour angiogenesis in a rodent dorsal skinfold chamber model. *Br J Cancer* 2010; 102: 837-843.
- [92] Foster BA, Gingrich JR, Kwon ED, Madias C and Greenberg NM. Characterization of prostatic epithelial cell lines derived from transgenic adenocarcinoma of the mouse prostate (TRAMP) model. *Cancer Res* 1997; 57: 3325-3330.
- [93] Dakhova O, Ozen M, Creighton CJ, Li R, Ayala G, Rowley D and Ittmann M. Global gene expression analysis of reactive stroma in prostate cancer. *Clin Cancer Res* 2009; 15: 3979-3989.
- [94] Gregg JL, Brown KE, Mintz EM, Piontkivska H and Fraizer GC. Analysis of gene expression in prostate cancer epithelial and interstitial stromal cells using laser capture microdissection. *BMC Cancer* 2010; 10: 165.

Regression of Prostate Tumors Upon Combination of Hormone Ablation Therapy and Celecoxib In Vivo

Parisa Abedinpour, Véronique T. Baron, John Welsh, and Per Borgström*

Vaccine Research Institute of San Diego, San Diego, California

BACKGROUND. Hormonal ablation is the standard of treatment for advanced androgen-dependent prostate cancer. Although tumor regression is usually achieved at first, the cancer inevitably evolves toward androgen-independence, in part because of the development of mechanisms of resistance and in part because at the tissue level androgen withdrawal is not fully attained. Current research efforts are focused on new therapeutic strategies that will increase the effectiveness of androgen withdrawal and delay recurrence. We used a syngeneic pseudo-orthotropic mouse model of prostate cancer to test the efficacy of combining androgen withdrawal with FDA-approved COX-2 inhibitor celecoxib.

METHODS. GFP-tagged TRAMP-C2 cells were co-implanted with prostate tissue in the dorsal chamber model and tumors were allowed to establish and vascularize. Tumor growth and angiogenesis were monitored in real-time using fluorescent intravital microscopy (IVM). Androgen withdrawal in mice was achieved using surgical castration or chemical hormonal ablation, alone or in combination with celecoxib (15 mg/kg, twice daily).

RESULTS. Celecoxib alone decreased the growth of prostate tumors mostly by inducing mitotic failure, which resulted in increased apoptosis. Surprisingly, celecoxib did not possess significant angiostatic activity. Surgical or chemical castration prevented the growth of prostate tumors and this, on the other hand, was associated with disruption of the tumor vasculature. Finally, androgen withdrawal combined with celecoxib caused tumor regression through decreased angiogenesis and increased mitosis arrest and apoptosis.

CONCLUSION. Celecoxib, a relatively safe COX-2-selective anti-inflammatory drug, significantly increases the efficacy of androgen withdrawal in vivo and warrants further investigation as a complement therapy for advanced prostate cancer. *Prostate* 71: 813–823, 2011.

© 2010 Wiley-Liss, Inc.

KEY WORDS: prostate cancer; androgen therapy; COX-2; intravital microscopy; celecoxib; celebrex

INTRODUCTION

Current therapeutic interventions for advanced prostate cancer are not curative. Although androgen ablation does initially deliver a response, the return of hormone-refractory tumors invariably prevents long-term patient survival. More effective strategies are needed to extend life expectancy and improve the quality of life for patients with advanced prostate cancer. New strategies may involve the combination of known effective treatments such as androgen withdrawal with drugs that have relatively minor side effects.

Additional Supporting Information may be found in the online version of this article.

Grant sponsor: Pfizer, Inc.; Grant number: COXAV-V0190-010; Grant sponsor: NIH/NCI; Grant numbers: RO1-CA102688, R21CA133638; Grant sponsor: DOD-CDMRP; Grant numbers: W81XWH-09-1-0280, UC/CBCRP 151B-0133.

*Correspondence to: Per Borgström, Vaccine Research Institute of San Diego (VRISD), 10835 Road to the Cure, Suite 150, San Diego, CA 92121. E-mail: pborgstrom@vrisd.org

Received 29 April 2010; Accepted 26 September 2010

DOI 10.1002/pros.21297

Published online 5 November 2010 in Wiley Online Library (wileyonlinelibrary.com).

Cyclooxygenase (COX), the key regulatory enzyme for prostaglandin synthesis, is transcribed from two distinct genes. COX-1 is expressed constitutively in most tissues, while COX-2 expression is normally low and induced by a wide variety of stimuli (it was initially identified as an immediate-early growth response gene). Cyclooxygenases catalyze the formation of prostaglandins (PGs), which are involved in tumor initiation and/or progression. For example, COX-1 and COX-2 promote inflammation, which may directly contribute to the development of prostate cancer [1]. In addition, COX-2-induced PGE2 activates cell signaling involved in proliferation and thereby directly promotes tumor cell growth. COX-2 is overexpressed in prostate cancer and its level of expression correlates with Gleason score and cancer progression [2].

Nonsteroidal anti-inflammatory drugs (NSAIDs) that inhibit both COX-1 and COX-2, as well as COX-2 selective inhibitors, are currently being evaluated clinically for the prevention of major types of cancer because of their positive effects in epidemiological and animal studies. Indeed, a recent meta-analysis of epidemiological studies concluded that NSAIDs—whether or not they are selective for COX-2—have a chemopreventive effect against cancer of the colon, breast, lung, and prostate [3]. In addition, COX-2 promotes angiogenesis and therefore COX-2 inhibitors may impair tumor growth by blocking angiogenesis [4]. Whereas genetic ablation of COX-2 decreases tumor formation in mouse models, its overexpression favors transformation and cancer progression (reviewed in Ref. [2]). COX-2 is overexpressed in a number of malignancies and is associated with increased production of PGE2, which plays a role in the initiation and progression of tumors [2]. It is now well accepted that COX-2 contributes to prostate cancer and the evidence that COX-2 inhibitor celecoxib may be beneficial to prostate cancer patients is mounting [5,6].

In animal models, celecoxib (alone or in combination with another drug) decreased the growth of androgen-independent PC3 xenograft [7] and suppressed the regrowth of LNCaP xenografts following androgen withdrawal [8]. In addition, several clinical studies have started to evaluate the effect of celecoxib in various therapeutic settings. These trials show that celecoxib is safe, with a low cytotoxicity profile. Two studies have described neoadjuvant celecoxib prior to prostatectomy in men with clinically localized prostate cancer, showing measurable amounts of celecoxib in tumors [9] and measurable biological effects in prostate cancer tissue [10] but lacking clear clinical benefit. Other studies have examined the effect of celecoxib in combination with chemotherapy for the treatment of advanced, hormone-independent prostate cancer, without much success [11,12]. A larger trial is under-

way [13], which will provide further information regarding the potential efficacy of celecoxib for advanced prostate cancer. Finally, the efficiency of celecoxib was assessed in patients with recurrent prostate cancer following radiation therapy or radical prostatectomy. A decline or stabilization of PSA levels was observed in both trials, indicative of biological activity and suggesting that the drug may delay the growth of recurrent tumors and extend time before hormone-deprivation therapy [14,15]. Of note, there has been no clinical trial so far to assess whether celecoxib may delay the progression of prostate cancer toward androgen-independence in patients undergoing hormone-deprivation therapy. Thus, more studies are warranted to discover the best use for COX-2 inhibitors and examine the efficacy of various strategies.

We have previously described a syngeneic pseudo-orthotopic model to study prostate cancer progression *in vivo* [16]. This model is based on the dorsal skinfold chamber technique, in which a transparent chamber for microscopy is positioned in the dorsal skinfold of a mouse. Mouse cells derived from the prostate tumor of a TRAMP mouse, known as TRAMP-C2 cells [17], were implanted into mouse dorsal chambers. A H2B-GFP fusion protein was stably introduced into the TRAMP-C2 cells by retroviral transduction. As shown by Kanda et al., [18] the H2B-GFP fusion protein is incorporated into chromatin without affecting cell cycle progression. Because the cells are stably transfected with fluorescent H2B-GFP, tumors can be visualized and imaged *in real time* using intravital fluorescence video-microscopy (IVM). IVM allows measuring tumor growth, vascular parameters and intratumoral mitotic and apoptotic indices. To create a pseudo-orthotopic microenvironment, prostate tissue from a donor mouse was co-implanted with TRAMP-C2-GFP in the chambers. We have shown previously that after 1–2 weeks post-implantation the prostate tissue grafted into the chamber was able to connect its vasculature to the skin vasculature of the recipient mouse, which in turn supported angiogenesis within the growing tumor [16].

The present study investigated the effect of celecoxib alone or in combination with surgical and chemical castration on the growth of TRAMP-C2-GFP tumors.

METHODS

Antibodies and Reagents

Cell culture media, culture-grade PBS, L-glutamine, Trypsin-EDTA, penicillin/streptomycin, and fetal bovine serum (FBS) were from Mediatech (Herndon, VA). G418 and Insulin–Selenium–Transferrin supplement (#41400-Gibco) was from Invitrogen (Carlsbad,

CA). Celecoxib was from Toronto Research Chemicals (Ontario, Canada).

Antibodies against phospho-ERK1/2, PARP, and phospho-histone H3 (Ser10; Ab 6G3) were from Cell Signaling Technology (Danvers, MA). Antibodies to β -actin (AC-15) were from Sigma-Aldrich (St. Louis, MO). Monoclonal anti-p27Kip1 antibodies were from BD Pharmingen (San Jose, CA). Alexa Fluor-488 goat anti-mouse antibodies were from Invitrogen.

Cell Culture

H2B-GFP/TRAMP-C2 (TRAMP-C2-GFP) cells that stably express histone H2B-GFP fusion protein [18] were generated as described [19]. TRAMP-C2-GFP cells were grown in RPMI containing 10% FBS, 2 mM L-glutamine, 100 U/ml penicillin/100 μ g/ml streptomycin, insulin-selenium-transferrin (10 μ g/ml insulin), and DHT 10^{-8} M final. G418 (100 μ g/ml) was added to maintain stable expression of H2B-GFP. Androgen withdrawal was achieved by keeping the cells in phenol red-free RPMI medium containing 10% charcoal-treated FBS and the same supplements as in the normal medium except for DHT.

Human prostate cancer cells DU145 and PC3 were grown in RPMI containing 10% FBS, 2 mM L-glutamine, 100 U/ml penicillin/100 μ g/ml streptomycin. Cells were maintained in a humidified incubator at 37°C and 5% CO₂.

Measurement of Cell Growth In Vitro

Cell growth was monitored by direct counting. Cells in 12-well plates were washed once with PBS, detached using Trypsin, and transferred to a suspension vial in a final volume of 10 ml PBS. Cells were counted using a COULTER™ Multisizer II instrument (Beckman Coulter, Inc., Hialeah, FL) gated for the appropriate cell size and corrected for particulate debris. Each experiment was performed in biological replicates and each vial was counted twice.

Flow Cytometry Quantification of Mitosis

Cells were treated with celecoxib for 24 hr, suspended using trypsin, fixed and permeabilized using BD cytofix/cytoperm solution (BD Pharmingen) according to instructions. Cells were incubated with antibodies to phospho-histone H3 for 30 min, washed three times in BD perm/wash buffer, and stained with Alexa Fluor-488 anti-mouse antibodies for 20 min followed by three more washes. The cells were resuspended at a density of approximately 10^6 cells/0.5 ml in BD perm/wash buffer containing 50 μ g/ml DNase-free RNase A, and 50 μ g/ml propidium iodide. Fluorescence of single cells was recorded using a

Facscan flow cytometer (BD Pharmingen). FlowJo™ Software was used for data analysis.

Western-Blot Analysis of Protein Expression

Cells treated with 40 μ M celecoxib for the indicated times were lysed on ice in the presence of phosphatase and protease inhibitors. Lysates were clarified by centrifugation and the protein concentration in each sample was measured using a BCA assay (Pierce, Rockford, IL). Lysates were submitted to SDS-PAGE electrophoresis. Proteins were transferred to Immobilon-P® membranes (Millipore, Billerica, MA), which were incubated with a blocking buffer for 20 min (Pierce). The first antibody was incubated overnight. Peroxidase-conjugated antibodies (Amersham Biosciences, Piscataway, NJ) were added for 45 min. Proteins were revealed using a chromogenic stabilized substrate from Promega (Madison, WI). When appropriate, membranes were stripped using Restore™ Stripping Buffer (Pierce) for 15 min and reprobed.

Animal Model and Surgical Techniques

Animal experiments have been approved by our Institutional IACUC and were conducted in accordance to NIH guidelines. The dorsal skinfold chambers were prepared as described previously [16,19]. Briefly, male C57/bl6 mice (25–30 g body weight) were anesthetized and placed on a heating pad. Two symmetrical titanium frames were implanted into the dorsal skinfold. A circular layer was excised from one of the skin layers. The underlying muscle and subcutaneous tissues were covered with a glass coverslip incorporated in one of the frames. After a recovery period of 2–3 days, prostate tissue and tumor cells were carefully placed in the chamber.

Preparation of Tumor Spheroids

TRAMP-C2-GFP cells were trypsinized and adjusted to a concentration of 250,000 cells/ml. Cell suspensions were then overlaid into 96-well round bottom plates coated with 1% agarose (100 μ l cell suspension/well). Cell spheroids were allowed to compact for 48 hr and were washed in serum-free medium before implantation into the mouse chambers.

Implantation of Prostate Tissue and Cancer Cells

Anterior prostate tissue was excised from a normal C57/BL6 mouse, minced into small pieces (<1 mm²), and implanted into a chamber. A small indentation was made in the center of the prostate tissue, in which a pre-formed tumor spheroid was placed. The prostate tissue and tumor spheroid were allowed to re-vascularize prior to experimentation.

Surgical Castration

Mice were anesthetized with 7.3 mg ketamine hydrochloride and 2.3 mg xylazine/100 g body weight, i.p. A lateral incision across the scrotum was made and the testes were individually ligated and excised. The wound was cauterized. The incision was then sutured and sealed with Nexaband[®] acrylic.

Chemical Castration

The mice were chemically castrated through oral administration of Cyproterone acetate twice daily (0.5 mg/kg) and injection of Leuprolide acetate daily (0.07 mg/kg).

Celecoxib Treatment

Celecoxib was administered orally twice daily (15 mg/kg/administration).

Intravital Microscopy

Fluorescence microscopy, image analysis, measurement of tumor growth and vascular parameters, calculation of mitotic and apoptotic indices have been carefully detailed in our previous study [16].

RESULTS

TRAMP-C2 cells were derived from the prostate tumor of a TRAMP mouse and were shown previously to have lost the viral SV40-T antigen and to be tumorigenic in vivo [17]. The GFP-tagged cells (TRAMP-C2-GFP) display the same growth characteristics as parental cells and are androgen-dependent in vivo [16], and in vitro (Supplemental Fig. 1).

We first tested the sensitivity of TRAMP-C2-GFP cells to celecoxib in vitro. As shown in Figure 1, a concentration of 20 μ M reduced cell growth by more than 50%, whereas 50 μ M completely inhibited cell growth. It should be noted that these concentrations are within the physiological range. Indeed, average plasma levels achieved by the administration of 800 mg Celecoxib (FDA-approved dose for the treatment of familial adenomatous polyposis) are 8 μ M within 24 hr of administration and can reach up to 40 μ M, whereas even higher peak levels are reached 3 hr post-administration [20–22].

Relevance to human cancer was assessed by measuring the growth of human prostate cancer cells following treatment with celecoxib in similar conditions (Fig. 1). A concentration of 40 μ M was needed to reduce the growth of DU145 and PC3 cells by 50%. Thus, aggressive human prostate cancer cells are also sensitive to celecoxib-induced toxicity, as previously shown by others [8,23–25].

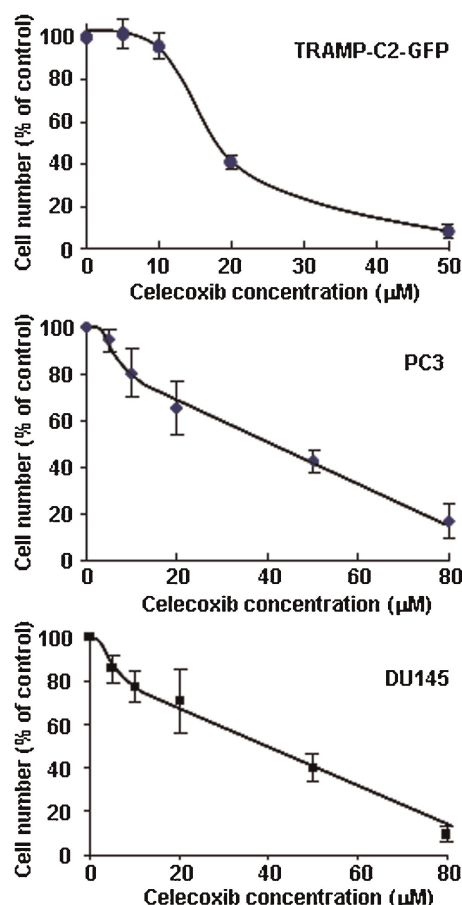


Fig. 1. Effect of celecoxib on the growth of prostate cancer cells in vitro. Mouse TRAMP-C2 cells stably transfected with H2B-GFP (top panel), as well as human prostate cancer cells PC3 (middle panel) and DU145 (bottom panel), were treated with increasing concentrations of celecoxib for 48 hr. Cells were counted using a Cell Coulter Multisizer II as described in Methods Section. Results are expressed relative to untreated cells and are means \pm SEM of three separate experiments, each done in biological duplicates.

The morphology of celecoxib-treated TRAMP-C2-GFP cells was assessed by fluorescent and bright-field microscopy (Fig. 2A). Celecoxib at 10 μ M did not alter the morphology of most cells, although a few cells were observed that contained enlarged nuclei. Some dead cells were observed (thin arrow). The number of cells in mitosis (thick arrows) was higher compared to the control condition. At 20 μ M, celecoxib induced a dramatic change in cell morphology. Most cells had become flat, large cells with enlarged and abnormal nuclei. At 50 μ M, most cells were visibly dying. These observations are consistent with the hypothesis that celecoxib induces growth arrest of TRAMP-C2-GFP cells by impairing mitosis, which is eventually followed by mitotic catastrophe and cell death.

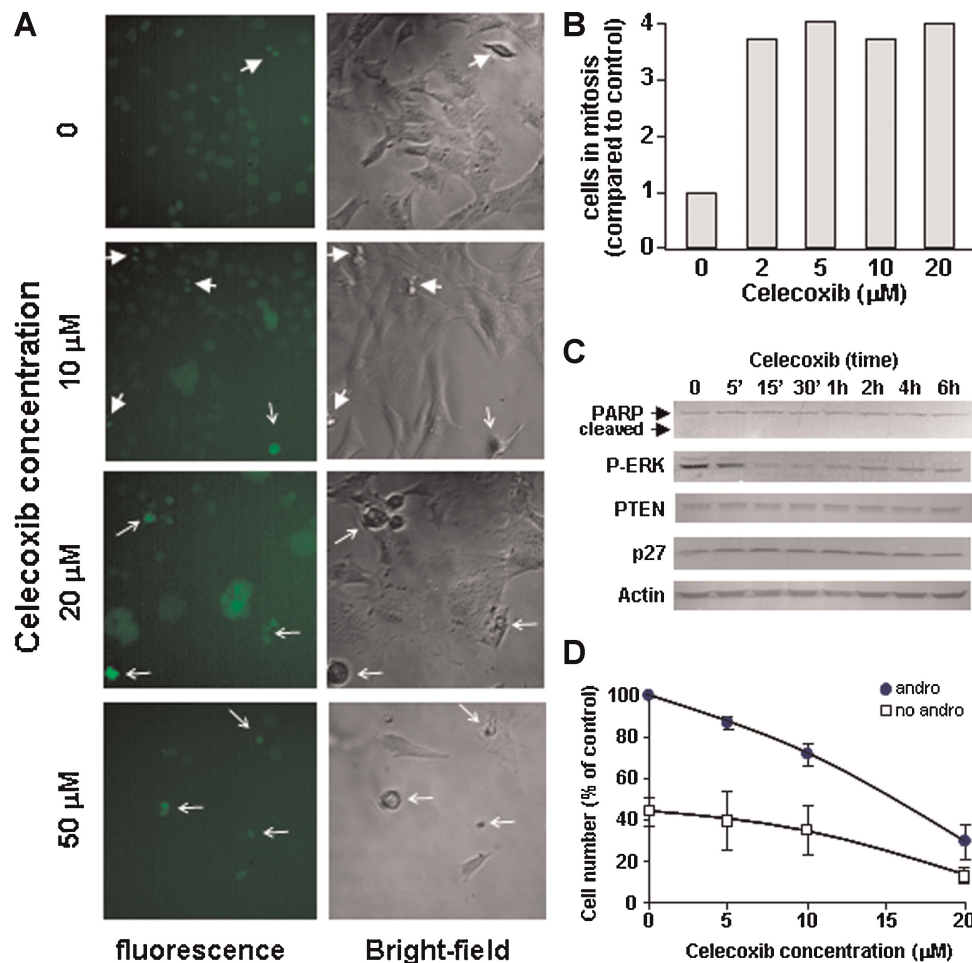


Fig. 2. Effect of celecoxib in TRAMP-C2-GFP prostate cancer cells. **Panel A:** Bright field microscopy (right) and fluorescence microscopy (left) of TRAMP-C2-GFP cells treated with increasing doses of Celecoxib for 48 hr. Thick arrows point to mitotic cells; thin arrows point to dead cells. **Panel B:** Cells were treated with the indicated concentrations of celecoxib for 24 hr. Cells were detached using trypsin, fixed, and co-stained for phospho-H3 (alexa-fluor 488) and DNA content (propidium iodide). The graph shows the proportion of cells in mitosis as compared to control, determined by flow cytometry on Facscan (BD Biosciences). **Panel C:** TRAMP-C2-GFP cells were treated with 40 μM celecoxib for the indicated times. Cells were lysed and protein expression was analyzed by Western-blot. Blot membranes were stripped and re-probed using the indicated antibodies. P-ERK: Phosphorylation-specific antibodies to ERK. **Panel D:** TRAMP-C2-GFP cells were incubated in medium with or without androgen and treated with increasing concentrations of celecoxib for 48 hr before cell counting. Results are expressed relative to untreated cells grown in medium containing androgen, and are means \pm SEM of three separate experiments, each done in biological triplicate.

The effect of celecoxib on mitosis was further validated by flow cytometry analysis. Thus, cells treated with celecoxib were fixed and incubated with antibodies to phospho-histone H3. Phosphorylation of histone H3 on serine 10 is restricted to mitosis and therefore allows to specifically stain mitotic cells. DNA content was measured in parallel by PI staining. The flow cytometry profiles of control (untreated) and cells treated with two doses of celecoxib are shown in Supplemental Figure S2. Celecoxib increased the proportion of mitotic cells by fourfold, an effect that was maximum at the lowest concentration tested (Fig. 2B).

A time-course of celecoxib was performed in TRAMP-C2-GFP cells, and the expression or phosphor-

ylation levels of several proteins were examined by Western-Blot (Fig. 2C). At these early times of treatment (up to 6 hr), celecoxib had no effect on PARP integrity, and did not visibly alter the expression of p27Kip1. No change in the phosphorylation of Akt was seen, although the signal was very weak (data not shown). Low levels of constitutive Akt phosphorylation are not unexpected, since there is no known alteration of the PTEN/PI3-kinase pathway in these cells. However, the cells do exhibit constitutive ERK phosphorylation (Fig. 2C), which was inhibited by celecoxib within 15 min of treatment.

We next examined the hypothesis that hormonal ablation, which is the standard of treatment for

androgen-dependent prostate cancer, may be more efficacious when combined with celecoxib. As shown in Figure 2D, androgen deprivation alone decreased cell proliferation by $56 \pm 11\%$, whereas the combination of androgen deprivation and $20 \mu\text{M}$ celecoxib inhibited cell proliferation by $88 \pm 6\%$. We conclude that in vitro, the combination treatment was more efficient than either treatment alone, although the combined effect was less than additive.

The mouse dorsal chamber was used to evaluate the effect of this combination therapy on tumor growth

in vivo. TRAMP-C2-GFP cell spheroids were co-implanted in the dorsal chambers of mice with prostate tissue obtained from a donor mouse. The implanted prostate tissue and tumor cells were allowed to vascularize for 2 weeks. Once the prostate tissue and the tumor were established, surgical castration was used to induce androgen deprivation (considered day 0 of treatment). Four treatment groups were studied: control untreated mice, castrated mice, celecoxib 15 mg/kg twice daily, celecoxib 15 mg/kg twice daily combined with castration. Figure 3A illustrates the

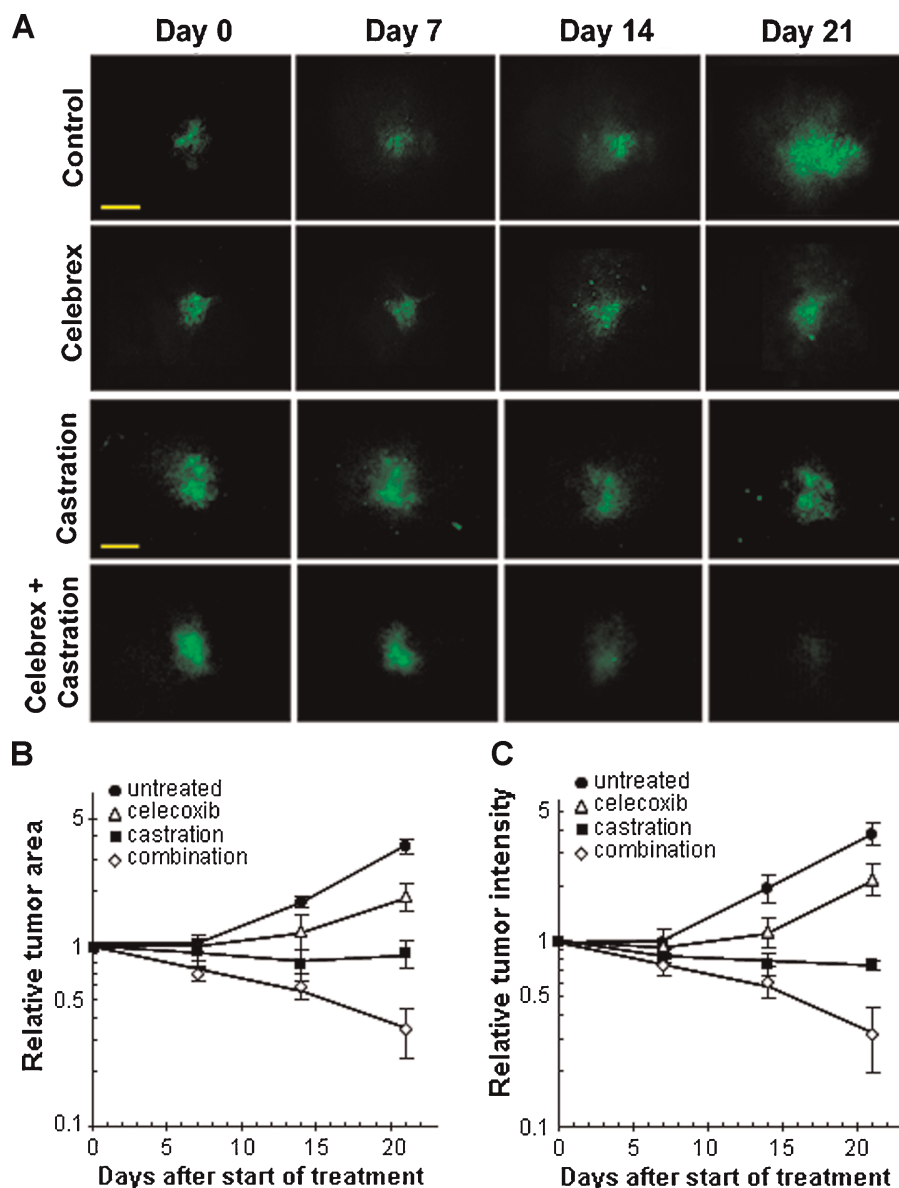


Fig. 3. Effect of celecoxib and/or surgical castration on prostate tumor growth in vivo. TRAMP-C2-GFP cell spheroids were co-implanted with prostate tissue and allowed to vascularize. When there was proper blood flow within the growing tumors, the mice were surgically castrated (Day 0) and Celecoxib treatment (15 mg/kg /administration) was started by oral administration twice daily. Tumors were imaged by intravital microscopy once a week. **Panel A:** A representative collage of tumor growth in the four treatment groups. Bar $\sim 500 \mu\text{m}$. **Panel B and C:** Graphic representation of relative tumor areas (B) and relative tumor intensities (C) calculated from intravital microscopy data (log scale).

effects of celecoxib and castration on tumor growth in our pseudo-orthotopic model, whereas Figure 3B,C depicts the quantification of tumor growth parameters measured by fluorescent intravital microscopy as described in Ref. [16]. The growth of tumors was apparent between days 14 and 21 in the control mice, with a fourfold increase in both tumor area and relative tumor intensity at day 21. Celecoxib caused a significant slowing of tumor growth, since only a twofold increase in both tumor area and tumor intensity was observed after 21 days. In agreement with our previous report [16], castration completely prevented the growth of TRAMP-C2-GFP tumors. However, none of these treatments alone resulted in the regression of established tumors. In contrast, the combination of surgical castration with celecoxib caused a three to fourfold tumor regression. Indeed, a decrease of 80% in tumor area (Fig. 3B), and a decrease of 65% in tumor intensity (Fig. 3C) were observed compared to untreated mice.

The apoptotic and mitotic index of each tumor in this experiment were measured using a higher microscopy magnification (shown in Fig. 4). The initial rate of apoptosis within the tumors decreased fivefold in the control mice, indicative of a high cell survival rate

when the implanted cells start growing into a tumor. In contrast, the rate of apoptosis remained constant, or was somewhat increased, within the tumors of the treated mice.

On the other hand, the mitotic index was stable in the growing tumors of control mice, indicating that the ratio of cells undergoing mitosis remained constant within the cell population. Treatment with celecoxib alone increased the mitotic index fourfold, whereas celecoxib combined with castration caused a fivefold increase in the intratumoral mitotic index, suggesting that many cells arrested in mitosis (Fig. 4B). Close examination of tumor cells nuclei over time (using H2B-GFP fluorescence) allowed us to visualize the onset of mitosis (Fig. 5, Panels A–B). Two days later we observed that cell division failed (Panel C) and the nuclei eventually became pycnotic (Panel D). These observations suggest that celecoxib induced mitotic arrest, leading to mitotic failure and apoptosis.

It had been reported previously that COX-2 inhibitors alter tumor growth in part through an anti-angiogenic activity [26]. Surprisingly, the vascular parameters measured from our experiments showed no difference between control and celecoxib-treated

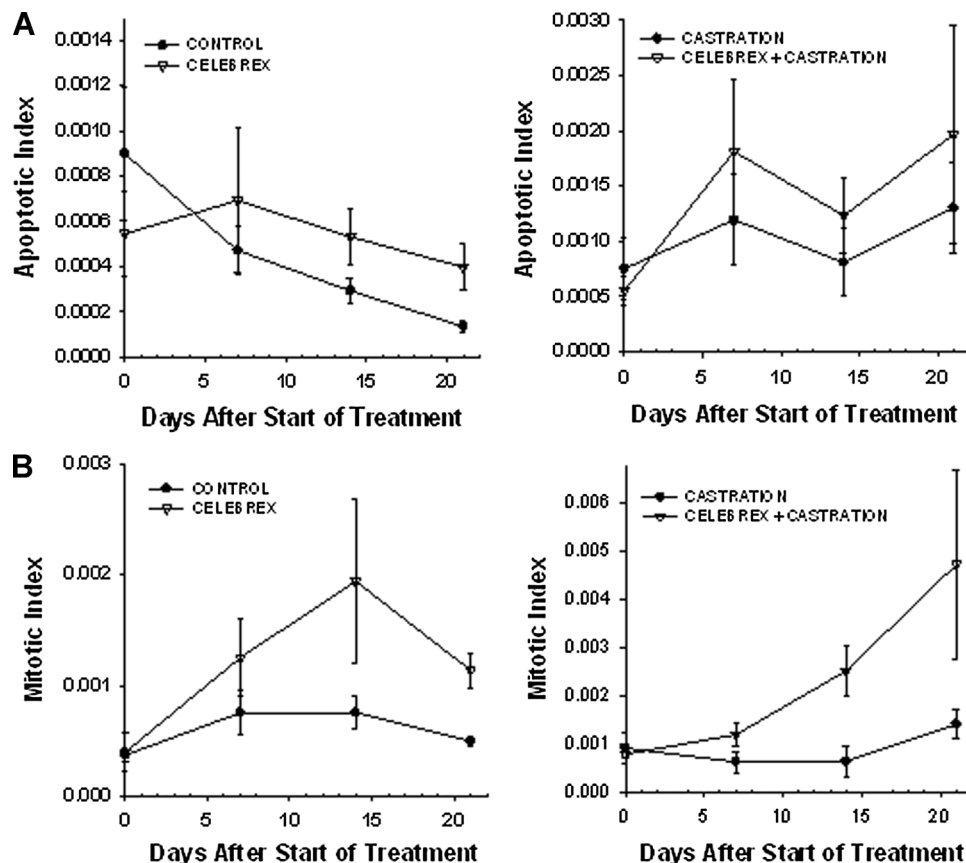


Fig. 4. Mitotic and apoptotic index. Graphic representation of the mean apoptotic index (Panel A) and the mean mitotic index (Panel B) within the tumors, calculated from intravital microscopy data. The animal experiments are the same as described in Figure 2.

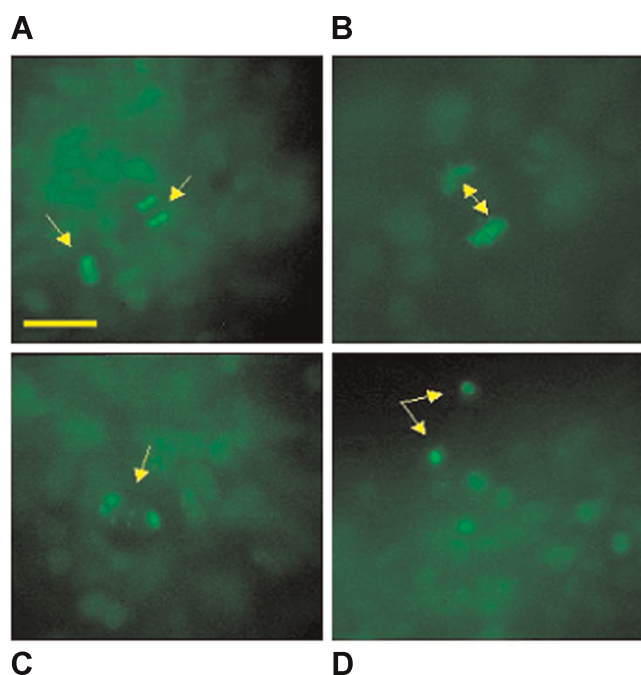


Fig. 5. Intravital microscopy at high magnification of celecoxib-treated TRAMP-C2-GFP tumors. Tumors from celecoxib-treated mice (shown in Fig. 2) were imaged by intravital microscopy at high magnification. **Panels A and B:** H2B-GFP fluorescence of TRAMP-C2-GFP tumors showing the onset of mitosis at day 3. Bar $\sim 25 \mu\text{m}$ (A); $\sim 10 \mu\text{m}$ (B). **Panels C and D:** Failed mitosis (C) with the nuclei becoming pycnotic at day 5 (D). Bar $\sim 25 \mu\text{m}$ (C,D).

mice, suggesting that celecoxib did not possess angiostatic activity in this mouse model (Fig. 6). The combination of celecoxib and castration decreased both the mean vascular area and the density of the vasculature.

In prostate cancer patients, androgen withdrawal is achieved chemically. To mimic the clinical setting, chemical castration was combined with COX-2 inhib-

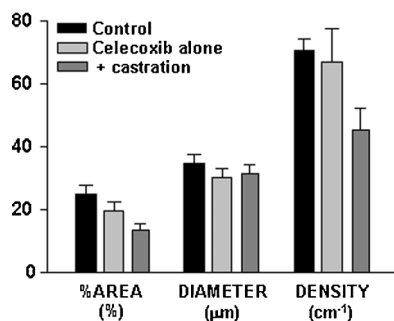


Fig. 6. Effect of celecoxib treatment on intra-tumoral angiogenesis. Tumors were imaged by intravital microscopy and vascular parameters were calculated. Graphic representation of vascular parameters (area, diameter, and density) for control, celecoxib-treated and celecoxib + castrated animals.

ition. TRAMP-C2-GFP cell spheroids were implanted with orthotropic prostate stroma in the dorsal chambers of mice. All the mice were treated with cyproterone acetate and leuprolide to induce androgen deprivation. One group of chemically castrated mice was treated with celecoxib 15 mg/kg (twice daily) whereas the other group received sham treatment (Fig. 7). As can be seen from comparing Figures 3 and 7, chemical castration and surgical castration had very similar effects on tumor growth. Combining celecoxib treatment with chemical castration caused tumor regression, similarly to the combination of celecoxib and surgical castration. The rate of mitosis increased significantly in tumors of mice treated with combination therapy compared to androgen deprivation alone (Fig. 7E). Our experiments demonstrate that surgical and chemical castration have similar effect on tumor regression when combined with celecoxib treatment.

In this model of the clinical condition, we observed a deep regression of angiogenesis within only 2 days, as shown in Figure 8. Androgen deprivation combined with celecoxib caused the vasculature to shrink, as measured by the vascular area and the vascular diameter (Panel B).

In conclusion, celecoxib alone decreased tumor growth by causing cell cycle arrest and mitotic failure. It had no measurable effect on vascular parameters in our model. Castration, which directly inhibited the proliferation of prostate cancer cells *in vitro* (Suppl. Fig. 1), blocked tumor growth *in vivo* but did not result in regression. The combination of celecoxib and androgen withdrawal, however, resulted in tumor regression and was associated with rapid shrinkage of the vasculature.

DISCUSSION

Animal models are crucial to our understanding of the mechanisms underlying tumor progression and growth. Current rodent models such as xenograft human tumors in immunodeficient mice do not sufficiently represent relevant clinical cancer models, especially with regard to angiogenesis and drug sensitivity. Transgenic animals, on the other hand, do not permit the direct measurement of tumor growth, and time-dependent observations can be made only by inference after killing mice at various time points. The dorsal skinfold chamber allows repeated observations in the same animal over extended time periods. Thus, evaluation of vascular responses to treatment can be done in real-time. The use of TRAMP-C2 cells transfected with H2B-GFP also allows us to measure increases or decreases in tumor growth and to assess other underlying mechanisms (mitosis or apoptosis) that influence tumor progression.

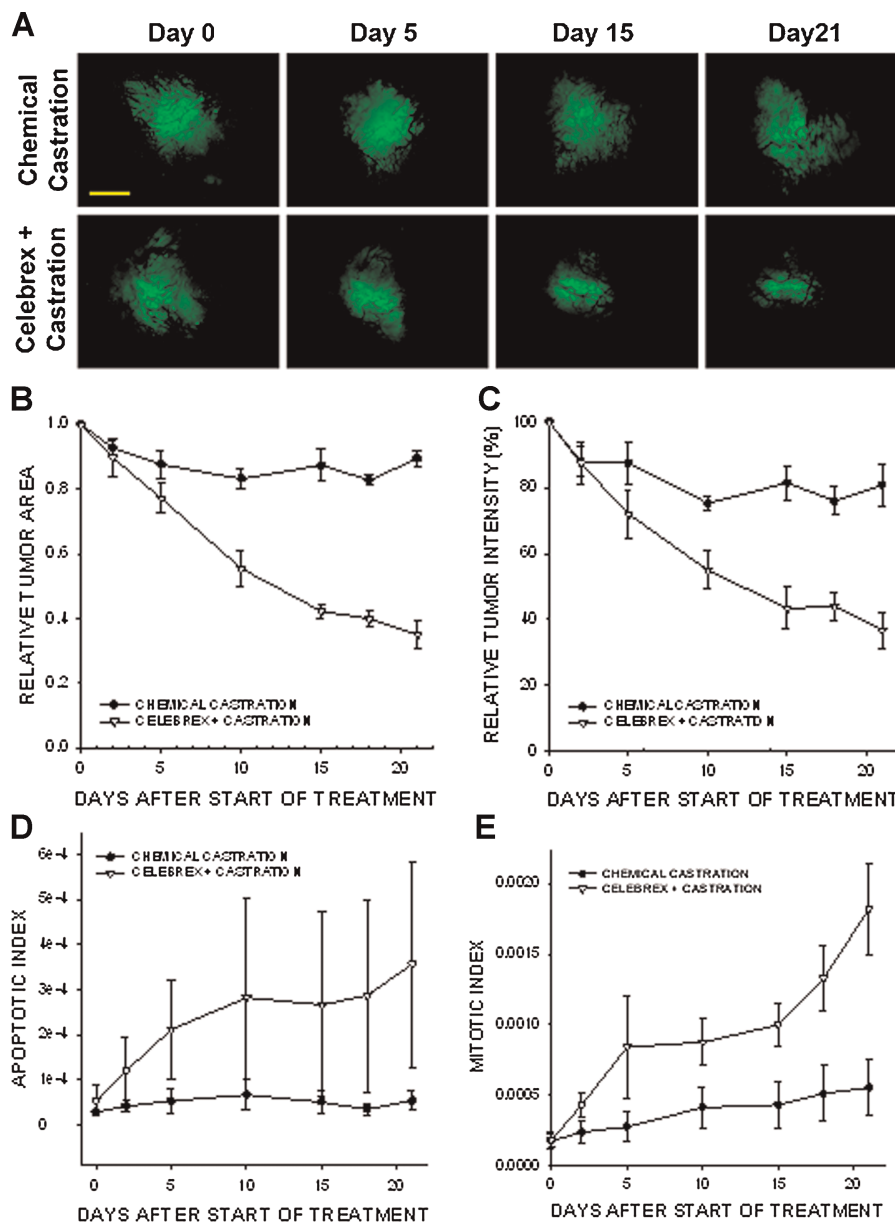


Fig. 7. Effect of combining celecoxib and hormonal ablation by chemical castration on the growth of tumors. TRAMP-C2-GFP spheroids were co-implanted with prostatic tissue and allowed to vascularize. When there was proper flow within the tumors, mice were chemically castrated by oral administration of cyproterone acetate twice daily and injection of leuprolide acetate daily, starting at Day 0. Celecoxib was administered orally twice daily, also starting at Day 0. **Panel A:** Representative collage of tumor growth. Bar $\sim 500 \mu\text{m}$. **Panels B and C:** Graphic representation of relative tumor area and intensity calculated from intravital microscopy data. **Panels D and E:** Apoptotic and mitotic index.

We have used this model to examine the effect of COX-2 inhibitor celecoxib in combination with androgen withdrawal for the treatment of prostate cancer. Surgical castration combined with celecoxib caused tumor regression, which was not observed with castration or celecoxib alone.

These results are in line with the recent finding that a combination of celecoxib and androgen withdrawal delayed the acquisition of androgen-independence in a

xenograft model using human LNCaP cells [8], which suggests that these observations may be relevant to human disease.

Observation of various tumor parameters indicated that regression was caused by a combination of decreased vascularization due to androgen withdrawal, together with tumor cells growth arrest due mostly to celecoxib treatment. Thus, the efficacy of the combination was much better in vivo than in vitro,

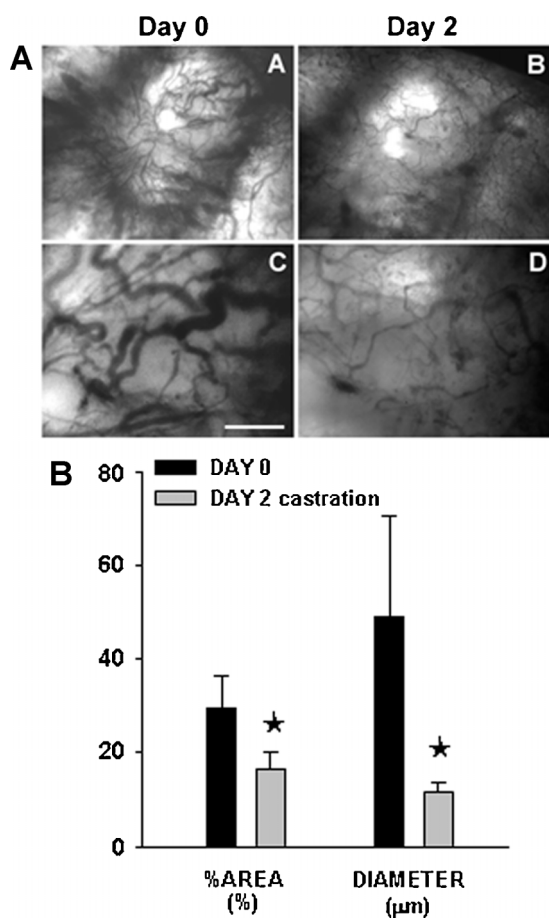


Fig. 8. Effect of hormonal ablation by chemical castration on intra-tumoral angiogenesis. Tumors from the mice treated with the combination therapy as described in Figure 6, were imaged by intravital microscopy and vascular parameters were calculated. **Panel A:** Phase contrast representative images of tumor vasculature at days 0 and 2 post-castration. Bar ~500 μm (A,B), 50 μm (C,D). **Panel B:** Graphic representation of the vascular area and the mean diameter of tumor vasculature calculated from intravital microscopy data.

because of the separate effects of each treatment on distinct biological compartments (vasculature, stroma, possibly inflammatory cells) that are not represented in the culture of cell lines.

A critical aspect in understanding and treating cancer progression is the relationship between the tumor and the “soil” that supports its growth and progression. It is well known that stromal–epithelial interactions are very important for androgen dependent prostate cancer [27]. Thus, co-implanting TRAMP-C2 cells with prostate stroma obtained from a donor mouse provides the tumor cells with an environment which closely resembles orthotopic implantation. When cancer cells were implanted in the chambers in the absence of prostate tissue, they did not grow into tumors, and treatment with celecoxib did not alter

tumor parameters (supplemental Fig. 3), exemplifying the importance of the orthotopic milieu in assessing treatment parameters.

The *in vivo* mechanism by which COX-2 affects tumor growth is still not completely understood. It has been suggested that COX-2 inhibitors induce cell cycle arrest and apoptosis in cancer cells through a mechanism that is fundamentally different from the apoptosis caused by cancer chemotherapeutic agents. Our results showing that celecoxib caused growth arrest and mitotic failure, characterized by deep alterations of nuclei morphology, and followed by mitotic catastrophe and cell death, are in agreement with this hypothesis.

Celecoxib did not alter protein levels of p53 or PARP, which are involved at early stages of apoptosis. Although in some cell lines celecoxib inhibits the PI3-kinase pathway and decreases the phosphorylation of Akt [28], we did not detect changes in phospho-Akt. However, the PI3-kinase pathway is not constitutively active in the TRAMP-C2 cells, therefore levels of phospho-Akt are barely detectable and probably not amenable to celecoxib alteration. In contrast, ERK phosphorylation was constitutively high and was inhibited by celecoxib, a result consistent with previous observations (reviewed in Ref. [29]).

We conclude that COX-2 selective inhibitor celecoxib, through COX-2 dependent and independent mechanisms, significantly increases the efficacy of androgen withdrawal in a mouse model of prostate cancer. This combination warrants further investigation as a complement therapy for aggressive prostate cancer.

ACKNOWLEDGMENTS

We thank Dale Winger for his excellent assistance in the preparation of the dorsal skinfold chambers and Reeti Bandyopadhyay for technical assistance. We also thank Dr. David Chambers (Salk Institute, San Diego) for his help with Flow Cytometry. This work was supported by funding from Pfizer, contract COXAV-V0190-010 (Dr. Per Borgström); NIH/NCI grant RO1-CA102688 (Dr. Véronique Baron); NIH/NCI grant R21CA133638 (Dr. John Welsh); DOD-CDMRP grant W81XWH-09-1-0280 and UC/CBCRP 151B-0133 (Dr. Per Borgström and Dr. John Welsh); Fellowship CTS07:1 from Carl Tryggers Stiftelse for Scientific Research, Stockholm (Dr. Parisa Abedinpour).

REFERENCES

1. Stock D, Groome PA, Siemens DR. Inflammation and prostate cancer: A future target for prevention and therapy? *Urol Clin North Am* 2008;35(1):117–130, vii.

2. Furstnberger G, Krieg P, Muller-Decker K, Habenicht AJ. What are cyclooxygenases and lipoxygenases doing in the driver's seat of carcinogenesis? *Int J Cancer* 2006;119(10):2247–2254.
3. Harris RE. Cyclooxygenase-2 (cox-2) blockade in the chemoprevention of cancers of the colon, breast, prostate, and lung. *Inflammopharmacology* 2009;17(2):55–67.
4. Sahin M, Sahin E, Gumuslu S. Cyclooxygenase-2 in cancer and angiogenesis. *Angiology* 2009;60(2):242–253.
5. Pruthi RS, Wallen EM. Cyclooxygenase-2: A therapeutic target for prostate cancer. *Clin genitourin Cancer* 2005;4(3):203–211.
6. Sooriakumaran P, Langley SE, Laing RW, Coley HM. COX-2 inhibition: A possible role in the management of prostate cancer? *J Chemother (Florence, Italy)* 2007;19(1):21–32.
7. Zheng X, Cui XX, Avila GE, Huang MT, Liu Y, Patel J, Kong AN, Paulino R, Shih WJ, Lin Y, Rabson AB, Reddy BS, Conney AH. Atorvastatin and celecoxib inhibit prostate PC-3 tumors in immunodeficient mice. *Clin Cancer Res* 2007;13(18 Pt 1):5480–5487.
8. Zheng X, Cui XX, Gao Z, Zhao Y, Lin Y, Shih WJ, Huang MT, Liu Y, Rabson A, Reddy B, Yang CS, Conney AH. Atorvastatin and celecoxib in combination inhibits the progression of androgen-dependent LNCaP xenograft prostate tumors to androgen independence. *Cancer Prev Res (Phil, PA)* 2010;3(1):114–124.
9. Antonarakis ES, Heath EI, Walczak JR, Nelson WG, Fedor H, De Marzo AM, Zahurak ML, Piantadosi S, Dannenberg AJ, Gurganus RT, Baker SD, Parnes HL, DeWeese TL, Partin AW, Carducci MA. Phase II, randomized, placebo-controlled trial of neoadjuvant celecoxib in men with clinically localized prostate cancer: Evaluation of drug-specific biomarkers. *J Clin Oncol* 2009;27(30):4986–4993.
10. Sooriakumaran P, Coley HM, Fox SB, Macanas-Pirard P, Lovell DP, Henderson A, Eden CG, Miller PD, Langley SE, Laing RW. A randomized controlled trial investigating the effects of celecoxib in patients with localized prostate cancer. *Anticancer Res* 2009;29(5):1483–1488.
11. Carles J, Font A, Mellado B, Domenech M, Gallardo E, Gonzalez-Larriba JL, Catalan G, Alfaro J, Gonzalez Del Alba A, Nogue M, Lianes P, Tello JM. Weekly administration of docetaxel in combination with estramustine and celecoxib in patients with advanced hormone-refractory prostate cancer: Final results from a phase II study. *Br J Cancer* 2007;97(9):1206–1210.
12. Fontana A, Galli L, Fioravanti A, Orlandi P, Galli C, Landi L, Bursi S, Allegrini G, Fontana E, Di Marsico R, Antonuzzo A, D'Arcangelo M, Danesi R, Del Tacca M, Falcone A, Bocci G. Clinical and pharmacodynamic evaluation of metronomic cyclophosphamide, celecoxib, and dexamethasone in advanced hormone-refractory prostate cancer. *Clin Cancer Res* 2009;15(15):4954–4962.
13. James ND, Sydes MR, Clarke NW, Mason MD, Dearnaley DP, Anderson J, Popert RJ, Sanders K, Morgan RC, Stansfeld J, Dwyer J, Masters J, Parmar MK. Systemic therapy for advancing or metastatic prostate cancer (STAMPEDE): A multi-arm, multistage randomized controlled trial. *BJU Int* 2009;103(4):464–469.
14. Pruthi RS, Derksen JE, Moore D, Carson CC, Grigson G, Watkins C, Wallen E. Phase II trial of celecoxib in prostate-specific antigen recurrent prostate cancer after definitive radiation therapy or radical prostatectomy. *Clin Cancer Res* 2006;12(7 Pt 1):2172–2177.
15. Smith MR, Manola J, Kaufman DS, Oh WK, Bubley GJ, Kantoff PW. Celecoxib versus placebo for men with prostate cancer and a rising serum prostate-specific antigen after radical prostatectomy and/or radiation therapy. *J Clin Oncol* 2006;24(18):2723–2728.
16. Frost GI, Lustgarten J, Dudouet B, Nyberg L, Hartley-Asp B, Borgstrom P. Novel syngeneic pseudo-orthotopic prostate cancer model: Vascular, mitotic and apoptotic responses to castration. *Microvasc Res* 2005;69(1–2):1–9.
17. Foster BA, Gingrich JR, Kwon ED, Madias C, Greenberg NM. Characterization of prostatic epithelial cell lines derived from transgenic adenocarcinoma of the mouse prostate (TRAMP) model. *Cancer Res* 1997;57(16):3325–3330.
18. Kanda T, Sullivan KF, Wahl GM. Histone-GFP fusion protein enables sensitive analysis of chromosome dynamics in living mammalian cells. *Curr Biol* 1998;8(7):377–385.
19. Frost GI, Borgstrom P. Real time in vivo quantitation of tumor angiogenesis. *Methods Mol Med* 2003;85:65–78.
20. Brautigam L, Vetter G, Tegeder I, Heinkele G, Geisslinger G. Determination of celecoxib in human plasma and rat microdialysis samples by liquid chromatography tandem mass spectrometry. *J Chromatogr* 2001;761(2):203–212.
21. Chow HH, Anavy N, Salazar D, Frank DH, Alberts DS. Determination of celecoxib in human plasma using solid-phase extraction and high-performance liquid chromatography. *J Pharm Biomed Anal* 2004;34(1):167–174.
22. McAdam BF, Catella-Lawson F, Mardini IA, Kapoor S, Lawson JA, FitzGerald GA. Systemic biosynthesis of prostacyclin by cyclooxygenase (COX)-2: The human pharmacology of a selective inhibitor of COX-2. *Proc Natl Acad Sci USA* 1999;96(1):272–277.
23. Lu W, Tinsley HN, Keeton A, Qu Z, Piazza GA, Li Y. Suppression of Wnt/beta-catenin signaling inhibits prostate cancer cell proliferation. *Eur J Pharmacol* 2009;602(1):8–14.
24. Narayanan NK, Narayanan BA, Reddy BS. A combination of docosahexaenoic acid and celecoxib prevents prostate cancer cell growth in vitro and is associated with modulation of nuclear factor-kappaB, and steroid hormone receptors. *Int J Oncol* 2005;26(3):785–792.
25. Patel MI, Subbaramaiah K, Du B, Chang M, Yang P, Newman RA, Cordon-Cardo C, Thaler HT, Dannenberg AJ. Celecoxib inhibits prostate cancer growth: Evidence of a cyclooxygenase-2-independent mechanism. *Clin Cancer Res* 2005;11(5):1999–2007.
26. Masferrer JL, Leahy KM, Koki AT, Zweifel BS, Settle SL, Woerner BM, Edwards DA, Flickinger AG, Moore RJ, Seibert K. Antiangiogenic and antitumor activities of cyclooxygenase-2 inhibitors. *Cancer Res* 2000;60(5):1306–1311.
27. Cunha GR, Hayward SW, Wang YZ, Ricke WA. Role of the stromal microenvironment in carcinogenesis of the prostate. *Int J Cancer* 2003;107(1):1–10.
28. Kulp SK, Yang YT, Hung CC, Chen KF, Lai JP, Tseng PH, Fowble JW, Ward PJ, Chen CS. 3-Phosphoinositide-dependent protein kinase-1/Akt signaling represents a major cyclooxygenase-2-independent target for celecoxib in prostate cancer cells. *Cancer Res* 2004;64(4):1444–1451.
29. Grosch S, Maier TJ, Schiffmann S, Geisslinger G. Cyclooxygenase-2 (COX-2)-independent anticarcinogenic effects of selective COX-2 inhibitors. *J Natl Cancer Inst* 2006;98(11):736–747.

The Combination of Plumbagin With Androgen Withdrawal Causes Profound Regression of Prostate Tumors In vivo

Parisa Abedinpour,¹ Véronique T. Baron,¹ Adrian Chrastina,^{1,2} John Welsh,¹
and Per Borgström^{1*}

¹*Vaccine Research Institute of San Diego, San Diego Science Center, San Diego, California*

²*Proteogenomics Research Institute for Systems Medicine, San Diego, California*

BACKGROUND. Hormonal ablation is the standard treatment for disseminated androgen-dependent prostate cancer. Although tumor growth is controlled at first, the tumor invariably recurs in the form of castration-resistant prostate cancer. This study assessed the efficacy of a new therapeutic strategy that combines plumbagin, a naturally occurring naphthoquinone, with androgen ablation.

METHODS. Viewing microscopy chambers were placed in the dorsal skinfold of mice. Syngeneic prostate tissue was grafted within the chambers and allowed to vascularize. H2B-GFP/PTEN-P2 prostate cancer cells were co-implanted on top of the grafted prostate tissue. Androgen ablation was achieved using surgical castration. Intact and castrated mice were administered plumbagin or sham treatment. Tumor growth, mitosis and apoptosis were monitored in real-time using fluorescent Intra-Vital Microscopy. The mechanism of action of plumbagin was explored using human and mouse prostate cancer cells.

RESULTS. Whereas both plumbagin and castration alone impeded tumor growth, only the combination of plumbagin and castration caused profound tumor regression in vivo, mostly due to increased apoptosis of the tumor cells. The cytotoxicity of plumbagin was not affected by androgens in vitro, suggesting that microenvironmental factors not present in culture play a crucial role in the combination effect. Plumbagin-induced cell death was mediated, at least in part, by activation of ERK and was due to generation of reactive oxygen species, because it was abolished by the anti-oxidant N-acetyl-L-cysteine.

CONCLUSION. Androgen deprivation in combination with plumbagin may provide a significant improvement over androgen deprivation alone and deserves further evaluation.

Prostate © 2012 Wiley Periodicals, Inc.

KEY WORDS: prostate cancer; androgen therapy; plumbagin; intra vital microscopy; dorsal chamber model; combination therapy

INTRODUCTION

Prostate cancer is typically slow growing and when the tumor is contained within the gland, medical options include watchful waiting/active surveillance

or surgery with or without radiotherapy. Once it has spread outside the prostate capsule, it is treated with hormone ablation, which invariably results in the eventual emergence of castration-resistant prostate cancer

Additional Supporting Information may be found in the online version of this article.

Grant sponsor: This work was supported by DOD-OCRP; Grant number: W81XWH-09-1-0280; Grant sponsor: PellFiCure Pharmaceuticals, Inc; Grant number: PPI001.

Disclosures: Dr. Borgström is inventor on a patent in relation to this work and is also CEO of PellFiCure Pharmaceuticals, Inc. Dr. Baron is a consultant for PellFiCure Pharmaceuticals, Inc. Drs. P. Abedinpour, A. Chrastina, and J. Welsh declare no conflict of interest.

Parisa Abedinpour and Véronique T. Baron contributed equally to this work.

*Correspondence to: Per Borgström, Vaccine Research Institute of San Diego (VRISD), San Diego Science Center, 3030 Bunker Hill, San Diego, CA 92109. E-mail: pborgstrom@vrisd.org

Received 26 July 2012; Accepted 21 August 2012

DOI 10.1002/pros.22585

Published online in Wiley Online Library
(wileyonlinelibrary.com).

(CRPC) [1]. About 90% of patients with advanced disease will develop metastases to the bone, although metastases may also develop in the liver, the lungs, and the brain [2]. While the 5-year survival rate is close to 100% for local disease, it drops to 30% for advanced cancer [3]. Conventional chemotherapeutic drugs and immunotherapy can prolong life in patients with CRPC, but the survival benefit is limited [4]. Thus, current hormonal and chemotherapy treatments for such advanced disseminated disease are palliative only and new strategies to prevent the emergence of CRPC are needed.

Plumbagin (5-hydroxy-2-methyl-1,4-naphthoquinone) is a naturally occurring naphthoquinone isolated from various plants of the Plumbaginaceae and Droseraceae families and used in traditional medicine across Asia (Fig. 1). It has anti-proliferative effects in vitro and anti-cancer effects in animal models and therefore is receiving attention as a potential therapeutic drug for the treatment of various types of cancer including prostate cancer (reviewed in [5]). Treatment with plumbagin inhibits the proliferation of prostate cancer cells in vitro [6][7]. In addition, plumbagin delays the growth of androgen-independent cancer cells in a subcutaneous xenograft mouse model [6][8]. Plumbagin-induced apoptosis was associated with the generation of reactive oxygen species (ROS) and could be prevented by treatment with the anti-oxidant N-acetyl-L-cysteine (NAC) [7].

In various types of cancer, plumbagin used in combination with radiotherapy increases apoptosis of tumor cells, demonstrating a radiosensitizing effect in cancer cells [9–12]. Plumbagin also increases the efficacy of tumor necrosis factor-related apoptosis-inducing ligand (TRAIL) in human melanoma cells [13]. These studies indicate that combination with plumbagin has the potential to improve the efficacy of several standard treatment regimens. However, the effect of plumbagin on prostate cancer when

administered at the time of androgen withdrawal has not been investigated, and this was the aim of the present study.

To assess the efficacy of plumbagin treatment in combination with castration in vivo, Intra-Vital Microscopy (IVM) was used in a mouse model of prostate cancer. IVM permits the visualization of tumors in animals and the analysis of various aspects of cancer physiology such as vascularization, tumor growth, cell migration, intra-tumoral proliferation, and apoptosis. The main advantages of IVM include the real-time analysis of dynamic processes with single-cell resolution, in a non-invasive manner. Since the application of IVM is limited to animal models that bear visually accessible tumors, we used our previously developed orthotopic dorsal skinfold chamber model (reviewed in [14]). In this model, a dorsal skinfold chamber containing a microscopy viewing window is surgically placed on a mouse. Prostate tissue is grafted within the chamber and becomes vascularized, thereby providing an orthotopic stroma on top of which the tumor cells are co-implanted. Using this model, we demonstrate that the combination of plumbagin and androgen withdrawal synergized in vivo to cause regression of prostate tumors.

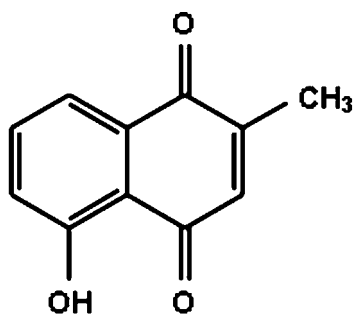
MATERIALS AND METHODS

Materials

DHT (dihydrotestosterone), Casodex[®] (bicalutamide), plumbagin from *Plumbago indica*, and NAC were purchased from Sigma-Aldrich (St. Louis, MO). Plumbagin, Figure 1, was dissolved in ethanol for in vitro experiments or in DMSO + polyethylene glycol 30% (w/v) for in vivo use.

Cell Culture

PC3 and DU145 human prostate cancer cell lines were purchased from ATCC. LNCaP cells were kindly provided by Dr. Dan Mercola (University of California, Irvine). The cell line has a characteristic morphology (described by ATCC) and its identity was verified by testing its androgen dependency and lack of the tumor suppressor gene PTEN. For each cell line, cell culture passages are limited to 20. All human cell lines were cultured according to ATCC recommendations. PTEN-P2 mouse prostate cancer cells were generously provided by the Wu laboratory and have been described in [15]. Expression of histone H2B-GFP fluorescent protein was achieved by infection with a viral vector followed by selection in geneticin as previously done in other cell lines [16]. After several weeks of selection, green-fluorescent cells were sorted by Flow Cytometry to retain cells within



5-hydroxy-2-methyl-1,4-naphthoquinone

Fig. 1. Structure of plumbagin.

a relatively homogenous range of fluorescence intensity. These cells were grown in DMEM containing 10% FBS, 2 mM L-glutamine, 100 U/ml penicillin 100 µg/ml streptomycin, insulin-selenium-transferrin (5 µg/ml insulin), and DHT 10^{-8} M final. G418 (100 µg/ml) was added to maintain stable expression of H2B-GFP.

In some experiments, androgen withdrawal was achieved by maintaining the cells in phenol red-free medium containing 10% charcoal-stripped FBS (Gibco at Life Technologies, Carlsbad, CA) and the same supplements as in the normal medium except for DHT, which was added only in the experimental conditions “+ androgen”. In other experiments, androgen withdrawal was achieved by addition of androgen antagonist Casodex to the normal growth medium.

Cell Proliferation

The effect of plumbagin on cell proliferation was measured by directly counting the cells 24 hr after treatment. Briefly, cells in 12-well plates were washed once with PBS, detached using Trypsin, and transferred to a suspension vial in a final volume of 10 ml PBS. Cells were counted using a COULTER™ Multi-sizer II instrument (Beckman Coulter Inc., Hialeah, FL) gated for the appropriate cell size and the elimination of particulate debris. Each vial was counted twice and each experiment was performed in duplicates.

Cell Cycle Analysis

Cells treated with plumbagin were suspended with trypsin and pooled with cells floating in the medium. After two washes in PBS, cells were fixed by adding ice-cold ethanol dropwise to reach a final concentration of 70% ethanol and maintained at 4°C for a minimum of 2 hr. Fixed cells were washed twice with PBS and suspended in PBS containing 0.1% Triton-X100 (v/v), 50 µg/ml PI and 50 µg/ml DNase-free RNase, for 30 min at 22°C. Fluorescence of single cells was measured by Flow Cytometry using the 488 nm laser on a Facscan instrument equipped with CellQuest (BD Pharmingen, San Jose, CA). FlowJo™ Software was used for data analysis. For quantification of the fraction of apoptotic cells, the pre-G1 fraction (containing fragmented DNA) was quantified by gating events with a cut-off at 250 on the FL2-A axis.

Western Blots

Cells were lysed on ice in the presence of phosphatase and protease inhibitors. Lysates were clarified by centrifugation, protein concentration was

determined using the BCA assay (Pierce, Rockford, IL), and lysates were resuspended in SDS-PAGE buffer. After electrophoresis, proteins were transferred to Immobilon-P® membranes (Millipore, Billerica, MA). Membranes were incubated with a 5% bovine serum albumin blocking buffer for 30 min and the first antibody was incubated overnight at 4°C. Peroxidase-conjugated antibodies (Amersham Biosciences, Piscataway, NJ) were added for 45 min at 22°C followed by a 5-min incubation in Western blot Luminata™ HRP substrate (Millipore). Analysis and quantification were performed using a FluoChem™ instrument 8900 (AlphaInnotech/Protein Simple, Santa Clara, CA). Membranes were stripped using Restore™ Stripping Buffer (Pierce/Thermo Scientific, Pittsburgh, PA) for 20–30 min at 22°C, then reprobed with the indicated antibodies. Where indicated, results were quantified using the instrument integrated quantification software (AlphaEase FC).

Animal Model and Surgical Techniques

All experiments have been approved by our IACUC and were carried out according to NIH recommended procedures and precautions. Surgeries were performed in a sterile laminar flow hood. Platinum chambers and surgical instruments were autoclaved before use. Saline used to keep tissue moist during surgical preparation was mixed with gentamicin (50 µl/ml).

Platinum chambers were fitted in the dorsal skinfold of male nude mice by surgery as described extensively in [16–18]. Two days later, a BalbC male donor mouse was euthanized and the anterior prostate tissue was excised, placed in a Petri dish with gentamicin (50 µl/ml), and minced with fine scissors into small pieces (<1 mm²) that were implanted into the dorsal chambers of host mice. The grafted tissue was allowed to vascularize for 7–10 days.

Mouse cancer cells PTEN-P2/H2B-GFP grown as pre-confluent monolayers were trypsinized and suspended in a final volume of 250,000 tumor cells/ml. Viability was determined using Trypan blue and a small number of cells (typically 50,000) was placed on top of the grafted prostate tissue.

Surgical castration was performed on mice anesthetized with 7.3 mg ketamine hydrochloride and 2.3 mg xylazine/100 g body weight, i.p. A lateral incision across the scrotum was made and the testes were individually ligated and excised. The wound was cauterized. The incision was then sutured and sealed with Nexaband® acrylic. Surgical castration induces androgen deprivation, and mimics clinical hormone therapy.

The mice were treated with plumbagin soon after castration. Plumbagin administration schedule was 1 mg/kg (DMSO/PEG30%) via i.p. injection, once a day.

Intra-Vital Microscopy

Description of microscopy instruments and objectives can be found in Supplementary Data.

Tumor area (A_T). The tumor area was calculated from the number of pixels with photo density above 40 (256 gray levels), that is, $A_T = \sum A_k$, for $40 < k < 255$.

Mitotic and apoptotic indices. At each time point, two peripheral and two central fields of the tumor were captured with an FITC filter and an integrated frame grabber. Only mitotic figures in metaphase–telophase (MI) were included. Apoptotic/Pyknotic nuclei were defined as H2B-GFP labeled nuclei with a cross-sectional area $< 30 \mu\text{m}^2$. Nuclear karyorrhexis is easily distinguishable by the vesicular nuclear condensation and brightness of H2BGFP and was included in the apoptotic index.

Statistical Analysis

To calculate the significance of differences in the in vivo data, a multivariate approach to repeated measures ANOVA was performed with a 2×6 design (two levels among groups \times six levels within subjects), using the statistics software STATISTICA (StatSoft, Inc. Tulsa, OK).

RESULTS

The Combination of Plumbagin and Androgen Ablation Causes Tumor Regression In vivo Through Increased Apoptosis

Based on earlier evidence that various syngeneic tissues grafted in rodent dorsal skinfold chambers revascularize and survive over long periods of time [17,19–22], we designed a model in which mouse prostate tissue is grafted in a microscopy viewing chamber placed in the dorsal skinfold of a male mouse, where it develops its own vasculature [17,23]. A small number of prostate cancer cells are co-implanted on top of the prostate tissue, which provides the tumor cells with orthotopic stroma.

The mouse epithelial prostate cancer cell line PTEN-P2 was chosen for this study. PTEN-P2 cells, derived from the prostate cancer tissue of a conditional prostate-specific PTEN-deficient mouse (*Pten*^{loxP/loxP}; *PB-Cre4+* mouse [24]), were generously

provided by Dr. Wu [15]. These cells are heterozygous *Pten*^{L/+} and express the protein PTEN; they are also androgen receptor (AR) positive and androgen dependent for growth [15]. PTEN-P2 cells were transfected with the histone H2B-GFP fusion protein, which is incorporated into the chromatin without affecting cell cycle progression [25]. A picture of H2B-GFP/PTEN-P2 cells in culture is shown in Supplemental Figure 1.

Although PTEN-P2 cells were initially described as non-tumorigenic in a subcutaneous graft model [15], we observed previously that they do form tumors and vascularize very well in our model, indicating that the orthotopic environment provided here supports tumor growth much better than subcutaneous models [14].

To examine the effect of combining plumbagin with androgen withdrawal in vivo, dorsal chambers were placed on male nude mice by surgery. Two days later, minced prostate tissue from BalbC mice (syngeneic) was grafted into the chambers and allowed to vascularize for 7–10 days. H2B-GFP/PTEN-P2 tumor cells were implanted onto the vascularized prostate tissue. The animals were surgically castrated when small tumors were formed (5–7 days after implantation). Surgical castration is known to effectively mimic clinical hormone deprivation. The mice were treated with plumbagin 2 days later at a dose of 1 mg/kg via intraperitoneal injection, once daily. There were four treatment groups: control (intact mice treated with carrier alone); castration (androgen deprivation and carrier); plumbagin (intact mice treated with plumbagin); combination (androgen deprivation through castration and plumbagin). Figure 2 shows IVM pictures of tumor growth in a representative mouse for each group, as a function of time. Tumor growth is reflected by an increase in fluorescence integrated over the area of the tumor and was quantified in each group as described in Methods Section (Fig. 3A). Tumors grew steadily in control mice, whereas castration caused tumor growth to stall, similarly to what is observed in patients undergoing hormone therapy. Plumbagin decreased tumor growth compared to the control but was not as efficient as castration. Tumor regression was observed following combined castration and plumbagin treatment, with a decrease in average tumor size to less than half of the original size after 26 days. The effect of the combination treatment was highly significant statistically: tumors grew 408.4% after 26 days in the control group, but shrank down to 33.9% of initial size in the combination group, $P = 0.0002$. The combination was better than either treatment alone: 33.9% versus 102.8% of initial size, combination versus castration, $P = 0.004$; 33.9%

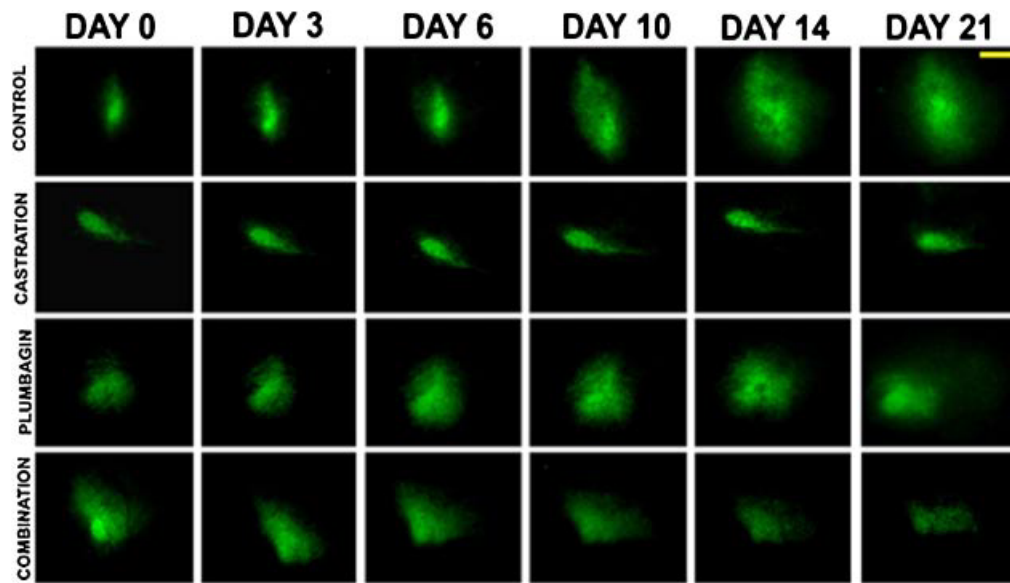


Fig. 2. H2B-GFP/PTEN-P2 cells were co-implanted with prostate tissue into mouse dorsal chambers. Half the mice were castrated once the tumors and tissue were vascularized. Soon after castration, control and castrated mice were treated with vehicle alone or plumbagin (1 mg/kg). Day 0 defines the start of plumbagin (or sham) treatment for the four treatment groups: control, castration only, plumbagin only, and castration + plumbagin. Tumors from the same mouse in each group were imaged at the indicated times using IVM. Bar $\sim 500 \mu\text{m}$.

versus 182.7% of initial size, combination versus plumbagin, $P = 0.002$.

The effect of plumbagin in castrated mice was dose dependent, as shown in Figure 3B. In this experiment, all mice were castrated and treated with increasing doses of plumbagin. A small but significant tumor regression was observed at a low dose (0.1 mg/kg), whereas a decrease in tumor sizes of over 60% was observed at a dose of 1 mg/kg. No obvious toxicity was observed based on animal weights, behavior or posture.

The ratio of apoptotic to mitotic cells was calculated for each tumor as a function of time (Fig. 3C). This ratio is a good indicator of the relative rates of cell death versus proliferation. Thus, the high ratio ($\text{AP/MI} = 28.93 \pm 0.04$) measured in the tumors of the combination group, denotes a high rate of apoptosis and is consistent with tumor regression. The difference between control and combination treatment was highly significant ($P = 0.0075$ multivariate analysis). Plumbagin induced apoptosis of the tumor cells in the castrated mice, but not nearly as much in the intact mice. In contrast, castration alone did not result in significant tumor cell apoptosis, in agreement with the notion that androgen deprivation in human patients causes mostly growth arrest.

We conclude that the combination treatment of plumbagin with castration was more efficient *in vivo* than either treatment alone, since only the combination treatment caused significant tumor regression.

Plumbagin Inhibits the Growth of Prostate Cancer Cells Independently of Androgens *In vitro*

The effect of plumbagin was assessed in prostate cancer cells that are androgen-dependent (PTEN-P2 and LNCaP) or independent (PC3 and DU145). Cells growing in normal culture medium were treated with the indicated concentrations of plumbagin for 24 hr, and cell proliferation was determined by counting the cells as described in Methods Section. The morphology of PTEN-P2 cells treated with increasing concentrations of plumbagin for 24 hr is shown in Supplemental Figure S2. As shown in Figure 4, plumbagin caused a decrease in cell number by 80% in all cell lines tested, with similar EC_{50} . No significant difference was observed between cell lines, irrespective of their androgen sensitivity.

The cytotoxicity of various synthetic derivatives of 1,4-naphthoquinone (Supplemental Fig. S6) was compared in PTEN-P2 cells. Analogs with substituents that contribute to the stabilization of the semi-quinone form and that increase the one-electron reduction potential (and therefore facilitate the formation of ROS) showed higher cytotoxicity compared with the 1,4-naphthoquinone. Plumbagin exhibited one of the lowest IC_{50} (Supplemental Fig. S7). On the other hand, substituents that increase the stability of the quinoid form and/or decrease the one-electron reduction potential showed lower cytotoxicity (Supplemental Fig. S7), in agreement with [26,27].

The combined effect of plumbagin and androgen deprivation was then assessed *in vitro* using the two androgen-dependent cell lines LNCaP and PTEN-P2. In one set of experiments, androgen deprivation was achieved by growing the cells in medium containing charcoal-stripped serum. DHT (10^{-8} M) was added back to the cells (or not) to compare cell proliferation with or without androgens. Cells were treated with

increasing concentrations of plumbagin for 24 hr before counting. As shown in Figure 5A, plumbagin had the same inhibitory effect on cell growth whether or not DHT was present.

In another set of experiments, cells grown in normal medium were treated with androgen antagonist Casodex (i.e., bicalutamide). A dose-response effect of Casodex[®] in LNCaP and PTEN-P2 cells is shown in Supplemental Figure S3. In the experiments shown in Figure 5B, cells were treated with various concentrations of Casodex[®] for 24 hr before addition of increasing doses of plumbagin for another 24 hr period. Once again, the effect of plumbagin was statistically similar in all hormone conditions. The highest Casodex[®] concentration used in these experiments induced a 20% decrease in cell numbers after 24 hr. When this effect of Casodex[®] was taken into account, the dose-response effect of plumbagin was identical in the control and Casodex[®] conditions (Supplemental Fig. S4).

We conclude that the synergistic effect of plumbagin and androgen deprivation observed *in vivo* is not due to a combination effect on the tumor cells *per se*. Instead, plumbagin and castration appear to affect distinct biological compartments *in vivo*, so that the physiological effect of the combination treatment reflects the complexity of the interactions that take place between the tumor cells, the stroma (prostate tissue) and the vasculature.

Plumbagin Increases ROS, Activates the ERK Pathway, and Induces G2/M Arrest and Tumor Cell Death

A cell cycle analysis of plumbagin-treated cells indicated that the drug induces cell cycle arrest in G2/M, as shown Figure 6A. Quantification of the pre-G0 PI-positive fraction, as shown in Figure 6B, indicated that arrest is followed by cell death. Cleavage of PARP, revealed by western blot analysis (Fig. 6C), suggested that plumbagin treatment leads mostly to apoptosis.

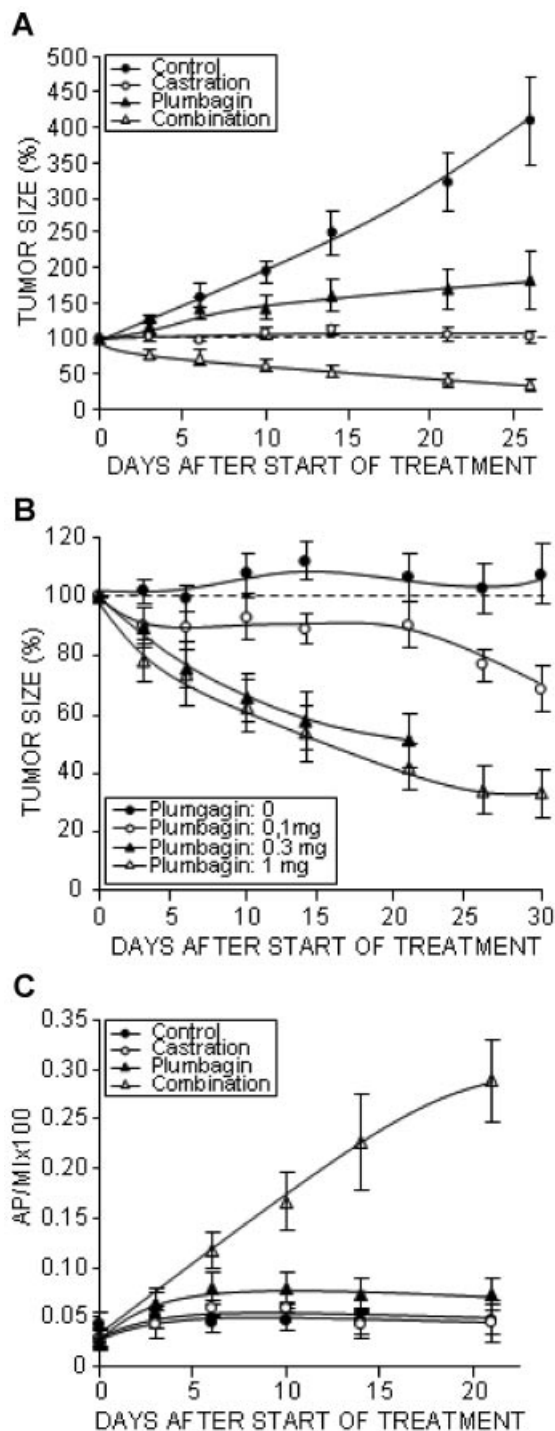


Fig. 3. **A:** Graphic representation of tumor sizes calculated from IVM data in the four treatment groups and as a function of time. Results are expressed as percent of initial (tumor size at day 0 in each group) and represent means \pm SE ($n = 6$). **B:** Tumor sizes in castrated mice treated with plumbagin at 0, 0.1, 0.3, and 1 mg/kg once daily. Sizes were calculated from IVM data as a function of time. Results are expressed as percent of initial (tumor size at day 0 for each group) and represent means \pm SE ($n = 6$, except for the 0.3 mg/kg treatment group for which $n = 5$). **C:** Representation of the ratio apoptotic index/mitotic index (AP/MI) within the tumors, calculated from IVM data obtained at high microscopy resolution. Results are expressed as absolute ratios and represent means \pm SE.

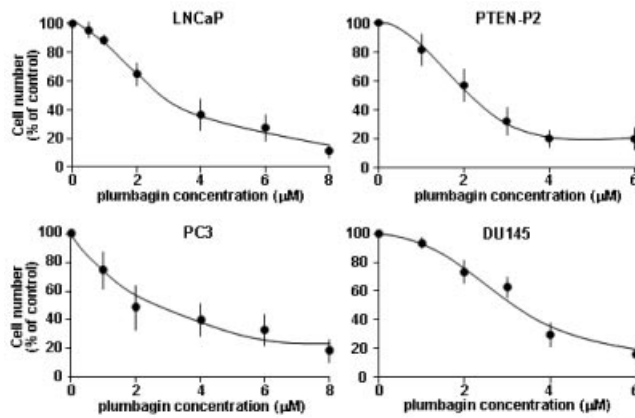


Fig. 4. Effect of plumbagin on the growth of LNCaP, PTEN-P2, PC3, and DU145 prostate cancer cell lines, in vitro. Cells grown in normal media were incubated with increasing doses of plumbagin for 24 hr, and counted using a Cell Coulter as described in Methods Section. Results are expressed as percent of control (sham-treated cells) and represent means \pm SE of at least four experiments, each performed in duplicates.

It has been shown previously that plumbagin activates various stress signaling pathways in cancer cells. Therefore, the phosphorylation of stress kinases ERK, p38 and JNK was assessed using western

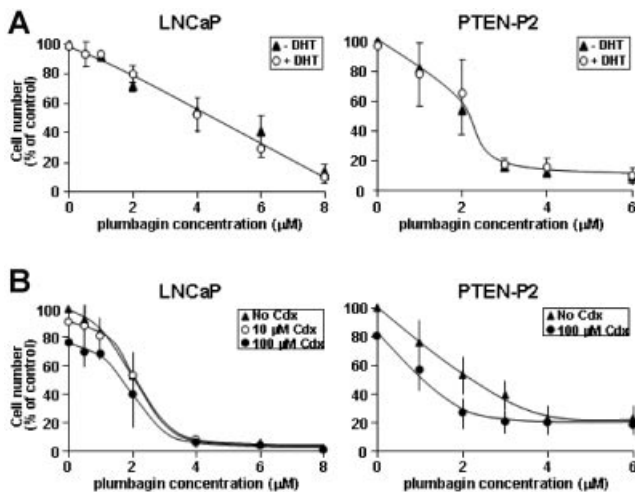


Fig. 5. Effect of plumbagin in vitro with or without hormone. **A:** Hormone-dependent prostate cancer cells LNCaP and PTEN-P2 were grown in phenol red-free medium supplemented with stripped serum, or in phenol red-free medium supplemented with stripped serum and DHT (10^{-8} M), and incubated with increasing concentrations of plumbagin for 24 hr before counting the cells. **B:** Cells were grown in regular growth medium and incubated with the indicated concentration of Casodex[®] for 24 hr. Plumbagin was added at increasing concentrations for 24 hr and cells were counted. In all graphs, results are expressed as percent of control (no treatment) and are means \pm SE of at least three experiments, each performed in duplicates.

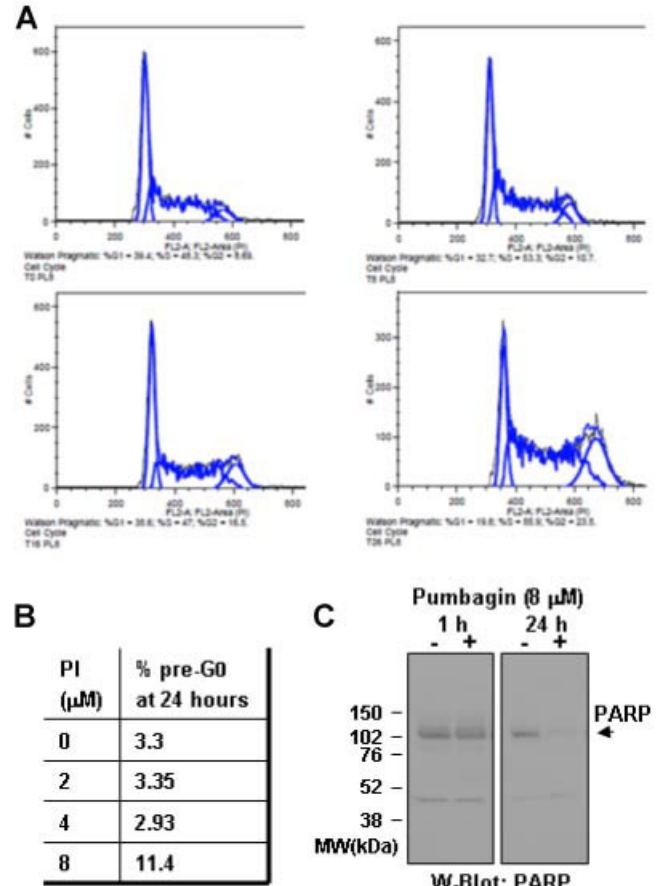


Fig. 6. **A:** Cell cycle analysis of plumbagin-treated cells. LNCaP cells were treated with plumbagin (8 μ M) for 0, 8, 16, and 26 hr. Cells were fixed and stained with propidium iodide for flow cytometry. Data were analyzed using FlowJo. **B:** The proportion of events in the PI-positive pre-G1 fraction (cut-off at 250 FL2-A) was used as an indicator of cell death. **C:** LNCaP cells treated with plumbagin (8 μ M) for 1 or 24 hr were lysed and PARP cleavage was analyzed by western blot using anti-PARP antibodies.

blotting in LNCaP cells treated with plumbagin for the indicated times. Figure 7A shows a slow increase in the phosphorylation of ERK1/2 following plumbagin treatment, with a maximum reached within 60 min. Activation of JNK and p38 was not observed.

The slow activation of ERK1/2 indicates that it is a secondary effect rather than a direct effect of plumbagin on the ERK pathway. Plumbagin causes severe oxidative stress on tumor cells and increases levels of ROS [5], which are known to activate stress signal pathways. To determine if the cytotoxic effect of plumbagin in prostate cancer cells is due to oxidative stress, cells were treated with the anti-oxidant agent NAC for 2 hr, then incubated with plumbagin for 24 hr before counting. As shown in Figure 7B, plumbagin reduced cell numbers by at least 60% depending on the concentration, whereas

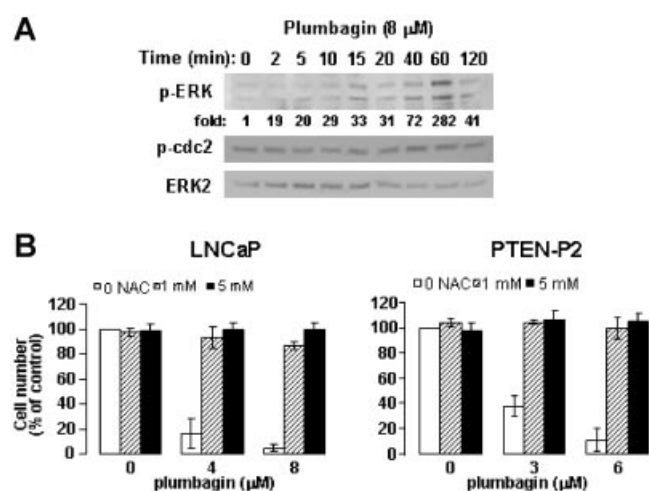


Fig. 7. A: Protein phosphorylation and expression following plumbagin treatment. LNCaP cells were treated with 8 μ M plumbagin for the indicated periods. Cells were lysed and relative protein expression or phosphorylation was analyzed by western blot using the indicated phospho-specific (p-protein) or pan (protein) antibodies. **B:** Effect of anti-oxidant NAC. LNCaP and PTEN-P2 cells were treated with the indicated concentrations of NAC for 2 hr before the addition of plumbagin at 0, 4, and 8 μ M; 24 hr later cells were counted. Results are expressed as percent of control (untreated cells) and are means \pm SE of three experiments, each performed in duplicates.

cells treated with NAC before the addition of plumbagin were entirely protected from its toxic effect. This was also observed in PC3 and DU145 cells (Supplemental Fig. S5).

Thus, plumbagin-induced toxicity is indeed due to ROS generation in the cells and subsequent activation of stress signals.

DISCUSSION

Androgen deprivation therapy remains the standard treatment for disseminated androgen-dependent prostate cancer, however, it is not curative and most patients eventually progress to androgen independence and die of the disease. Recurrence has been attributed to (i) tumor cell resistance caused by genetic amplification or mutation of the AR, activation of AR in low androgen conditions, or activation of pathways that bypass AR completely; (ii) incomplete androgen deprivation at tissue levels; and (iii) compensation mechanisms in the production of androgens by the environment [28]. Recent clinical efforts have focused on achieving more complete androgen deprivation or improving AR targeting, with some therapeutic improvements [29]. Another approach would be to delay or prevent the onset of CRPC through the combination of chemotherapy with androgen ablation.

This study examined the effect of combining androgen ablation with plumbagin, a naturally occurring quinone-type compound with demonstrated cytotoxicity toward cancer cells. Plumbagin does not necessarily target proliferating cells, as many chemotherapeutic drugs do, a potential advantage for the treatment of slow-growing tumors. Results presented here demonstrate that the combination treatment with plumbagin and castration was more efficient *in vivo* than either treatment alone. Furthermore, treatment with castration or with plumbagin only did not lead to a marked decrease in tumor size, whereas the combination of both resulted in significant decreases in tumor size, a clear improvement over castration alone.

The primary mechanism for the cytotoxic action of plumbagin and other quinone-based drugs is based on redox cycling. The quinone form of the drug is reduced to a semiquinone radical by NADPH oxidase in a process that involves the mobilization of endogenous copper [30]. This results in NADPH oxidation and oxygen reduction into superoxide [31–33]. The resulting superoxide is converted into hydrogen peroxide, hydroxyl radicals, and/or peroxynitrite, all of which are highly reactive [7,33–36]. In addition to redox cycling, plumbagin produces ROS via leakage of the mitochondrial respiratory chain [37] and by direct arylation of intracellular thiols, leading to the depletion of intracellular glutathione levels [7,36,38].

ROS are normally produced by the cell metabolism and eliminated by the glutathione/glutathione peroxidase system. Highly reactive, ROS induce damage to DNA and macromolecules such as proteins and lipids. Higher than normal levels of ROS are detected in cancer cells due in part to their higher metabolic rate and increased levels of stress, and in part to the deregulation of the detoxification system [39]. Because ROS cause cell death upon reaching a certain threshold, high constitutive levels of ROS in tumor cells often render them more sensitive to oxidative stress than normal cells, thus providing a therapeutic window for ROS-inducing drugs (reviewed in [40]). Consistent with this hypothesis, plumbagin lacks toxicity in normal cells at concentrations that kill tumor cells. For example, plumbagin effectively induced apoptosis in MDAMB-231 and MCF-7 BRCA cells whereas breast epithelial MCF-10A cells were not affected [41]. Similarly, and more relevant to the present study, non-transformed prostate epithelial cells RWPE-1 were not affected at concentrations that killed prostate cancer cells [6].

The bioavailability and pharmacokinetics of plumbagin have been reviewed [5]. Its side effects are proportional to dosage and include diarrhea, skin rash, hepatic toxicity, reproductive toxicity, and abortive

effects [42]. Early reports found that the LD50 in mouse was 16–40 mg/kg oral administration over 72 hr [43][44]. Whereas the LD50 in mice is 8 mg/kg for oral administration for 14 days, plumbagin is better tolerated when given i.p., with an LD50 at 16 mg/kg [42][43]. Most cancer therapy studies commonly use a dose of 2 mg/kg i.p., without obvious side effects. In our experiments, plumbagin was effective at doses of 1 and 0.3 mg/kg (Fig. 3B).

ROS directly (through redox-mediated structural changes in target proteins) or indirectly (through the up-regulation of stress activated pathways) alter the activity of transcription factors (review [45]). Thus, inhibition of constitutively active or cytokine-induced NF κ B appears to be a major mechanism underlying the cytotoxic effect of plumbagin in several cell types [41][46][47]. As a consequence, plumbagin also alters the expression of NF κ B target genes, blocking cell proliferation, and facilitating apoptosis [47]. It is also well established that ROS can activate stress kinases such as ERK, p38, and JNK. Although we did not observe it, we cannot rule out that plumbagin activates stress kinases p38 and JNK, which has been observed by others [37][46][48]. In contrast to other observations that plumbagin inhibits ERK activation induced by mitogens or TPA [49][50], and in accordance with [36][51], we observed slow activation of ERK, consistent with the notion that cells accumulate ROS before ERK phosphorylation takes place.

Evidence that the cellular effects of plumbagin are mediated by ROS generation is that anti-oxidants such as NAC prevent the cytotoxic effect of plumbagin as well as plumbagin-induced regulation of signaling pathways. Indeed, plumbagin-induced apoptosis was abrogated by NAC in various types of human cancer cells [30][35][36][52][53]. In addition, anti-oxidants prevent plumbagin-induced action of JNK [36] and ERK [36][51].

It is intriguing that in vitro, the effect of plumbagin was entirely independent from androgens, whereas in vivo there was synergy between plumbagin and castration. This suggests that plumbagin and castration differently affect biological compartments that are not present in culture. For example, castration has anti-vascular effects in the prostate, because the vasculature in the prostate is sensitive to androgens (reviewed in [54][55]). In the chamber model, the prostate tissue that is grafted develops a healthy vasculature that originates from the grafted tissue itself rather than from the host blood vessels, and remains androgen sensitive. Thus, castration leads to drastic vascular constriction and decreased blood flow, a shrinkage of the tumor vasculature that precedes its effects on the tumor [17]. Lai et al. have also shown that plumbagin decreases the proliferation and

migration of endothelial cells in vitro as well as in vivo and has anti-angiogenic effects [8]. Although the dose used in their study was 10 times higher than in ours, and we did not observe anti-angiogenic effects other than those due to castration (not shown), it is possible that plumbagin did have some anti-vascular effect in our in vivo model. In any case, the combined anti-angiogenic effect of castration, and tumor-directed cytotoxicity of plumbagin were only observed in vivo.

CONCLUSION

In mice bearing prostate tumors co-implanted with prostate tissue, treatment with plumbagin at the time of androgen deprivation causes tumor regression. The combination of plumbagin with castration was substantially better than either treatment alone. It remains to be seen if plumbagin, administered at the time of androgen deprivation therapy, can delay progression toward CRPC. The proposed combination warrants further investigation as an alternative therapy for high risk or aggressive prostate cancer.

ACKNOWLEDGMENTS

We are very grateful to Dr. Hong Wu (University of California, Los Angeles) for the generous gift of PTEN-P2 mouse prostate cancer cells, and to Prof. Dan Mercola (University of California, Irvine) for providing the LNCaP human cancer cells. We also thank Dr. David Chambers (Salk Institute, San Diego) for his help with Flow Cytometry, and Dr. Beryl Hartley-Asp for suggestions and critical review of the manuscript.

This study was supported by a grant from DOD-OCRP (Grant W81XWH-09-1-0280; P. Borgström and J. Welsh) and by funds from PellFiCure Pharmaceuticals, Inc. (Grant PPI001).

REFERENCES

1. Lee DJ, Cha EK, Dubin JM, Beltran H, Chromecki TF, Fajkovic H, Scherr DS, Tagawa ST, Shariat SF. Novel therapeutics for the management of castration-resistant prostate cancer (CRPC). *BJU Int*; 2012;109(7):968–985.
2. Bubendorf L, Schopfer A, Wagner U, Sauter G, Moch H, Willi N, Gasser TC, Mihatsch MJ. Metastatic patterns of prostate cancer: an autopsy study of 1,589 patients. *Hum Pathol* 2000;31(5):578–583.
3. Miller DC, Sanda MG, Dunn RL, Montie JE, Pimentel H, Sandler HM, McLaughlin WP, Wei JT. Long-term outcomes among localized prostate cancer survivors: health-related quality-of-life changes after radical prostatectomy, external radiation, and brachytherapy. *J Clin Oncol* 2005;23(12):2772–2780.
4. Higano CS, Crawford ED. New and emerging agents for the treatment of castration-resistant prostate cancer. *Urol Oncol* 2011;29(6 Suppl):S1–S8.

5. Padhye S, Dandawate P, Yusufi M, Ahmad A, Sarkar FH. Perspectives on medicinal properties of plumbagin and its analogs. *Med Res Rev* 2010; PMID: 21064184.
6. Aziz MH, Dreckschmidt NE, Verma AK. Plumbagin, a medicinal plant-derived naphthoquinone, is a novel inhibitor of the growth and invasion of hormone-refractory prostate cancer. *Cancer Res* 2008;68(21):9024–9032.
7. Powolny AA, Singh SV. Plumbagin-induced apoptosis in human prostate cancer cells is associated with modulation of cellular redox status and generation of reactive oxygen species. *Pharm Res* 2008;25(9):2171–2180.
8. Lai L, Liu J, Zhai D, Lin Q, He L, Dong Y, Zhang J, Lu B, Chen Y, Yi Z, Liu M. Plumbagin inhibits tumour angiogenesis and tumour growth through the Ras signalling pathway following activation of the VEGF receptor-2. *Br J Pharmacol* 2012;165(4b):1084–1096.
9. Devi PU, Rao BS, Solomon FE. Effect of plumbagin on the radiation induced cytogenetic and cell cycle changes in mouse Ehrlich as cites carcinoma in vivo. *Indian J Exp Biol* 1998;36(9):891–895.
10. Devi PU, Solomon FE, Sharada AC. In vivo tumor inhibitory and radiosensitizing effects of an Indian medicinal plant, *Plumbago rosea* on experimental mouse tumors. *Indian J Exp Biol* 1994;32(8):523–528.
11. Nair S, Nair RR, Srinivas P, Srinivas G, Pillai MR. Radiosensitizing effects of plumbagin in cervical cancer cells is through modulation of apoptotic pathway. *Mol Carcinog* 2008;47(1):22–33.
12. Prasad VS, Devi PU, Rao BS, Kamath R. Radiosensitizing effect of plumbagin on mouse melanoma cells grown in vitro. *Indian J Exp Biol* 1996;34(9):857–858.
13. Li J, Shen Q, Peng R, Chen R, Jiang P, Li Y, Zhang L, Lu J. Plumbagin enhances TRAIL-mediated apoptosis through up-regulation of death receptor in human melanoma A375 cells. *J Huazhong Univ Sci Technol Med Sci* 2010;30(4):458–463.
14. Baron VT, Welsh J, Abedinpour P, Borgstrom P. Intravital microscopy in the mouse dorsal chamber model for the study of solid tumors. *Am J Cancer Res* 2011;1(5):674–686.
15. Jiao J, Wang S, Qiao R, Vivanco I, Watson PA, Sawyers CL, Wu H. Murine cell lines derived from Pten null prostate cancer show the critical role of PTEN in hormone refractory prostate cancer development. *Cancer Res* 2007;67(13):6083–6091.
16. Frost GI, Dudouet B, Lustgarten J, Borgstrom P. The roles of epithelial-mesenchymal interactions and the innate immune response on the tumorigenicity of human prostate carcinoma cell lines grown in immuno-compromised mice. In vivo (Athens, Greece) 2003;17(5):377–388.
17. Frost GI, Lustgarten J, Dudouet B, Nyberg L, Hartley-Asp B, Borgstrom P. Novel syngeneic pseudo-orthotopic prostate cancer model: vascular, mitotic and apoptotic responses to castration. *Microvasc Res* 2005;69(1/2):1–9.
18. Oh P, Borgstrom P, Witkiewicz H, Li Y, Borgstrom BJ, Chrastina A, Iwata K, Zinn KR, Baldwin R, Testa JE, Schnitzer JE. Live dynamic imaging of caveolae pumping targeted antibody rapidly and specifically across endothelium in the lung. *Nat Biotechnol* 2007;25(3):327–337.
19. Funk W, Endrich B, Messmer K. A novel method for follow-up studies of the microcirculation in non-malignant tissue implants. *Res Exp Med* 1986;186(4):259–270.
20. Langer S, Sinitsina I, Biberthaler P, Krombach F, Messmer K. Revascularization of transplanted adipose tissue: a study in the dorsal skinfold chamber of hamsters. *Ann Plast Surg* 2002;48(1):53–59.
21. Laschke MW, Elitzsch A, Scheuer C, Holstein JH, Vollmar B, Menger MD. Rapamycin induces regression of endometriotic lesions by inhibiting neovascularization and cell proliferation. *Br J Pharmacol* 2006;149(2):137–144.
22. Laschke MW, Elitzsch A, Vollmar B, Vajkoczy P, Menger MD. Combined inhibition of vascular endothelial growth factor (VEGF), fibroblast growth factor and platelet-derived growth factor, but not inhibition of VEGF alone, effectively suppresses angiogenesis and vessel maturation in endometriotic lesions. *Hum Reprod (Oxford, England)* 2006;21(1):262–268.
23. Abedinpour P, Baron VT, Welsh J, Borgstrom P. Regression of prostate tumors upon combination of hormone ablation therapy and celecoxib in vivo. *Prostate* 2011;71(8):813–823.
24. Wang S, Gao J, Lei Q, Rozengurt N, Pritchard C, Jiao J, Thomas GV, Li G, Roy-Burman P, Nelson PS, Liu X, Wu H. Prostate-specific deletion of the murine Pten tumor suppressor gene leads to metastatic prostate cancer. *Cancer Cell* 2003;4(3):209–221.
25. Kanda T, Sullivan KF, Wahl GM. Histone-GFP fusion protein enables sensitive analysis of chromosome dynamics in living mammalian cells. *Curr Biol* 1998;8(7):377–385.
26. Klaus V, Hartmann T, Gambini J, Graf P, Stahl W, Hartwig A, Klotz LO. 1,4-Naphthoquinones as inducers of oxidative damage and stress signaling in HaCaT human keratinocytes. *Arch Biochem Biophys* 2010;496(2):93–100.
27. Ollinger K, Brunmark A. Effect of hydroxy substituent position on 1,4-naphthoquinone toxicity to rat hepatocytes. *J Biol Chem* 1991;266(32):21496–21503.
28. Mohler JL. Castration-recurrent prostate cancer is not androgen-independent. *Adv Exp Med Biol* 2008;617:223–234.
29. Danila DC, Morris MJ, de Bono JS, Ryan CJ, Denmeade SR, Smith MR, Taplin ME, Bubley GJ, Kheoh T, Haqq C, Molina A, Anand A, Kosciuszka M, Larson SM, Schwartz LH, Fleisher M, Scher HI. Phase II multicenter study of abiraterone acetate plus prednisone therapy in patients with docetaxel-treated castration-resistant prostate cancer. *J Clin Oncol* 2010;28(9):1496–1501.
30. Nazeem S, Azmi AS, Hanif S, Ahmad A, Mohammad RM, Hadi SM, Kumar KS. Plumbagin induces cell death through a copper-redox cycle mechanism in human cancer cells. *Mutagenesis* 2009;24(5):413–418.
31. Bachur NR, Gordon SL, Gee MV. A general mechanism for microsomal activation of quinone anticancer agents to free radicals. *Cancer Res* 1978;38(6):1745–1750.
32. Imlay J, Fridovich I. Exogenous quinones directly inhibit the respiratory NADH dehydrogenase in *Escherichia coli*. *Arch Biochem Biophys* 1992;296(1):337–346.
33. Inbaraj JJ, Chignell CF. Cytotoxic action of juglone and plumbagin: a mechanistic study using HaCaT keratinocytes. *Chem Res Toxicol* 2004;17(1):55–62.
34. Kawiak A, Piosik J, Stasiłojc G, Gwizdek-Wisniewska A, Marczak L, Stobiecki M, Bigda J, Lojkowska E. Induction of apoptosis by plumbagin through reactive oxygen species-mediated inhibition of topoisomerase II. *Toxicol Appl Pharmacol* 2007;223(3):267–276.
35. Srinivas P, Gopinath G, Banerji A, Dinakar A, Srinivas G. Plumbagin induces reactive oxygen species, which mediate apoptosis in human cervical cancer cells. *Mol Carcinog* 2004;40(4):201–211.
36. Wang CC, Chiang YM, Sung SC, Hsu YL, Chang JK, Kuo PL. Plumbagin induces cell cycle arrest and apoptosis through

- reactive oxygen species/c-Jun N-terminal kinase pathways in human melanoma A375.S2 cells. *Cancer Lett* 2008;259(1): 82–98.
37. Kuo PL, Hsu YL, Cho CY. Plumbagin induces G2-M arrest and autophagy by inhibiting the AKT/mammalian target of rapamycin pathway in breast cancer cells. *Mol Cancer Ther* 2006;5(12):3209–3221.
 38. O'Brien PJ. Molecular mechanisms of quinone cytotoxicity. *Chem Biol Interact* 1991;80(1):1–41.
 39. Brigelius-Flohe R, Kipp A. Glutathione peroxidases in different stages of carcinogenesis. *Biochim Biophys Acta* 2009;1790(11): 1555–1568.
 40. Lau AT, Wang Y, Chiu JF. Reactive oxygen species: current knowledge and applications in cancer research and therapeutic. *J Cell Biochem* 2008;104(2):657–667.
 41. Ahmad A, Banerjee S, Wang Z, Kong D, Sarkar FH. Plumbagin-induced apoptosis of human breast cancer cells is mediated by inactivation of NF-kappaB and Bcl-2. *J Cell Biochem* 2008; 105(6):1461–1471.
 42. Singh UV, Udupa N. Reduced toxicity and enhanced antitumor efficacy of betacyclodextrin plumbagin inclusion complex in mice bearing Ehrlich as cites carcinoma. *Indian J Physiol Pharmacol* 1997;41(2):171–175.
 43. Krishnaswamy M, Purushothaman KK. Plumbagin: a study of its anticancer, antibacterial & antifungal properties. *Indian J Exp Biol* 1980;18(8):876–877.
 44. Premakumari P, Rathinam K, Santhakumari G. Antifertility activity of plumbagin. *Indian J Med Res* 1977;65(6):829–838.
 45. Liu H, Colavitti R, Rovira II, Finkel T. Redox-dependent transcriptional regulation. *Circ Res* 2005;97(10):967–974.
 46. Gomathinayagam R, Sowmyalakshmi S, Mardhatillah F, Kumar R, Akbarsha MA, Damodaran C. Anticancer mechanism of plumbagin, a natural compound, on non-small cell lung cancer cells. *Anticancer Res* 2008;28(2A):785–792.
 47. Sandur SK, Ichikawa H, Sethi G, Ahn KS, Aggarwal BB. Plumbagin (5-hydroxy-2-methyl-1,4-naphthoquinone) suppresses NF-kappaB activation and NF-kappaB-regulated gene products through modulation of p65 and IkappaBalpha kinase activation, leading to potentiation of apoptosis induced by cytokine and chemotherapeutic agents. *J Biol Chem* 2006;281(25): 17023–17033.
 48. Hsu YL, Cho CY, Kuo PL, Huang YT, Lin CC. Plumbagin (5-hydroxy-2-methyl-1,4-naphthoquinone) induces apoptosis and cell cycle arrest in A549 cells through p53 accumulation via c-Jun NH2-terminal kinase-mediated phosphorylation at serine 15 in vitro and in vivo. *J Pharmacol Exp Ther* 2006; 318(2):484–494.
 49. Checker R, Sharma D, Sandur SK, Subrahmanyam G, Krishnan S, Poduval TB, Sainis KB. Plumbagin inhibits proliferative and inflammatory responses of T cells independent of ROS generation but by modulating intracellular thiols. *J Cell Biochem* 2010;110(5):1082–1093.
 50. Shieh JM, Chiang TA, Chang WT, Chao CH, Lee YC, Huang GY, Shih YX, Shih YW. Plumbagin inhibits TPA-induced MMP-2 and u-PA expressions by reducing binding activities of NF-kappaB and AP-1 via ERK signaling pathway in A549 human lung cancer cells. *Mol Cell Biochem* 2010;335(1/2):181–193.
 51. Yang SJ, Chang SC, Wen HC, Chen CY, Liao JF, Chang CH. Plumbagin activates ERK1/2 and Akt via superoxide, Src and PI3-kinase in 3T3-L1 cells. *Eur J Pharmacol* 2010;638(1–3): 21–28.
 52. Sun J, McKallip RJ. Plumbagin treatment leads to apoptosis in human K562 leukemia cells through increased ROS and elevated TRAIL receptor expression. *Leukemia Res* 2011;35(10): 1402–1408.
 53. Xu KH, Lu DP. Plumbagin induces ROS-mediated apoptosis in human promyelocytic leukemia cells in vivo. *Leukemia Res* 2010;34(5):658–665.
 54. Buttyan R, Ghafar MA, Shabsigh A. The effects of androgen deprivation on the prostate gland: cell death mediated by vascular regression. *Curr Opin Urol* 2000;10(5):415–420.
 55. Woodward WA, Wachsberger P, Burd R, Dicker AP. Effects of androgen suppression and radiation on prostate cancer suggest a role for angiogenesis blockade. *Prostate Cancer Prostatic Dis* 2005;8(2):127–132.